

Dissertation

submitted to the

Combined Faculties of the Natural Sciences and Mathematics
of the Ruperto-Carola-University of Heidelberg, Germany

for the degree of

Doctor of Natural Sciences

Put forward by

Dipl.-Phys. Benedikt Rudek

born in: Rockville/MD/USA

Oral examination: 2012/05/09

Multiple Ionization of Heavy Atoms
by Intense X-Ray Free-Electron Laser Pulses

Referees:

Prof. Dr. Joachim Ullrich

Prof. Dr. Ilme Schlichting

Abstract

The photoionization of heavy atoms, krypton and xenon, by ultra-intense X-ray laser pulses was studied at the novel X-ray free-electron laser (FEL), the Linac Coherent Light Source (LCLS). Using an ion time-of-flight (TOF) spectrometer, the ion charge-state distributions were retrieved at 1.5 and 2 keV photon energies as a function of the FEL pulse energy, while large X-ray pnCCD detectors simultaneously recorded the fluorescence spectra. The experimental findings are compared to calculations by S.-K. Son and R. Santra, that are based on perturbation theory and numerically solve a large number of coupled rate equations, and to photoionization processes in light atoms observed in previous measurements at LCLS.

For xenon unprecedentedly high charge states, up to Xe^{36+} , are found at 1.5 keV photon energy, 80 fs pulse length and 2.5 mJ pulse energy, although the ground-state ionization energy exceeds the photon energy starting at Xe^{26+} already. As direct multi-photon ionization was demonstrated to play a minor role at X-ray energies, a different ionization pathway has to be considered here. Measured fluorescence spectra along with the theoretical analysis indicate that ionization beyond the Xe^{26+} threshold is enabled by densely spaced excitation resonances which can be hit within a single broadband FEL pulse for several subsequent high charge states generated during the ionization process. In contrast to the 1.5 keV case, photoionization at 2 keV photon energy only proceeds up to Xe^{32+} , because at higher photon energy accessible resonances appear at higher charge states, which are not reached within a single shot for the pulse energies used in the present experiment.

In order to demonstrate the general nature of the multiple ionization mechanism involving resonances, similar measurements were performed for krypton at 2 keV. Here, combined experimental and theoretical analysis shows that, similar to the case of xenon at 1.5 keV, the highest observed charge state, Kr^{21+} , can only be explained by the resonance-enhanced X-ray multi-ionization process.

Based on the experimental data for two exemplary elements and the general model suggested to explain the results, resonance-enhanced photoionization in intense X-ray pulses is predicted to be a general phenomenon for heavy atoms. Thus, systems containing heavy atoms with large nuclear charge Z will experience dramatically increased photoionization in certain photon energy ranges, which can either be desirable, e.g. for the efficient creation of dense plasmas of high- Z atoms, or disturbing, e.g. for coherent diffractive imaging, where local radiation damage in the vicinity of heavy atoms can be significantly enhanced.

Zusammenfassung

Die vorliegende Arbeit befasst sich mit der Photoionisation von schweren Atomen, Krypton und Xenon, durch hoch-intensive Röntgenstrahlung, wie sie erstmalig durch Freie-Elektronen-Laser (FEL) zur Verfügung steht. Die Messungen wurden am Röntgen-FEL Linac Coherent Light Source (LCLS) durchgeführt. Mit Hilfe eines Flugzeitspektrometers wurden die in der Photoionisation resultierenden Ladungszustände für Photonenenergien von 1.5 und 2 keV als Funktion der eingestrahnten Pulsenergie bestimmt. Gleichzeitig registrierten energiesensitive pnCCD Röntgen-Detektoren die Fluoreszenzstrahlung der ionisierten Atome. Die Messergebnisse werden mit theoretischen Modellen von S.-K. Son und R. Santra, basierend auf Störungsrechnung und numerisch gelösten Ratengleichungen, unterlegt und mit vorangegangenen Photoionisations-Experimenten an leichten Atomen verglichen.

Für Xenon wurde eine Ionisation bis zu Xe^{36+} beobachtet, was den bis dato höchsten nachgewiesenen Ionisationsgrad durch Photoionisation darstellt. Die dabei genutzte Strahlung hatte eine Photonenenergie von 1.5 keV, eine Pulslänge von 80 fs und eine Pulsenergie von 2.5 mJ. Da die eingestrahlte Photonenenergie von 1.5 keV jedoch lediglich ausreicht, Xenon bis zum Ladungszustand $28+$ direkt zu ionisieren und direkte Multiphotonen-Ionisation bei Röntgenenergien eine vernachlässigbare Rolle spielt, wird in dieser Arbeit ein neuer Ionisationspfad vorgeschlagen. Anhand der Fluoreszenzspektren wird gezeigt, dass nach Erreichen der Ionisationsschwelle eines Orbitals mehrere Elektronen dieses Orbitals statt ins Kontinuum resonant in gebundene Zustände angehoben werden, von wo sie auto-ionisieren können. Solche Resonanzen sind sowohl abhängig vom Ladungszustand, der die Bindungsenergie der Elektronen bestimmt, als auch von der gewählten Photonenenergie. Während bei der Photoionisation von Xenon mit 1.5 keV innerhalb eines Röntgenpulses Ladungszustände erreicht werden, die dicht-liegende Resonanzen aufweisen, treten im Falle von 2 keV Resonanzen erst bei noch höheren Ladungszuständen auf, zu hoch, als dass sie den Ionisationsgrad noch beeinflussen könnten. Für Krypton wiederum finden sich auch bei 2 keV Photonenenergie Resonanzen, um die sequentielle Multiphotonen-Ionisation effizient verstärken zu können.

Die untersuchten Resonanzmechanismen treten überwiegend bei der Wechselwirkung von hoch-intensiven Röntgenstrahlen mit schweren Elementen auf, da diese während der Ionisation dichte Resonanzen in Valenz- und Rydbergorbitale aufweisen. Somit sind die hier nachgewiesenen Prozesse für alle Experimente zu berücksichtigen, bei denen schwere Elemente intensivem Röntgen-Licht ausgesetzt werden.

Contents

1	Introduction	1
2	Interaction of Light with Matter	7
2.1	Atomic Structure	7
2.1.1	The Unperturbed One-Electron Atom	7
2.1.2	Multielectron Atoms	8
2.2	Photoabsorption and Photoionization Processes in Atoms	11
2.2.1	An Atom in an Electromagnetic Field	12
2.2.1.1	Time-Dependent Perturbation Theory	13
2.2.2	Single-Photon Processes in Weak Electromagnetic Fields	15
2.2.2.1	Fermi's Golden Rule	15
2.2.2.2	Selection Rules	15
2.2.2.3	Resonances and Ionization	16
2.2.2.4	Photoionization in the X-ray Regime	18
2.2.2.5	Decay Mechanism of Inner-Shell Holes	19
2.2.3	Multiphoton Processes in Strong Electromagnetic Fields	22
2.2.3.1	Sequential and Direct Multiphoton Ionization	22
2.2.3.2	Classification of Strong-Field Interactions	25
2.2.3.3	Strong-Field Effects in the Tunneling Regime	26
2.2.4	Photoionization by Intense X-ray Pulses	28
2.2.4.1	Multiple Ionization of Inner-Shell Electrons	28
2.2.4.2	Modeling of X-Ray Photoionization	29
3	Experimental Setup	31
3.1	The Linac Coherent Light Source	31
3.1.1	Electron Acceleration in the Linac	31

3.1.1.1	Electron Sources	32
3.1.1.2	Accelerator	32
3.1.2	Light Generation by the Undulators	33
3.1.3	Diagnostics	36
3.1.3.1	Photon Energy	36
3.1.3.2	X-Ray Pulse Length	37
3.1.3.3	Pulse Energy	38
3.1.3.4	The LCLS Gas Monitor Device	39
3.1.3.5	The ASG Intensity Monitor	41
3.1.4	Beamlines	46
3.1.4.1	Focus Size	48
3.2	The CAMP Endstation	51
3.2.1	Gas Jet	52
3.2.2	Momentum Imaging Charged-Particle Spectrometers	54
3.2.2.1	Reaction Microscope	55
3.2.2.2	Velocity Map Imaging Spectrometer	56
3.2.2.3	Time and Spatial Resolved Ion Detection	59
3.2.3	Photon Detection	61
3.3	Data Acquisition and Analysis	63
3.3.1	From Analogue Pulses to Digitized Data	63
3.3.1.1	High-Pass Filter	63
3.3.1.2	Digital Converter	63
3.3.1.3	Analysis Software	64
3.3.2	Ion Time-of-Flight Spectra	64
3.3.2.1	Constant Fraction Discriminator	65
3.3.2.2	Calibration of a Time-of-Flight Spectrum	65
3.3.2.3	Deconvolution of Merged Charge States	66
3.3.3	Analysis of the Fluorescence Spectra	68
3.3.3.1	Correction Maps created from Dark Frames	69
3.3.3.2	Clustering of Pixels and Pixel Threshold	70
3.3.4	Machine Data	70
4	Multiple Ionization of Heavy Atoms by Intense X-Ray FEL Pulses	71
4.1	Experimental Parameters	71
4.2	Ion Spectra: Charge-State Distribution after X-ray FEL Irradiation	75

4.2.1	Ion Spectra of Xenon	75
4.2.2	Discussion of the Xenon Charge-State Distribution	78
4.2.3	Ion Spectra of Krypton	83
4.2.4	Discussion of the Krypton Charge-State Distribution	84
4.3	Ion Yield vs. Fluence: How Many Photons are Involved in the Ionization?	86
4.3.1	Xenon at 80 fs Pulse Length	86
4.3.2	Discussion of the Ion Yields for Xenon	91
4.3.3	Krypton at 80 fs Pulse Length	92
4.3.4	Discussion of the Ion Yield of Krypton	92
4.3.5	Photoionization of Krypton at 3 fs Pulse Length	93
4.3.6	Discussion of the Ion Yields for Krypton (3 fs Pulse)	95
4.4	Fluorescence Spectra of Xenon: Radiative Transitions During Ionization	97
4.5	Tracing back the Xenon Ionization Pathways	100
5	Summary and Outlook	107
A	Appendix to the Experimental Setup	113
A.1	Free-Electron Laser	113
A.1.1	Microbunching and SASE	113
A.1.2	Seeding and Resonators	115
A.1.3	Determination of the X-Ray Pulse Length	116
A.2	The CAMP endstation	121
A.2.1	A Multi-Purpose Endstation	121
A.2.2	Vacuum System	122
A.2.3	Estimating the Density and Temperature of the Gas Jet	123
A.2.4	Multi Channel Plate (MCP)	124
A.2.5	pn-Junction Charge Coupled Device (pnCCD)	125
	Bibliography	128

List of Tables

2.1	Atomic quantum numbers	8
3.1	Measurements of the X-ray pulse duration	38
3.2	Beamlines and their particular purpose at LCLS	48
3.3	Isotopic composition of xenon	67
4.1	Experimental parameters during the beamtimes in 2009 and 2011	71
4.2	Photoionization cross sections for the individual orbitals in the ground-state configuration of neutral xenon at 1.5 keV photon energy	80
4.3	Exemplary Auger cascade upon 2s photoionization in krypton	85
4.4	Minimum number of absorbed photons needed to create a given xenon charge state	87
4.5	Minimum number of absorbed photons needed to create a given krypton charge state	92

List of Figures

1.1	Peak Brilliance of Synchrotrons and FELs	3
2.1	Schematic atomic absorption spectrum below and above the ionization threshold	17
2.2	Decay mechanism of an inner-shell vacancy	20
2.3	Fluorescence yields for the K and L shells	20
2.4	Direct and sequential two-photon two-electron ionization.	22
2.5	Photoionization processes in the multiphoton regime	23
2.6	Tunneling ionization and high harmonics generation	27
3.1	LCLS machine layout	33
3.2	Undulator working principle	33
3.3	LCLS gain length	35
3.4	Light generation in bending magnet, wiggler and undulator	35
3.5	Photon energy bandwidth and energy jitter	37
3.6	The LCLS attenuator system	39
3.7	The LCLS gas monitor device	40
3.8	Intensity monitor setup and position	42
3.9	Total cross sections of rare and residual gases	43
3.10	Xenon TOF spectrum vs. pulse energy in the intensity monitor	44
3.11	GMD calibration curves	45
3.12	Xenon ion yield vs. pulse energy measured by the ASG intensity monitor	46
3.13	Reflectivity of the Soft X-ray Offset Mirror System (SOMS)	47
3.14	The LCLS photon beam line layout with instrument stations	47
3.15	Imprint studies in the HFP chamber of the AMO beamline	49
3.16	Overview of the CAMP endstation	51

3.17	Setup of the supersonic gas jet	53
3.18	The jet velocity seen in detector-hit positions	54
3.19	REMI sketch	55
3.20	Sketches of ASG REMI and VMI spectrometer	57
3.21	Two modes to run a VMI spectrometer: spatial imaging and focusing	59
3.22	The working principle of the delay line anode	60
3.23	The mounting of two pnCCD-detector pairs in the CAMP endstation	61
3.24	VMI and reaction microscope mounted in CAMP	61
3.25	Circuit of high-pass MCP read-out	63
3.26	Circuit of anode read-out	63
3.27	Constant Fraction discriminator	65
3.28	Xenon time-of-flight calibration at 50 V spectrometer voltage	67
3.29	Deconvolution of merged xenon time-of-flight peaks	68
4.1	Determination of beamline transmission by the use of the neon charge- state distribution	73
4.2	Xenon ion time-of-flight spectra at 1.5 keV photon energy for three fluences	75
4.3	Xenon ion time-of-flight spectrum at 1.5 keV and 2 keV photon energy	76
4.4	Xenon charge-state distribution at 1.5 keV and 2 keV photon energy .	77
4.5	Xenon orbital binding energies as a function of the degree of ionization	80
4.6	Xenon 3d single-hole Auger life time and inverse 3d photo-absorption rate	81
4.7	Krypton ion time-of-flight spectrum at 2 keV photon energy	83
4.8	Krypton charge-state distribution at 2 keV photon energy	84
4.9	Krypton orbital binding energies as a function of the degree of ionization	86
4.10	Determination of the pulse energy dependent ion yield from ion time- of-flight and GMD data	88
4.11	Experimental and calculated xenon ion yield vs. peak fluence at 1.5 keV and 2 keV photon energy	90
4.12	Experimental and calculated krypton ion yield vs. peak fluence at 2 keV photon energy	93
4.13	Krypton ion time-of-flight spectrum at 2 keV photon energy and 3 fs pulse length	94

4.14	Experimental and calculated krypton ion yield vs. peak fluence at 2 keV photon energy and 3 fs pulse length	95
4.15	Xe fluorescence spectra at 1500 eV photon energy	98
4.16	Diagram of an exemplary pathway leading to Xe^{36+}	100
4.17	Population of xenon charge states as a function of time during a 80 fs X-ray pulse	101
4.18	Calculated photoabsorption cross sections around 1.5 keV photon en- ergy for Xe^{21+} , Xe^{26+} and Xe^{31+}	102
4.19	Calculated photoabsorption cross sections around 1.5 keV photon en- ergy for Xe^{21+} up to Xe^{35+}	104
5.1	Xenon binding energy as a function of the ionization level and pre- dicted REXMI region at 6keV photon energy	111
A.1	Energy exchange between electron and light wave	115
A.2	LCLS X-ray pulse length determination via double core hole creation	117
A.3	LCLS X-ray pulse length determination via sidebands in a two color set up	118
A.4	Pulse length determination by light field streaking	119
A.5	The working principle of the multi channel plate	124
A.6	LCLS Photon beam line layout with instrument stations.	126

Abbreviations

- AMO** Atomic, Molecular and Optical Science
ASG Max Planck Advanced Study Group at CFEL
CAMP CFEL-ASG Multi-Purpose endstation
CASS CFEL-ASG-Software-Suite
CCD Charged Coupled Device
CFEL Center of Free-Electron Laser Science at DESY
CFD Constant Fraction Discriminator
DESY Deutsches Elektronen-Synchrotron, research center in Hamburg
FEL Free Electron Laser
FLASH Freie-Elektronen-Laser in Hamburg, the XUV to soft X-ray FEL at DESY
FWHM Full width half maximum (e.g. of a Gaussian distribution)
GMD Gas Monitor Device, pulse energy monitor at LCLS
KB mirror Kilpatrick Baez mirror, X-ray grazing incidence mirror
LCLS Linac Coherent Light Source, the X-FEL facility on the SLAC campus
REMI Reaction Microscope, ion and electron spectrometer
rms root mean square, the quadratic mean
SASE Self Amplified Spontaneous Emission
SLAC Stanford Linear Accelerator Center, an US National Lab in Menlo Park, CA
UV ultraviolet, photon energies from 3.26 eV to 6.2 eV (380 nm to 200 nm)
VMI Velocity Map Imaging (-spectrometer), ion and electron spectrometer
VUV vacuum UV, photon energies from 6.2 eV to 12.4 eV (200 nm to 100 nm)
XUV extreme UV, 12.4 eV up to 124 eV (corresponding to 100 nm to 10 nm)

Constants

- ϵ_0 vacuum permittivity, $8.854 \cdot 10^{12}$ F/m
 e elementary charge, $1.602 \cdot 10^{-19}$ C
 \hbar Planck constant, $1.054 \cdot 10^{-34}$ Js
 m_e mass of the electron, $9.109 \cdot 10^{-31}$ kg
 m_p mass of the proton, $1.672 \cdot 10^{-27}$ kg

Chapter 1

Introduction

About hundred years ago, studies of the fundamental processes in light-matter interaction have set both, the foundation of modern physics and a starting point for applications indispensable in many disciplines of natural science today. In 1898, Wilhelm Conrad Röntgen discovered the X-rays [1]; in 1900, Max Planck postulated the quantization of emitted electromagnetic energy, $E = \hbar\omega$, an assumption incompatible with classical physics [2]. Albert Einstein seized Planck's idea to introduce *light quanta* - now called photons - to explain the photoelectric effect, where electrons were emitted from surfaces irradiated by light and their kinetic energy was found to be solely dependent on the frequency ω of the incident light but not on its intensity [3]. That also explained why electrons were only emitted when the photon energy exceeded the work function of the irradiated material independent of the light intensity. In an extension of this experimentally verified model, Maria Göppert-Mayer theoretically discussed the possibility that two photons could be absorbed simultaneously, adding up the single photon energies to surpass the ionization threshold [4]. Because two-photon absorption requires relatively high light intensities, an experimental demonstration of this process in the optical domain was not possible until 1965, when a new technology, the LASER, provided extremely intense radiation which could, for instance, ionize a xenon atom by combining the energy of seven 1.78 eV photons to overcome the ionization threshold of 12.13 eV [5]. Since then, multiphoton ionization has become a powerful tool to investigate the behavior of targets perturbed by the intense laser field, and still remains a hot topic in atomic, molecular and optical physics.

Until recently, the technological and scientific advances in the area of laser science

and the applications of X-rays were mostly separate fields. Röntgen's X-rays were first used to capture images of human bone structures [6], which is still the most famous application today. In 1912 Max von Laue pointed out the importance of the short wavelength and the penetration depth of X-rays for structural analysis. He predicted that X-ray diffraction in crystals would provide information about the position of the atoms and the arrangement of the chemical bonds. His theory led to the earliest X-ray diffraction experiment on a single crystal [7]. Peter Debye and Paul Scherrer extended the approach for powder diffraction [8]. Laue's model was simplified by William Henry Bragg and William Lawrence Bragg, who proposed a basic condition for coherent and incoherent scattering from a crystal lattice, now known as Bragg's law [9]. Thereupon X-ray diffraction on crystals, X-ray crystallography, became a standard tool for structural analysis in biology, chemistry and material science and resulted in more than a dozen Nobel prizes. One prominent example is the discovery of the helical structure of the DNA [10]. While first experiments were restricted to broadband X-ray tubes limited in tunability and photon intensity, X-ray crystallography heavily benefited from the development of synchrotron light sources [11]. Synchrotrons offer much higher peak brilliance (see notes in figure 1.1), which allows for better resolution, and are tunable over a wide range of wavelengths. One of the main factors currently limiting the achievable resolution in X-ray crystallography is given by the radiation dose the sample can tolerate before its structure is significantly modified due to the onset of radiation damage.

Moreover it typically requires crystallized samples, where diffraction from different periodic layers add up to the total signal. Otherwise, even synchrotrons cannot deliver enough luminosity to gain sufficient structural information. Here extreme intensities and high degree of coherence common to lasers would be needed. Most lasers, on the other hand, are restricted to the infrared, optical or ultraviolet spectral range.

With the advent of free-electron lasers (FELs) radiation with unique, laser-like properties became available in the extreme-ultraviolet (XUV) and X-ray domains, the spectral range typically covered by synchrotrons. FELs deliver peak brilliances nine orders of magnitude higher than modern synchrotrons (see figure 1.1), shorten the pulse length down to a few tens of femtoseconds and even below while providing full spatial and partial temporal coherence. Thus, the start-up of the first hard X-ray free-electron laser, the Linac Coherent Light Source (LCLS), has sparked intense

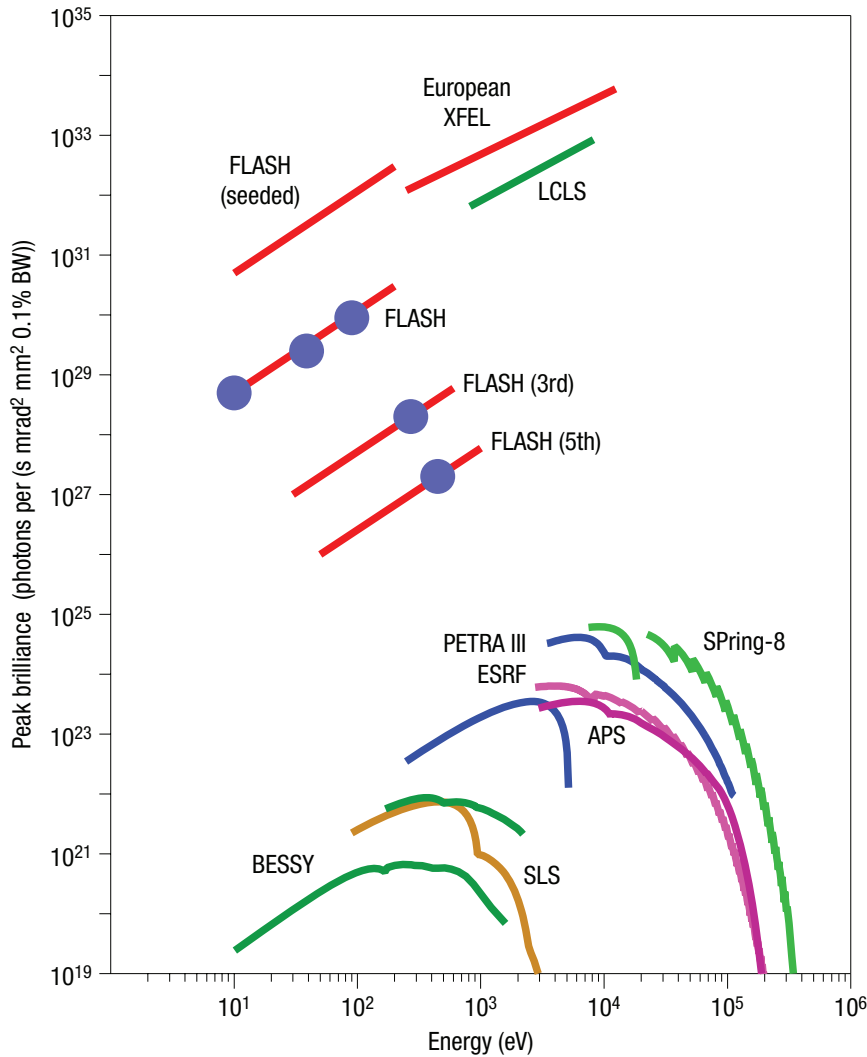


Figure 1.1 – Peak brilliance of XUV and X-ray FELs in comparison with third-generation synchrotron-radiation light sources. Blue spots show the experimental performance of the FLASH XUV FEL at DESY at the fundamental, 3rd and 5th harmonics; the LCLS X-ray FEL performance is drawn in green, the design parameters of the upcoming European XFEL in red. Lower colored lines refer to various state-of-the-art synchrotrons as indicated in the figure. For comparison: Standard X-ray tubes have a bremsstrahlung continuum of about 3 to 30 keV with up to 10^7 photons/(s $\text{mrad}^2 \text{mm}^2 0.1\%$), the copper $K\alpha$ line lies at 8050 eV with up to three orders of magnitude higher brilliance than bremsstrahlung. The peak brilliance is defined as number of photons per time [s], opening angle [millirad] squared, beam area [mm^2] and 0.1% of the bandwidth. It is proportional to the pulse intensity (number of photons times the photon energy divided by area and time). Image source: W. Ackermann et al. Nature Photonics 1, 336-342 (2007). Copyright (2007) by the Nature Publishing Group.

research activities of a broad scientific community exploiting the unique properties of FEL light.

One large portion of research activity at LCLS is related to X-ray scattering another to X-ray absorption. X-ray scattering, as described above, is used to retrieve structural information from large molecules and solid samples; X-ray absorption yields insight about the electronic response of matter to the impinging radiation.

In scattering experiments the unique combination of extreme peak intensity and short pulse length common for FELs allows one to acquire a sufficiently bright single-shot image before the disintegration of the sample blurs out the image [12]. Here, single-shot coherent diffractive imaging (CDI) of crystals as well as of non-periodic samples has been demonstrated in proof-of-principle-experiments at LCLS [13, 14]. Moreover, to provide save grounds for this new technique, sample disintegration times and impact of radiation damage on the resolution has been started to be investigated [15, 16], image classification algorithms have been improved [17] and methods have been developed to account for the finite-size effect of nano- to micrometer-sized crystals used in first experiments [18].

In first X-ray absorption experiments at LCLS the electronic response of small few-electron quantum systems, i.e. individual atoms, for example neon [19, 20], and small molecules, for example nitrogen [21–23], to X-ray pulses of unprecedentedly high intensity was investigated. Here, multiple photoionization was found to predominantly proceed via sequential single-photon single-electron interactions [19–21], in good agreement with earlier theoretical predictions [24]. Although the signatures of the direct two-photon processes, where two light-quanta add their energies to remove or excite one electron, were experimentally observed, their contribution was found to be rather small [20, 25]. In general, strong-field phenomena playing an important role in the optical domain, such as "tunneling" and "electron recollision" with the nucleus [26–28], could be neglected, owing to the high photon energy where in a simple picture the electromagnetic field oscillates too fast to allow for any significant response by the atomic potential. However, an inherent novel feature of the interaction with high-intensity pulses at short wavelength is the creation of multiple inner-shell vacancies [19, 21]. These multiple core-hole states occur when the X-ray intensity is high enough to photoionize the inner-shell of the ion a second time before the initial inner-shell vacancy is filled. Here, the energy of the electron liberated during an Auger decay into double-core holes was shown to carry information about

the chemical environment [22, 23].

While such fundamental experiments on X-ray absorption are of direct importance for the understanding of atomic structure and dynamics, the knowledge of the single-atom response to intense X-ray radiation also has considerable impact on virtually all other scientific applications of X-FELs. In a sense, atomic physics is the starting point of any approximation needed to describe larger systems. With neon and nitrogen, the first studies at LCLS focused on light atoms and molecules. Most of the samples in scattering experiments, however, contain at least a few heavy elements, for which different mechanisms of the interactions with light might be expected - given the experience from experiments with heavy atoms at high-intensity light sources of lower photon energy [29–31].

This thesis deals with the photoionization of heavy atoms, xenon and krypton, by high-intensity, femtosecond X-ray pulses provided by the LCLS. The main goal of this work was to study dominant multiple ionization pathways for systems with high atomic number Z , to search for basic differences compared to lighter elements, and to highlight potential features and mechanisms specific for the heavy atoms.

Multiple ionization was experimentally studied using the combination of a time-of-flight (TOF) spectrometer measuring ionic charge-state distributions, and energy-resolving, single-photon counting X-ray detectors simultaneously recording the fluorescence spectra during the ionization. The simultaneous measurement allows one not only to define the final charge state of the system, but also to trace signatures of the inner-shell vacancies from the radiative relaxation of the excited ions. The experimental results were compared to calculations (performed by S.-K. Son and R. Santra) based on perturbation theory and numerically solved coupled rate equations. In contrast to the earlier experiments on lighter elements, charge states with ionization potentials far exceeding the energetic limit for the sequence of single-photon single-electron ionization steps were observed. Combined experimental and theoretical analysis of the ion charge-state distributions and correlated fluorescence spectra indicate that this enhanced ionization is caused by intermediate resonances which enable photoionization beyond the direct one-photon photoionization threshold. This mechanism, denoted as "resonance-enabled X-ray multiple ionization" (REXMI), is predicted to be a general phenomenon for high- Z atoms irradiated by sufficiently intense X-ray pulses, and is expected to play an important role for many XFEL application, such as, e.g., the creation of dense plasmas of heavy elements,

or local radiation damage in coherent diffractive imaging.

The work is structured as follows: In Chapter 2, the description and nomenclature of the atomic structure and basic photoionization mechanisms at different photon energies and intensities will be introduced. Chapter 3 describes the LCLS X-ray FEL and the experimental apparatus used to simultaneously record ionic and fluorescence spectra. In Chapter 4, the obtained experimental results are presented and discussed in comparison with the outcome of the theoretical model of Son and Santra. Finally, Chapter 5 summarizes the findings of the work and gives an outlook towards future experiments.

Chapter 2

Interaction of Light with Matter

Multiphoton multiple ionization in the X-ray regime is a new phenomenon and has only become accessible at the novel ultra-intense X-ray free-electron laser LCLS at Stanford. To put this new kind of light-matter interaction into physical and historical context, atomic photoionization and decay mechanisms in different wavelength regions and the basics of the underlying theory will be discussed in this chapter.

2.1 Atomic Structure

2.1.1 The Unperturbed One-Electron Atom

In classical mechanics, the equation of motion, Newton's 2nd law $F = \dot{p}$, predicts the temporal evolution of a mechanical system. In quantum mechanics, the Schrödinger equation, analogue to Newton's law, describes how the quantum state of a physical system changes in time. In the Schrödinger equation, the wavefunction ψ replaces the local coordinate in the classical equation of motion. Wavefunctions can also form standing waves, called stationary states or orbitals. To calculate these orbitals, the time-independent Schrödinger equation is used. For the hydrogen or hydrogen-like atom, an electron of mass m_e is interacting with the nucleus, assumed to be infinitely heavy, through the Coulomb potential. Then, the time-independent Schrödinger equation (in SI units) becomes

$$H\psi(r, \theta, \phi) = \left(-\frac{\hbar^2}{2m_e} \nabla^2 - \frac{e^2}{4\pi\epsilon_0 r} \right) \psi(r, \theta, \phi) = E\psi(r, \theta, \phi) \quad (2.1)$$

Due to the spherical symmetry of the atom, the electron wavefunction ψ is chosen to be dependent on its spherical coordinates $\psi(r, \theta, \phi)$. Here, \hbar is Planck's constant, e the electron charge, and E its energy Eigenvalues. Expressing the Laplacian operator ∇^2 in spherical coordinates allows to separate ψ into a radial part, $R_{nl}(r)$, and an angular part, $Y_l^m(\theta, \phi)$:

$$\psi(r, \theta, \phi) = R_{nl}(r)Y_l^m(\theta, \phi) \tag{2.2}$$

Solving the time-independent Schrödinger equation with this Ansatz yields, that the hydrogen atom can be described by three independent quantum numbers. The spherical harmonics $Y_l^m(\theta, \phi)$ depend on the angular momentum quantum number l , and the magnetic quantum number m_l . The radial part, which basically is a polynomial multiplied by an exponential, defines the principal quantum number n . n is associated with the energy of the electron, l with the angular momentum and m_l with its z -projection. The quantum numbers can be summarized as shown in table 2.1. Here, the quantum numbers m_s , which represent the z component of the electron spin angular momentum, is introduced ad hoc, and can only consistently derived within a relativistic treatment of the problem. It will be shortly discussed for multielectron atoms below.

Quantum number	Associated physical quantity	Range
n principal	$E_n = \frac{-e^2}{8\pi\epsilon_0 a_0 n^2}$	$1, 2, 3, \dots$
l angular momentum	$ L = \hbar\sqrt{l(l+1)}$	$0 \leq l \leq n-1$
m_l magnetic	$L_z = m\hbar$	$m = 0, \pm 1, \pm 2 \dots \pm l$
m_s spin		$\pm \frac{1}{2}$

Table 2.1 – Atomic quantum numbers

Commonly n is denoted K, L, M, \dots for $n = 1, 2, 3, \dots$ and l as s, p, d, f, \dots for $l = 0, 1, 2, 3, \dots$

2.1.2 Multielectron Atoms

In multielectron atoms the electrons not only experience the attractive Coulomb potential of the nucleus, but also repulsions by the other electrons. To account for this, electron correlation terms have to be added to the Schrödinger equation; e.g. for helium, the time-independent Schrödinger equation can be written as a sum of

two hydrogen-like Hamiltonians, $H_H(1)$ and $H_H(2)$, for each individual electron, plus an interelectronic repulsion term $e^2/(4\pi\epsilon_0 r_{12})$:

$$\left(H_H(1) + H_H(2) + \frac{e^2}{4\pi\epsilon_0 r_{12}} \right) \psi(\vec{r}_1, \vec{r}_2) = E\psi(\vec{r}_1, \vec{r}_2) \quad (2.3)$$

Then an exact solution of the Schrödinger equation is not possible any more. However, approximation methods yield solutions with sufficient accuracy. Widely used techniques are perturbation theory, which will be introduced in section 2.2.1.1, and the variation method. The *variational principle* says that, if the ground-state wavefunction ψ_0 is substituted by any other function ϕ , the eigenvalue E_ϕ will always be greater than the ground-state energy E_0 :

$$E_\phi = \frac{\int \phi^* H \phi d\tau}{\int \phi^* \phi d\tau} \geq \frac{\int \psi_0^* H \psi_0 d\tau}{\int \psi_0^* \psi_0 d\tau} = E_0 \quad (2.4)$$

Thus, any trial function ϕ can be taken to calculate an upper bound of the ground-state energy. This trial function may be dependent on some arbitrary *variational parameters*, so that E_ϕ can be minimized with respect to these variational parameters to get as close as possible to the ground-state energy E_0 .

Neglecting the interelectronic repulsion term in equation 2.3 for now, the ground-state wavefunction would be a product of the hydrogen wavefunctions of the two individual electrons

$$\phi_0(\vec{r}_1, \vec{r}_2) = \psi_{1s}(\vec{r}_1)\psi_{1s}(\vec{r}_2) \quad \text{with} \quad \psi_{1s}(\vec{r}_j) = \left(\frac{Z_{eff}^3}{\pi a_0^3} \right)^{1/2} e^{-Z_{eff} r_j / a_0} \quad (2.5)$$

as calculated from equation 2.2, for the hydrogen ground-state $n = 1$, $m = l = 0$ and with $j = 1$ or $j = 2$. This wavefunction can now serve as trial function with the effective nuclear charge Z_{eff} as variational parameter. It is inserted into equation 2.4 (with normalized wavefunctions $\int \phi^* \phi d\tau = 1$), evaluated with the Hamiltonian in equation 2.3

$$E(Z_{eff}) = \int \phi(\vec{r}_1, \vec{r}_2) H \phi(\vec{r}_1, \vec{r}_2) d\vec{r}_1 d\vec{r}_2 = \frac{m_e e^4}{16\pi^2 \epsilon_0^2 \hbar} \left(Z_{eff}^2 - \frac{27}{8} Z_{eff} \right) \quad (2.6)$$

then minimized with respect to Z_{eff} and yields, now in atomic units (where $e = \hbar = m_e = 1$),

$$\frac{dE(Z_{eff})}{dZ_{eff}} = 2Z_{eff} - \frac{27}{8} \Rightarrow Z_{eff} = \frac{27}{16} \quad (2.7)$$

This result is substituted back into equation 2.6 to give $E_\phi = -2.8477$ for the ground-state energy of the helium atom (experimental result -2.9033)[32]. For more accurate calculations, a trial function with more than one variational parameter can be chosen, i.e. in a linear combination $\phi = \sum_{j=1}^N c_j f_j$ where f_j themselves may contain variational parameters; then, however, minimization of $E(c_j)$ has to be done numerically.

In the illustrative example above, the interelectronic repulsion term was completely neglected, hydrogen ground-state orbitals ψ_{1s} were used, and the Pauli exclusion principle did not restrict the electron configuration. Modifications to correct for these shortcomings are expressed in the Hartree-Fock method [33].

In the Hartree-Fock procedure, the two-electron wavefunction $\psi(\vec{r}_1, \vec{r}_2)$ can be written as product of one-electron orbitals, such as in equation 2.5, but with arbitrary orbitals $\phi(\vec{r}_1)\phi(\vec{r}_2)$ (in practice a linear combination of *Slater orbitals* is used [34], see below). The potential energy that electron 1 experiences at point r_1 due to electron 2 can be expressed as effective potential

$$V_1^{eff}(r_1) = \int \phi^*(\vec{r}_2) \frac{1}{r_{12}} \phi(\vec{r}_2) d\vec{r}_2 \quad (2.8)$$

where the probability distribution of the second electron, $\phi^*(\vec{r}_2)\phi(\vec{r}_2)d\vec{r}_2$, is interpreted as classical charge density (mean field approximation). Because the effective one-electron Hamiltonian in the *Hartree-Fock equation* with the orbital energy ϵ_1 is now dependent on $\phi(\vec{r}_2)$ via $V_1^{eff}(r_1)$,

$$H_1^{eff}(\vec{r}_1)\phi(\vec{r}_1) = \left(-\frac{\hbar^2}{2m_e} \nabla_1^2 - \frac{e^2}{4\pi\epsilon_0 r_1} + V_1^{eff}(r_1) \right) \phi(\vec{r}_1) = \epsilon_1 \phi(\vec{r}_1) \quad (2.9)$$

an iterative approach, the *self-consistent field method*, is required: first a form of $\phi(\vec{r}_2)$ is guessed to set a $V_1^{eff}(r_1)$ for the calculation of H_1^{eff} . In turn the resulting $\phi(\vec{r}_1)$ is used to get better value of $\phi(\vec{r}_2)$. These iterations are repeated until the field becomes self-consistent. The final wavefunctions ϕ are called Hartree-Fock orbitals.

In quantum mechanics, elementary particles have a characteristic property, i.e. the spin, which has no classical analogon. For electrons the spin is either $+1/2$ or $-1/2$. Then their wavefunction consists of two parts, a spatial (e.g. $1s$) and a spin (α or β) part. Under the Pauli exclusion principle, all electronic (in general: fermionic) wavefunctions must be antisymmetric under interchange of any two electrons ($\psi(2,1) = -\psi(1,2)$). Therefore, one part in the electronic wavefunction has to be symmetric, the other one antisymmetric. For the two indistinguishable

ground-state electrons of helium, the linear combination of all possible labeling of the two electrons is $\psi = 1s\alpha(1)1s\beta(2) - 1s\alpha(2)1s\beta(1)$. The Slater determinant

$$\psi(1, 2) = \frac{1}{\sqrt{2!}} \begin{vmatrix} 1s\alpha(1) & 1s\beta(1) \\ 1s\alpha(2) & 1s\beta(2) \end{vmatrix} \quad (2.10)$$

accounts for the indistinguishability of the electrons in accordance with the Pauli Principle an asymmetric wavefunction as a linear combination of single-electron orbitals. While for the two-electron-system, helium, only the spatial part was considered in H_1^{eff} , the full Slater determinant has to be used in systems with more than two electrons. Then H_1^{eff} will be substituted by the more complex Fock operator.

Up to now, several approximations have been used that can be accounted for in more sophisticated treatments. The Hartree-Fock method itself is based on the central field approximation, where the electrons are considered to move in the mean field of all other electrons, rather than including the instantaneous repulsion between electrons. If the correlation energy of electrons cannot be neglected, Hartree-Fock orbitals can be treated as zero-order wavefunctions and the correlation energy can be calculated by perturbation theory [32]. Moreover, a non-relativistic approach was used, which is not valid for heavy atoms and can be accounted for e.g. by the relativistic HF approximation. Then, the finite mass of the nucleus has to be considered, which can strictly only be done within quantum electrodynamics (QED). Finally, if it comes to precision atomic structure calculations QED effects have to be taken into account that are particularly important for the inner-shell levels of high- Z atoms due to their $\sim Z^4$ scaling

2.2 Photoabsorption and Photoionization Processes in Atoms

When an atom or molecule interacts with an electromagnetic field, it can absorb the quantized photon energy $\hbar\omega$. Consequently, electrons will either undergo a bound-bound transition between two energy levels, $E_i - E_f = \hbar \cdot \omega$, or, when the photon energy exceeds the electron binding energy, will be emitted into the continuum carrying away the excess energy, $E_{kin} = \hbar \cdot \omega - E_i$ ("bound-free" transition). To quantitatively describe the photon-atom interaction, transition probabilities upon photon impact can be derived from time-dependent perturbation theory ("Fermi's

Golden Rule") as outlined in section 2.2.1. These transition probabilities also imply certain selection rules. Photoionization involving inner-shell electrons represent an interesting case, since it results in the creation of an inner-shell vacancy, which is filled either radiatively or non-radiatively, and, thus, is discussed separately in section 2.2.2.4 and 2.2.2.5.

In intense electromagnetic fields, more than one photon can be absorbed to photoionize an atom. Here, photoionization has been distinguished [35] to proceed either via multiphoton absorption [36] or via "tunneling" [26], which are classified by photon energy and intensity dependent parameter as described in detail in section 2.2.3.2. Finally in section 2.2.4.1, photoionization at X-ray energies and high intensities will be put in context to these regimes and modeling approaches, as well as relaxation mechanisms of core-excited atoms summarized.

2.2.1 An Atom in an Electromagnetic Field

The Hamiltonian for a hydrogen-like atom with nuclear charge Z and mass m_e with the electron coordinate \vec{r} in an electromagnetic field is given by

$$H(\vec{p}, \vec{r}) = \frac{1}{2m} \left(\vec{p} - q\vec{A}(\vec{r}) \right)^2 - \frac{Ze^2}{4\pi\epsilon_0 r} \quad (2.11)$$

In addition to the electrons' kinetic energy expressed by $\vec{p}^2/2m_e$, and its potential energy in the electric field of the nucleus as described in equation 2.1, the interaction with the external electromagnetic field is considered via the vector potential $\vec{A}(t)$. It is related to the magnetic induction field \vec{B} via $\vec{B}(\vec{r}) = \nabla \times \vec{A}(\vec{r})$ and to the electric field \vec{E} via $\vec{E} = -\nabla\Phi(\vec{r}) - \frac{\partial\vec{A}}{\partial t}$, where $\Phi(\vec{r})$ is the scalar potential [37, 38].

When the *Coulomb gauge* is chosen, one has $\nabla \cdot \vec{A} = 0$. Then with $\vec{p} = -\hbar\nabla$

$$\left(\vec{p} - q\vec{A}(\vec{r}) \right)^2 = \vec{p}^2 - \vec{p}q\vec{A} - q\vec{A}\vec{p} + q^2\vec{A}^2 = \vec{p}^2 - q\vec{A}\vec{p} + q^2\vec{A}^2 \quad (2.12)$$

because $\vec{p} \cdot \vec{A} = -\hbar\nabla \cdot \vec{A} = 0$. Equation 2.11 simplifies to

$$H = \frac{\vec{p}^2}{2m_e} - \frac{Ze^2}{4\pi\epsilon_0 r} - \frac{q}{2m_e} \left(\vec{A} \cdot \vec{p} + q^2\vec{A}^2 \right) \quad (2.13)$$

The first two terms represent the field-free Hamiltonian, while the last term is dependent on the vector potential. In weak fields \vec{A}^2 is small and will, therefore, be neglected.

The vector potential of the electromagnetic field with the polarization vector $\vec{\epsilon}$ is approximated as plane wave

$$\vec{A}(\vec{r}, t) = A_0 \vec{\epsilon} e^{i(\vec{k}\vec{r} - \omega t)} \quad (2.14)$$

Then this plane wave is separated into a space- and a time-dependent part and expanded for the spatial part

$$\vec{A}(\vec{r}, t) = A_0 \vec{\epsilon} \cdot e^{i(\vec{k}\vec{r} - \omega t)} = A_0 \vec{\epsilon} \cdot e^{-i\omega t} \cdot \left(1 + i\vec{k}\vec{r} + \frac{(i\vec{k}\vec{r})^2}{2!} + \dots\right) \quad (2.15)$$

As the wavelength $\lambda = 2\pi/k$ is large as compared to the orbit of an electron of about 1 \AA for most cases where the photon energy is not too high, $\vec{k}\vec{r} \ll 1$ and higher orders can be neglected. This is called the *electric dipole approximation*; "electric" because an \vec{r} -independent vector potential discards the magnetic induction field ($\vec{B}(\vec{r}) = \nabla \times \vec{A}(t)$). The Schrödinger equation then becomes

$$i\hbar \frac{\partial}{\partial t} \psi(\vec{r}, t) = H \psi(\vec{r}, t) = \left(\frac{\vec{p}^2}{2m} - \frac{Ze^2}{4\pi\epsilon_0 r} - \frac{q^2}{m_e} A_0 \vec{\epsilon} \vec{p} e^{-i\omega t} \right) \psi(\vec{r}, t) \quad (2.16)$$

which is generalized to

$$i\hbar \frac{\partial}{\partial t} \psi(\vec{r}, t) = \left(H_0 + \vec{d} \cdot e^{-i\omega t} \right) \psi(\vec{r}, t) \quad (2.17)$$

where H_0 is the Hamiltonian of the field-free particle, and $(q/m_e)A_0\vec{\epsilon}\vec{p}$ was summarized as \vec{d} , the dipole operator. Because there is no general analytical solution to this equation, numerical approaches or approximation methods have to be applied.

2.2.1.1 Time-Dependent Perturbation Theory

If the interaction with the electromagnetic field in equation 2.16 is sufficiently weak to be regarded as small perturbation, which will leave the population of a state "almost" untouched, the exact solutions of a time-independent, unperturbed system can be found, and corrections from the time-dependent Hamiltonian $H'(t)$, describing the perturbation, can be added.

Here, the general form of perturbation theory is derived [37], and will be applied for the special case of a short perturbation by an oscillating electric field in the next section.

Equation 2.17 is generalized using the parameter ζ for the order of the perturbation as

$$i\hbar \frac{\partial}{\partial t} |\psi(t)\rangle = (H_0 + \zeta H'(t)) |\psi(t)\rangle \quad (2.18)$$

The exact solution of a time-independent unperturbed system H_0 with eigenfunctions $|n\rangle$, time-dependent phases $e^{-i\omega_n t}$ and energy eigenvalues $E_{0,n}$ is

$$i\hbar \frac{\partial}{\partial t} |n(t)\rangle = H_0 |n(t)\rangle \quad \text{with} \quad |n(t)\rangle = e^{-i\omega_n t} |n\rangle \quad \text{and} \quad \omega_n = \frac{E_{0,n}}{\hbar} \quad (2.19)$$

so that the perturbed states $|\psi(t)\rangle$ can be expanded in a linear combination of the orthonormal, unperturbed and time-independent eigenfunctions with the coefficients c_{ni}

$$|\psi(t)\rangle = \sum_n c_{ni}(t) e^{-i\omega_n t} |n\rangle \quad (2.20)$$

where the index i marks the initial unperturbed state at time zero. Without perturbation the state does not change - that is expressed by the equation $c_{ni}(0) = \delta_{ni}$. This expansion is inserted in equation 2.18 to investigate if the system changed from its initial unperturbed eigenvalue, now denoted as $|i_0\rangle$, to a final unperturbed eigenvalue $|f_0\rangle$. With the product rule, subtraction of $\omega_n = \frac{E_{0,n}}{\hbar}$ and multiplication with $\langle f_0 | e^{i\omega_f t}$ (i.e. the projection on state f_0) a system of differential equations is obtained

$$i\hbar \frac{\partial}{\partial t} c_{fi}(t) = \sum_n \langle f_0 | \zeta H | n_0 \rangle e^{i\omega_{fn} t} c_{ni}(t), \quad \text{with} \quad \omega_{fn} = \omega_f - \omega_n \quad (2.21)$$

For the zeroth order $\zeta = 0$, the system is unperturbed so that $c_{fi} = \delta_{fi}$. This coefficient is now inserted into equation 2.21 to calculate the first order. Then, zeroth and first order are used to calculate the second order and so on. Zeroth, first and second order are

$$\begin{aligned} c_{fi}(t) = & \delta_{fi} \\ & - \frac{i}{\hbar} \int_0^t dt' \langle f_0 | H'(t') | i_0 \rangle e^{i\omega_{fi} t'} \\ & + \left(\frac{i}{\hbar} \right)^2 \int_0^t dt' \int_0^{t'} dt'' \sum_n \langle f_0 | H'(t') | n_0 \rangle \times \langle n_0 | H'(t'') | i_0 \rangle e^{i\omega_{fn} t'} e^{i\omega_{ni} t''} \\ & + \dots \end{aligned} \quad (2.22)$$

Then $c_{fi}(t)$ is interpreted as probability amplitude for a transition from $|i_0\rangle$ to $|f_0\rangle$. In any of the individual matrix elements, just a single perturbation by the photon field is expressed. Thus, in second order, for example, the system is perturbed twice, which means that two photons were involved. The probability for a transition is given by the square of the modulus

$$W_{fi} = |c_{fi}(t)|^2 \quad (2.23)$$

2.2.2 Single-Photon Processes in Weak Electromagnetic Fields

2.2.2.1 Fermi's Golden Rule

The perturbation of the light field is described as $H'(t) = \vec{d} \cdot e^{-i\omega t} = H'e^{\pm i\omega t}$ (equation 2.17), where the time dependence is separated from the perturbing Hamiltonian $H'(t)$. The *first order* perturbation then becomes [37]

$$c_{fi}(t) = -\frac{i}{\hbar} \int_0^t dt' \langle f_0 | H' | i_0 \rangle e^{i(\omega_{fi} \pm \omega)t} = -\frac{i}{\hbar} \langle f_0 | H' | i_0 \rangle \frac{e^{i(\omega_{fi} \pm \omega)t} - 1}{i(\omega_{fi} \pm \omega)} \quad (2.24)$$

with the transition probability as described in equation 2.23

$$W_{fi} = |c_{fi}(t)|^2 = \frac{1}{\hbar^2} |\langle f_0 | H' | i_0 \rangle|^2 \frac{4 \sin^2[(\omega_{fi} \pm \omega) \frac{t}{2}]}{(\omega_{fi} \pm \omega)^2} \quad (2.25)$$

Because the term containing $\Delta\omega = \omega_{fi} \pm \omega$ can be approximated for long times (the system will be evaluated long time after the perturbation) with

$$\lim_{t \rightarrow \infty} \frac{4 \sin^2[(\omega_{fi} \pm \omega) \frac{t}{2}]}{(\omega_{fi} \pm \omega)^2} = 2\pi t \delta(\omega_{fi} \pm \omega) \quad (2.26)$$

the famous Fermi's Golden Rule is found defining the transition rate P_{fi}

$$\boxed{P_{fi} = \lim_{t \rightarrow \infty} \frac{W_{fi}(t)}{t} = \frac{2\pi}{\hbar} |\langle f_0 | H' | i_0 \rangle|^2 \delta(E_f - E_i \pm \hbar\omega)} \quad (2.27)$$

with $\hbar\omega_{fi} = E_f - E_i$ being the energy difference between final and initial state.

The perturbing Hamiltonian H' for photo-absorption is, in the dipole approximation, the dipole operator $\vec{d} = A_0(q/m_e)\vec{\epsilon} \cdot \vec{p}$ and, thus, $\langle f_0 | \vec{d} | i_0 \rangle$ is called *transition dipole moment*, M_{fi} . Because the dipole operator is proportional to the field amplitude A_0 , the transition rate $|M_{fi}|^2$ is proportional to the amplitude squared. Then, since $A_0^2 \propto I$, the transition rate is linearly proportional to the intensity in first-order perturbation theory:

$$\boxed{P_{fi}^{(1)} = \sigma_1 I^1} \quad (2.28)$$

2.2.2.2 Selection Rules

For a photo-absorption in the dipole approximation, the dipole operator is inserted into the transition dipole moment M_{fi} often using the *length-form* where $\vec{p} = \vec{r}$, so that with linear polarized light along the z-direction $\vec{d} = A_0(q/m_e)\vec{\epsilon} \cdot \vec{p} \hat{\times} q\vec{r} = q\vec{z}$

$$M_{fi} \propto q \int \langle \psi_f | z | \psi_i \rangle \quad (2.29)$$

In the above section about the atomic structure, ψ was expressed in a radial part and an angular part (equation 2.2). Here, the spherical harmonics are rewritten as $Y_l^m(\theta, \phi) = 1/\sqrt{2\pi}\Theta_m^l \cdot e^{im\phi}$ with the associated Legendre functions Θ_m^l so that

$$\psi_{n,l,m_l} = \frac{1}{\sqrt{2\pi}} R_{n,l}(r) \Theta_m^l(\theta) e^{im\phi} \quad (2.30)$$

Then the matrix element becomes with $z = r \cdot \cos \theta$

$$(M_{fi})_z = \frac{1}{2\pi} \int_{r=0}^{\infty} R_i R_f r^3 dr \cdot \int_{\theta=0}^{\pi} \Theta_{m_f}^{l_f} \Theta_{m_i}^{l_i} \sin \theta \cos \theta d\theta \cdot \int_{\phi=0}^{2\pi} e^{i(m_f - m_i)\phi} d\phi \quad (2.31)$$

From the last factor concerning the the magnetic quantum number following condition has to be fulfilled so that $(M_{fi})_z$ is non-zero: $\Delta m_{if} = (m_f - m_i) = 0$, i.e. the z-component of the angular momentum, remains unchanged. An illustrative explanation is that the angular momentum of linear polarized light can be expressed as a sum of Eigenstates with $\pm\hbar$ circular polarization and, thus, its z-component is zero in average.

The second factor is only non-zero for $\Delta l = l_i - l_f = \pm 1$, a change by one in the angular momentum quantum number. Since the photon angular momentum is $\pm\hbar$, the quantum number l of the atom has to change by $\pm\hbar$ to conserve the total angular momentum.

Other selection rules, such as for the total angular momentum in many-electron systems and the spin quantum number, will not be discussed in the context of this work. Also note that these selection rules are only valid for electric dipole transitions, and must be modified for multipole or magnetic transitions. Magnetic dipole transitions are typically 10^5 times less likely than dipole transitions. The next multipole transition, the electric quadrupole, is typically 10^8 times less likely than dipole transitions [39], such that both classes of transitions will be neglected here. There is no selection rule for the principal quantum number n , and all transitions are allowed, as long as they are energetically possible and in accordance with the selection rules for the other quantum numbers.

2.2.2.3 Resonances and Ionization

Fermi's Golden Rule describes (electric dipole) transition rates in general, regardless whether a photon is absorbed or emitted, or whether the final state is bound or lies in the continuum. Here, the photoabsorption rate in the vicinity of the photoionization

threshold, that means the border from bound to continuum states, is discussed since it relates directly to the experimental situation of this work.

Bound-bound transitions require a discrete photon energy within a small interval ΔE around $\hbar \cdot \omega = E_i - E_f$. The energy interval where absorption occurs is called linewidth, named after the sharp lines in a continuous absorption energy spectrum. According to the Heisenberg uncertainty principle $\Delta E \Delta t \geq \hbar/2$, the linewidth is connected to the lifetime Δt of the bound state where the electron is excited to. Because of the limited linewidth, bound-bound transitions are called resonances.

Close to the ionization threshold, the spacing of excited states becomes very dense. These highly excited states, named after Johannes Rydberg, have macroscopic radii making them suitable to be described by the Bohr model: Rydberg states can be considered as hydrogenic systems, i.e. as nuclei with a single electron in a Coulomb potential. Then, the binding energy is calculated with the Rydberg formula as

$$E_n = -Ry \cdot \frac{Z_{eff}^2}{n^2} = -13.6eV \cdot \frac{(q+1)^2}{n^2} \quad (2.32)$$

where the Rydberg constant Ry equals the ground-state binding energy of an electron in hydrogen, and the effective charge of the nucleus Z_{eff} is the total charge of the nucleus minus the number of shielding electrons. So for neutral atoms $Z_{eff} = 1$, for ions of charge state q it follows $Z_{eff} = q + 1$. The linewidth of transitions into Rydberg states is very small due to their long lifetime.

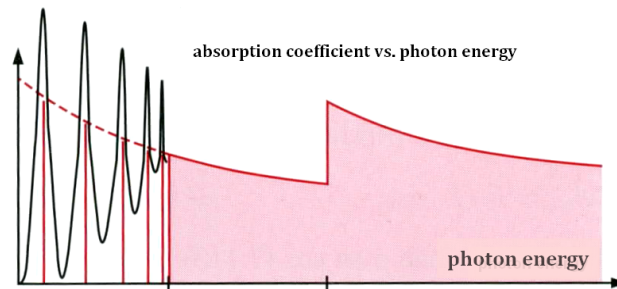


Figure 2.1 – Schematic atomic absorption spectrum below and above the ionization threshold. Below the threshold photons are absorbed at sharp photon energies to excite electrons into Rydberg states (sharp red lines with a black envelope illustrating an actual detector resolution). Above threshold the atom is ionized and electrons are emitted into the continuum (red area). The two steps in the absorption spectrum illustrate photoionization of different shells¹.

¹Source: Demtröder Experimentalphysik 3: Atome, Moleküle und Festkörper [40]

For $n \rightarrow \infty$ the transition rate for resonant excitation into densely-spaced Rydberg states, expressed by the dipole moment M_{fi} , smoothly converges towards the transition rate into unbound continuous states, as illustrated in figure 2.1.

2.2.2.4 Photoionization in the X-ray Regime

The X-ray regime is classified by a wavelength range between ten nanometer down to about one picometer [41], corresponding to 124 eV to 124 keV. This range is commonly divide into soft X-rays, with the photon energies up to the argon (2958 eV) K-edge [42], and hard X-rays for higher photon energies, where the wavelength of few Ångström and below becomes comparable to the length of a chemical bond (and hence enabling structure determination with atomic-scale resolution).

Photoionization at X-ray energies proceeds predominantly through single-photon ionization of the deepest energetically accessible inner-shell electron. For one-electron atoms and ions the photo-electric cross section σ can be derived (see [43]) as

$$\sigma = \frac{16\sqrt{2}\pi}{3}\alpha^8 Z^5 \left(\frac{m_e c^2}{\hbar\omega}\right)^{7/2} a_0^2 \quad (2.33)$$

where $\alpha \approx 1/137$ is the fine structure constant and $a_0 \approx 0.5 \text{ \AA}$ the first Bohr radius of hydrogen. This formula can also (approximately) be applied to inner-shell photoionization in the X-ray regime, far-off from any absorption edges. The energy dependency shows, that photoabsorption rapidly decreases with higher photon energy for a given electronic state. The Z^5 term implies, that heavier elements have a higher X-ray absorption than lighter elements. In addition, since heavier elements have lower lying shells, i.e. a series of edges (see figure 2.1), absorption is dramatically enhanced. So in experiments with molecules consisting of different elements the X-ray photon is preferably absorbed by inner-shell electrons of the high- Z -elements. That means X-ray photon absorption is *element-specific* which is a crucial feature for chemical analysis. A review on spectroscopic applications of monochromatic soft X-rays can be found in reference [44].

While X-ray photoionization is predominantly a one-photon one-electron process, nevertheless through electron correlation one X-ray photon can ionize two electrons simultaneously with rather low probability (typically less than 1%) [45], e.g. via the so-called shake-off process. Here, in sudden approximation the electronic wavefunction has to adjust after photoionization. Then, the wavefunction of the neutral

initial state is projected onto the ionic final state exhibiting overlap with continuum states, offering the possibility that the electron is "shaken-off" [46–48].

2.2.2.5 Decay Mechanism of Inner-Shell Holes

Inner-shell photoionization leaves the ion in a highly excited state.



For relaxation, the inner-shell vacancy ("core-hole") is filled with an electron of an outer shell. The binding energy difference of these shells is dissipated via two competing mechanisms:

Fluorescence In a radiative decay, an X-ray photon is emitted. Its energy equals the binding energy difference of the inner and outer shell, $\hbar\omega = E_o - E_i$:



The atom relaxes but the charge state remains. For fluorescent decay, selection rules apply, see section 2.2.2.2 above.

Auger Decay By Coulomb interaction, the liberated transition energy can be transferred to a second outer-shell electron, which then is emitted carrying the excess energy. The excess energy is the binding energy difference of the inner and outer shell (transition energy) minus the ionization potential of the ejected electron, $E_{kin} = E_{excess} = |E_i| - |E_o| - |I_P|$. When the excess energy is not fully transformed into kinetic energy of the electron, but also into an additional excitation of an outer-shell electron, the Auger decay is called satellite Auger transition. In a double Auger decay, the excess energy is sufficient to emit even two electrons at the same time.

Auger decay mediated by intra-shell transitions is called Coster-Kronig-decay. If energetically allowed Coster-Kronig decay is the dominating Auger channel.

The single Auger decay is described by



Auger decay increases the ion charge state by one or, with low probability, by two (double Auger). The Auger decay mechanism is non-radiative, so it is not limited by selection rules.

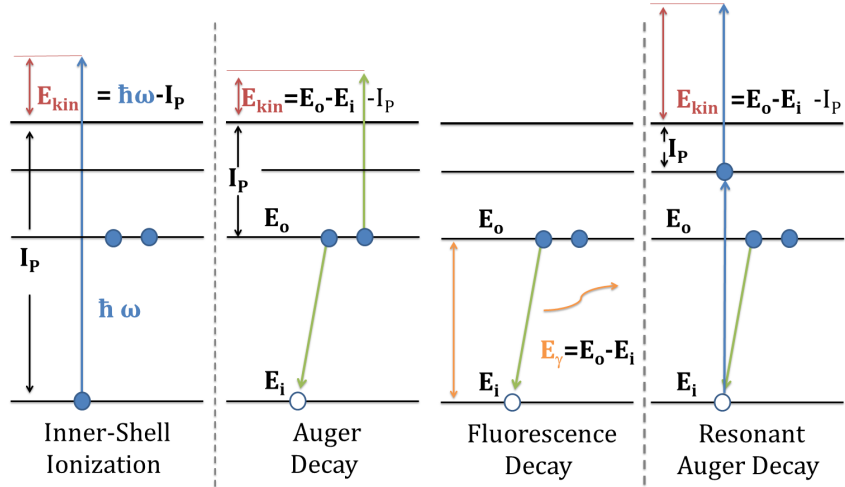


Figure 2.2 – Decay mechanism of an inner-shell vacancy.

Auger decay and fluorescence decay are illustrated in figure 2.2. In cases where the shells above E_o are filled as well, electrons of these shells will fill the E_o vacancy, so that the vacancy successively moves to higher shells until full relaxation. This is called decay cascade. If the inner-shell vacancy is created by a resonant excitation instead of a photoionization, the subsequent Auger decay is called resonant Auger decay [49], see on the very right in figure 2.2. It will become important when the photon energy is not sufficient for direct single ionization of a core electron, and when resonant bound-bound transitions are energetically possible instead.

Both decay mechanisms show a Z dependence: for a K-shell vacancy, the X-ray fluorescence rate strongly increases for heavier atoms, $\propto Z^4$, while the Auger rate rises slower than linear [38, 50].

In figure 2.3 the fluorescence yield for the K-shell and the average yield for the three L-shells are plotted as a function of the atomic number. Accordingly, core-hole relaxation in heavy elements proceeds primarily through radiative decay, but becomes less likely for relaxation of vacancies in outer shells.

The strong Z dependence of the fluorescence

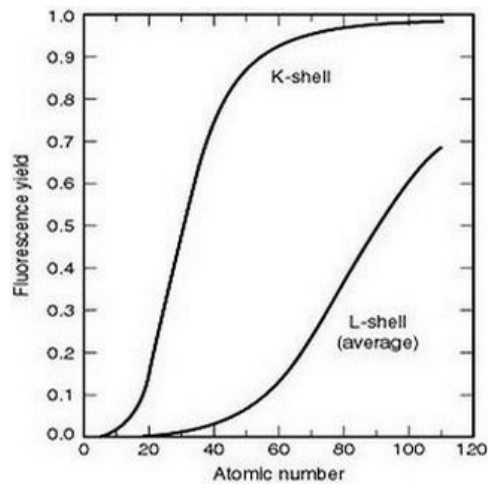


Figure 2.3 – Fluorescence yields¹

¹Source: X-ray data booklet http://xdb.lbl.gov/Section1/Sec_1-3.html

rate is based on a cubic dependence as a function of the emitted photon energy [46]. Thus, in a decay cascade, started by a K-shell vacancy, the first decays are predominantly radiative but non-radiative Auger transitions are dominating for outer-shells [38]. When the transition energy during a decay cascade is not sufficient anymore to liberate an electron, Auger decay is energetically not possible, and the excited state relaxes radiatively instead.

2.2.3 Multiphoton Processes in Strong Electromagnetic Fields

2.2.3.1 Sequential and Direct Multiphoton Ionization

Here, different pathways of photoionization will be discussed proceeding from single to multiple photoabsorption. They are illustrated in figure 2.4 for the ejection of two electrons and in figure 2.5 for one electron ejection.

For a quantitative treatment of processes in the multiphoton regime perturbative theory can be employed. The first-order perturbation theory describes the interaction with a single photon, whereas in the n-th order n photons contribute to excitation or ionization. Because of the iterative approach in the calculation of the expansion coefficients $c_{fi}^{(n)}(t)$ (equation 2.22) the transition dipole moment appears n-times in the calculation of the n-th order coefficient. That means the transition probability for an n-th order transition rises with the power of n. As $|M_{fi}|^2 \propto P \propto I$ for single-photon absorption, $|M_{fi}|^{2n} \propto P^n \propto I^n$ is valid for multiphoton absorption. With the generalized cross sections σ_n the multiphoton transition probability is derived as

$$P_{fi}^{(n)} = \sigma_n I^n \quad (2.37)$$

In the following this result will be discussed for the different pathways of photoionization.

When the photon energy exceeds the ionization potential of the atom, $\hbar\omega > I_p$, single photon ionization is possible and the most likely ionization process (panel a) in figure 2.5). Upon ionization the Coulomb force of the nucleus is shielded by less electrons and, thus, the remaining electrons are stronger bound.

If the photon energy still exceeds the ionization potential of the created ionic state, a second photon can be absorbed resulting in *sequential ionization*, depicted on the right in figure 2.4. In figure 2.4 the direct two photon double ionization (TPDI) is illustrated. It has become observable at high photon intensities in

Two Electron Photoionization Processes

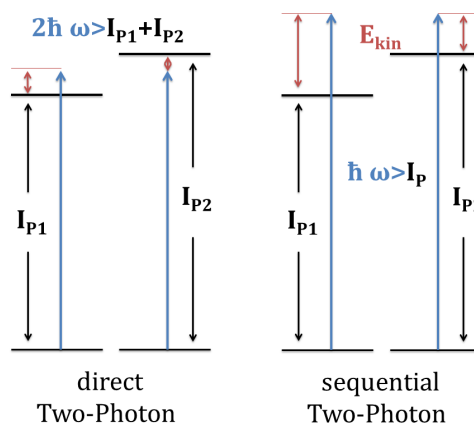


Figure 2.4 – Direct and sequential two-photon two-electron ionization.

situations, when the energy of the second photon is not enough to ionize the ion (figure 2.4 left), but where the sum of both photon energies exceed the sum of the ionization potential of the two electrons. For a detailed description for TPDI in the case of Helium see [51].

One Electron Photoionization Processes

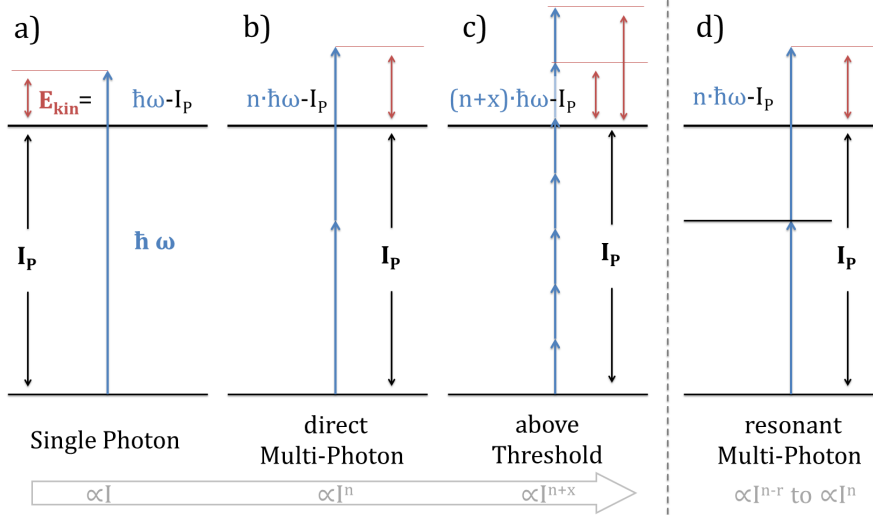


Figure 2.5 – Photoionization processes in the multiphoton regime. The blue arrows symbolized the photon energy which has to overcome the ionization potential drawn in black. The energy difference between photon and binding energy is observed in the electron kinetic energy (in red). The required intensity at a given photon energy is increasing from left to right, indicated by the grey arrow, with the resonant process as an exception on the very right.

If the photon energy is smaller than the ionization potential I_p , a single photon cannot ionize the atom. Then several photons have to be absorbed simultaneously to fulfill the condition $n \cdot \hbar\omega > I_p$ (picture b) in figure 2.5). This *direct non-sequential* multiphoton ionization has a small cross section and, thus, requires a high intensity. The probability for multiphoton ionization rises with the intensity to the power n of simultaneously absorbed photons, see equation 2.38. For optical lasers, the intensity range between 10^{12} W/cm² and 10^{14} W/cm² is called multiphoton regime, as many photons can be absorbed simultaneously at these intensities.

If more photons are absorbed than required for ionization, $n \cdot \hbar\omega > I_p + x \cdot \hbar\omega$ with $n > x > 1$, the electron will carry away the excess energy, which is a multiple of the single photon energy $x \cdot \hbar\omega$ [52, 53] (picture c) in figure 2.5). Such *above threshold ionization* (ATI) was exploited to calibrate the energy scale of the electron

spectrometer, described in this work, by analyzing the discrete excess energies in the photoelectrons created by the simultaneous absorption of photons from a Ti:Sa laser in argon (here, the photon energy was 1.5 eV and the ionization potential for argon is 15.6 eV. Electrons with ten different energies were resolved. From $n \cdot 1.5\text{eV} > 15.8\text{eV} + 10 \cdot 1.5\text{eV}$, it follows that $n=20$ photons were absorbed).

In "resonant" multiphoton ionization a resonant bound-bound transition is included in the photoionization [52, 54] (picture d) in figure 2.5). Resonances significantly enhance the ionization process, such that it is called resonance enhanced multiphoton ionization (REMPI). REMPI is widely used in spectroscopy [55, 56]. If the resonance is hit with monochromatic light, the probability to excite the atom via this resonance is close to one. Then, the absorption is saturated, and a further increase in intensity cannot further increase the absorption probability. Hence, the probability of resonant multiphoton ionization is proportional to I^{n-r} , with r as the number of involved saturated resonances. However, it is closer to I^n when the resonances are not saturated, e.g. because not all photons in a large bandwidth pulse have the appropriate energy.

The transition *rate* in equation 2.37 in a photoionization experiment with N_0 target atoms is often observed by means of the ion yield dN_1/dt .

$$\frac{dN_1}{dt} = N_0 \sigma^{(n)} \left(\frac{I}{\hbar\omega} \right)^n \quad (2.38)$$

Here, the intensity is divided by the energy $\hbar\omega$ to give a dimensionless number of ions when multiplied with the generalized cross section.

The intensity I can be varied by increasing or decreasing the focus size or attenuating the laser beam, respectively. Then, a measurement of the ion yield as a function of the intensity can provide information about the number of absorbed photons. In a double-logarithmic plot of ion yield as a function of intensity, the number of photons is found as the slope of the yield curve, $n = \log(dN_1/dt)/\log(I/\hbar\omega)$. The minimum number of photons necessary for m -fold ionization is the sum of ionization energies divided by the photon energy, $n_{min} = \sum_m (I_P)_m / \hbar\omega$.

When the intensity is rising, all neutral target-atoms will be ionized at some point. Then, a further increase of the intensity will not lead to a higher ion yield of singly-ionized charge states any more. The single-photoionization in the target volume is saturated; the path to full saturation can be described by an exponential decrease of the population of neutral target-atoms. Upon single-photoionization, the

ions in the target volume can absorb another photon. Again this *sequential double photoionization* will saturate as soon as all target-ions are doubly ionized.

For instance, in two-photon double ionization, the ion yield for the sequential two-photon ionization is

$$\frac{dN_2^{seq}}{dt} = N_1 \sigma_{12}^{(1)} \left(\frac{I}{\hbar\omega} \right)^1 \quad (2.39)$$

$$\text{with } N_1(t) = \int_{-\infty}^t N_0(t') \sigma_{01}^1 \left(\frac{I}{\hbar\omega} \right)^1 dt' \quad (2.40)$$

Here, σ_{01} and σ_{12} are the photoionization cross sections for the first and second step, respectively. For completeness it should be noted that two photons may, with much lower probability, also be absorbed simultaneously in a *non-sequential double photoionization* [51], depicted in 2.4

$$\frac{dN_2^{nonseq}}{dt} = N_1 \sigma_{02}^{(2)} \left(\frac{I}{\hbar\omega} \right)^2 \quad (2.41)$$

$$(2.42)$$

So from the number of absorbed photons these pathways cannot be distinguished.

2.2.3.2 Classification of Strong-Field Interactions

The kinetic energy of a free electron driven by an oscillating electromagnetic field is described by the *ponderomotive potential*. It is defined as

$$U_P(E, \omega) = \frac{e^2 E^2}{4m_e \omega^2} \hat{=} \frac{E^2}{4\omega^2} = \frac{I}{4\omega^2} \quad (2.43)$$

where E denotes the electric field, ω the radiation frequency and I the field intensity. The two right terms are, for shortness, expressed in atomic units where $e = m_e = 1$. Obviously, the ponderomotive potential rises linearly with the pulse intensity, and decreases quadratically with shorter wavelength, i.e. with higher photon energy.

For distinguishing between of the "multiphoton" and the "tunneling" (strong-field) regime, the so called *Keldysh (or adiabatic) parameter* γ was introduced [35]

$$\gamma = \frac{T_{tunneling}}{T_{laser\ period}} = \sqrt{\frac{I_P}{2U_P}} \quad (2.44)$$

It compares the time in which tunneling takes place with the time the laser bends the atomic potential to enable tunneling. Since the strong field bends the atomic

potential (see figure 2.6 on the left), this regime is called tunneling regime. In a more practical form, the Keldysh parameter may be written as the ratio between the ionization potential I_P and the ponderomotive potential U_P . Now, γ has been widely used to approximately distinguish between the two regimes by classifying:

$\gamma \gg 1$	multiphoton regime
$\gamma \ll 1$	tunneling regime

Note that this classification is not very sharp and has been intensively discussed in the literature. Nevertheless, it provides good guidance. To illustrate the approximate border line between these regimes, the intensity leading to $\gamma = 1$ for the hydrogen atom if radiated by an infrared laser is calculated: with an ionization potential of 13.6 eV in the focus of a 800 nm laser, the Keldysh parameter becomes one for an intensity of $1.1 \cdot 10^{14}$ W/cm².

2.2.3.3 Strong-Field Effects in the Tunneling Regime

If the intensity is increased above the multiphoton regime, the ponderomotive force of the oscillating electromagnetic field is sufficiently large to modify atomic states and drive electron motions.

Thus, being far away from a "small perturbation", processes in this regime cannot be treated by perturbation theory anymore. One of the most common theoretical approaches to be applied now is the so-called strong-field approximation. Here, interactions with the external field are neglected in the initial state and, in the final state, interactions with the nucleus are considered to be small, such that essentially a free electron is moving in the laser field [57, 58]. Three prominent reaction mechanisms within the tunneling regime should be mentioned.

Bending the potential well and tunneling The oscillating field modifies the potential well, so that the $1/r$ symmetry of the Coulomb potential is broken (figure 2.6). If the oscillation of the field is slower than the tunneling time, electrons may tunnel through the lowered potential barrier [26]. If the potential barrier is bent below the energy level of the electron, the ionization is called above the barrier ionization.

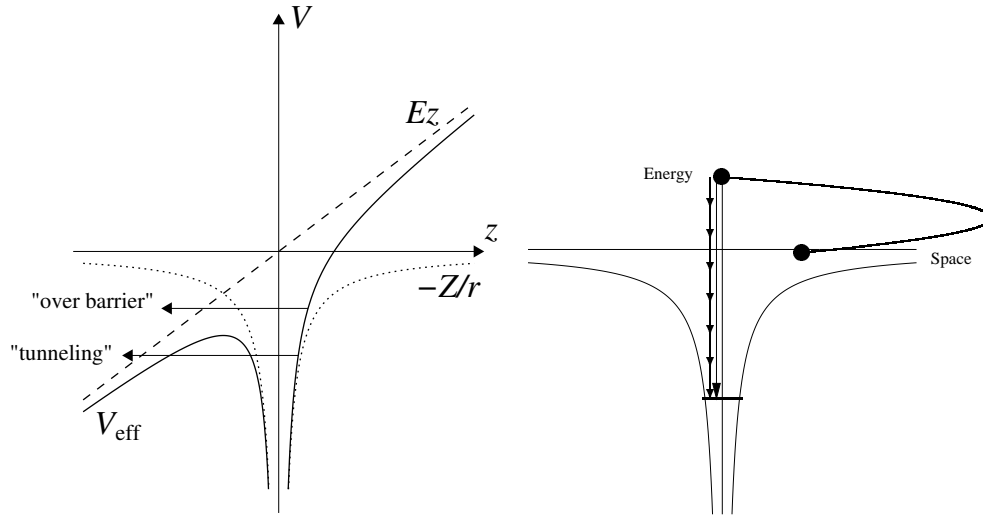


Figure 2.6 – Tunneling ionization and high harmonics generation[1]

Driving electronic motion and HHG When an electron tunnels out of the potential well during the optical pulse, it can be regarded as quasi-free electron with zero energy, being subject to acceleration in the oscillating electric field. Thus, it is first driven away from the atom but then returns after half an optical cycle after ionization. At the parent core, the electron can either scatter elastically, scatter inelastically (and ionize or excite a second electron) or recombine. In recombination, its kinetic energy (as in bremsstrahlung) and energy difference to the bound state (as in fluorescence decays) is transferred to a photon of an energy (odd) orders higher than the initial photon energy. At maximum the photon has an energy of $I_P + 3.17U_P$ which is the upper classical limit for the electron recollision energy. Thus, this process is called high-order harmonics generation (HHG) [59, 60]. With shorter pulse length (down to attoseconds) and higher photon energies (up to XUV) as compared to optical lasers, HHG sources share two important advantages with free-electron lasers. However, even the brightest HHG pulses are currently at least four orders of magnitude lower in peak brightness [61].

Shifting atomic states Atomic states are shifted or, when degenerated, split in external fields. The most prominent examples are the Zeeman effect for atoms in a static magnetic and the Stark effect for the influence of an external static electric field. In high-intensity laser foci, the Stark effect is induced by an oscillating field

¹Source: Lecture notes by Dieter Bauer [62]

and, thus, is called AC-Stark effect. In multiphoton ionization, atomic states, not accessible by an integer number of laser pulses without the presence of an external field, may be shifted by the AS-Stark effect so that the difference to the ground-state becomes an integer multiple of the photon energy. Then, multiphoton ionization proceeds very efficiently via this resonance to the shifted intermediate state as in REMPI discussed above for non-shifted levels [63].

A broader discussion on light-matter interactions in intense laser fields can be found in the review articles [26–28, 36].

2.2.4 Photoionization by Intense X-ray Pulses

2.2.4.1 Multiple Ionization of Inner-Shell Electrons

In the preceding section, the multiphoton and tunneling regime were introduced to evaluate at which intensity the oscillating field starts to disturb the potential barriers and drives the electron motion. Due to the $1/\omega^2$ dependence of the ponderomotive force, strong-field effects are expected to play a negligible role at X-ray energies. Whereas the intensity to yield a Keldysh parameter of $\gamma = 1$ for the hydrogen atom irradiated with 800 nm wavelength was calculated to be $1.1 \cdot 10^{14} \text{ W/cm}^2$ in section 2.2.3.2, at X-ray energies, say 0.8 nm wavelength (about 1500 eV), the required intensity becomes $1.1 \cdot 10^{20} \text{ W/cm}^2$, which is still higher than the values achieved at any X-ray source currently available, including free-electron lasers. This classification puts X-ray photoionization clearly in the multiphoton regime.

At infrared, optical and ultraviolet energies direct multiphoton processes have been discussed in section 2.2.3.1. At X-ray energies, even at high intensities of free-electron lasers, nonlinear X-ray processes are expected to be dominated by *sequential* single-photon single-electron interactions [20, 24, 25].

In section 2.2.2.5 decay mechanisms upon X-ray inner-shell photoionization have been discussed. At high intensities, several sequential photoionization steps may occur, before a decay into the first inner-shell vacancy takes place. Then, multiple inner-shell vacancies are created.

Sequential multiphoton ionization leads to high charge states, where the ratio of the two competing decay mechanisms, Auger and fluorescence decay, may change: The Auger rate depends on the number of available electrons in higher shells to participate in the decay process. Auger decay becomes, therefore, less likely with

increasing charge state during sequential inner-shell ionization. Eventually core-shell excited ions like $C^{4+} 1s^1 2s^0 2p^1$ must solely decay radiatively.

2.2.4.2 Modeling of X-Ray Photoionization

At free-electron lasers two important features have to be addressed by theoretical models: the influence of the chaotic photon statistics (see the experimental section), and the high intensity of the radiation. The basic underlying steps of calculating the atomic response to FEL X-ray pulses are briefly outlined in the following providing references to detailed descriptions.

To account for the photon statistics, the number of photons in a certain mode (wavevector \vec{k} , polarization λ) has to be considered and defines the field configuration. All possible field configurations are summed up in a density matrix, which is evaluated via the (first order) field correlation function [64, 65]. Eventually, integration of this function yields an average number of photons per unit area and FEL pulse. In this way, possible intensity and coherence spikes are considered from pulse to pulse. The chaoticity of the FEL pulse was found to have limited impact on the overall ionization process in the sequential regime, but to become important in certain high-intensity ionization pathways [24]. In the calculations presented in this work, a simple Gaussian shape was assumed for the photon intensity distribution.

The differential cross sections for one photon ionization is calculated with non-relativistic quantum dynamics using first-order perturbation theory. Each cross section is multiplied by the average photon number to give the differential probability for single photoionization by the FEL pulse. The new inner-shell electron binding energy of the resulting core excited state is then calculated with the Hartree-Fock-Slater (HFS) approach [66]. Within the sudden approximation [67], the ionization process is assumed to happen instantaneously and the two appropriate Hamiltonians, before and after ionization, are independent. Then, the double ionization probability is the product of the single-photon ionization cross section of the ground and of the core-excited state. The latter may also relax via Auger or fluorescence decay, and the corresponding decay rates have to be considered within the ionization process. As the differential cross section, these decay rates are calculate within perturbation theory.

Finally, the ionization probabilities and decay rates of intermediate excited states are put into a set of coupled rate equation, which are numerically solved. Those

show the temporal evolution of probabilities to find the target in a certain state. Because photoionization and decay mechanisms constantly shift the charge-state distributions during the FEL pulse, these probabilities are coupled. While the atomic processes (ionization, decay) are treated in the perturbative regime, the overall ionization and relaxation dynamics, described by the coupled rate equations, are non-perturbative.

The accuracy of this modeling is limited by several approximations. First, the electronic structure calculations is based on the Hartree-Fock-Slater method, which does not consider relativistic effects or electron correlation; the difference of the exact and the self-consistent field energy is the correlation energy (CE) [41]. CE calculations, however, have shown little deviations from the HFS results on the level of sophistication needed for the interpretation of the present experiments. For the photoionization and fluorescence rate, the dipole approximation is used, for shake-off ionization the sudden-approximation. At soft X-ray energies the dipole approximation is still plausible. Shake-off is included for the first photoionization step, then the shake-off ratio decreases, and it has no effect on the production of high charge states [68]. Double Auger decay, Auger satellites and impact ionization (such as "knockout" of an outer-shell electron by the inner-shell photoelectron) are not considered in the theoretical model. In rate equations either one or another state is addressed but a superposition of states is not possible. For the experimental parameters of this work, the bandwidth (about 15 eV) is too small for a superposition of different states (about 50 eV apart).

A discussion of this theoretical approach for helium and neon can be found in [24], a general tutorial in [38]. The XATOM toolkit, which was used by S.-K. Son for the calculations, related to this work, is described in [69].

Chapter 3

Experimental Setup

3.1 The Linac Coherent Light Source

The Linac Coherent Light Source (LCLS), the world-wide first hard X-ray free-electron laser, has started operation in fall 2009 with one beamline operational, the "AMO-beamline" for atomic, molecular and optical science. In December 2011, the last of six beamlines was being commissioned. LCLS provides coherent X-rays with pulse lengths between 500 fs and below 3 fs at wavelengths ranging from 1.2 to 22 Å. The offered peak brilliance is almost nine orders of magnitude higher than at conventional synchrotron sources [70] (see figure 1.1). The following sections cover four topics with respect to the design of the LCLS, namely: the electron gun and the accelerator section, the lasing process, the photon diagnostics and, finally, the relevant parameters of the beamlines.

3.1.1 Electron Acceleration in the Linac

The lasing process in FELs is based on the collective interaction of relativistically fast electrons with their own spontaneous emission. For these collective interactions to occur, the electrons have to be confined in a small volume and with similar momenta, that means the six-dimensional phase-space density has to be sufficiently high. The average spread of particle coordinates in position and momentum phase space is called emittance. The lower the electron beam emittance, the higher the photon beam brilliance (defined in figure 1.1). To account for the required low emittance and high beam currents FELs are based on linear accelerators (Linacs) which are single-pass machines. In comparison, synchrotrons consist of a pre-accelerating Linac, a

circular accelerator and a storage ring [11] where the same electron bunch circulates for several days. The FEL was proposed as early as 1971 [71] but the first optical FEL based on sufficient electron beam emittance could only be realized in 2001 [72].

3.1.1.1 Electron Sources

LCLS uses the accelerator units in the last kilometer of the 3-km-long SLAC Linac. At kilometer two, the electron beam is created 35° off-axis in a photocathode radio frequency (RF) gun, where a copper cathode is illuminated by 3-ps-long UV pulses with a 30 to 120 Hz repetition rate which thereby defines the repetition rate of the X-ray pulses. With stabilized irradiation of the copper cathode, the relative electron charge stability amounts to 1.1% root mean square (rms, the quadratic mean) at 1 nC [73]. The injector is typically operating with a lower charge of 0.25 nC and, then, provides a 35 A peak current and a transverse emittance of less than 1 mm rms [70].

Electron Bunch Length Similar to streak cameras (see figure A.4) the electron bunch profile can be derived by directly *streaking* the electron beam using an RF deflecting field [73]. In a transverse-deflection cavity (TCAV3 in figure 3.1), located after the second compressor, the electron beam is deflected by S-band RF pulses onto a phosphor screen [74]. From the spatial distribution the electron bunch length can be measured down to 10 fs [75]. This deflection measurement is very sensitive to the deflecting field and a precise calibration is essential; for example between two calibration procedures a shift in the field strength of up to 30% was found [76]. If the field strength was not recalibrated a 30% offset in the electron bunch length would have been measured.

3.1.1.2 Accelerator

At LCLS the electron bunch is accelerated by the S-band (2.856 GHz) Linac, where the RF-fields are fed in from klystrons and form a standing wave in the cavities for resonant acceleration. From the injector, the electron beam enters the main Linac axis with 135 MeV and is further accelerated to 250 MeV before passing the first bunch compressor chicane (BC1 in figure 3.1), which shortens the bunch and thereby magnifies the peak current. The two bunch compressors combined cause a 100-fold increase in peak current to 3.5 kA.

The maximum emittance and, thus, the compressibility is limited by the pulse charge. At low-charge mode operation, that is a 20 pC instead of the typical 0.25 nC, the electron bunch can be compressed to a minimum bunch length of few femtoseconds [77].

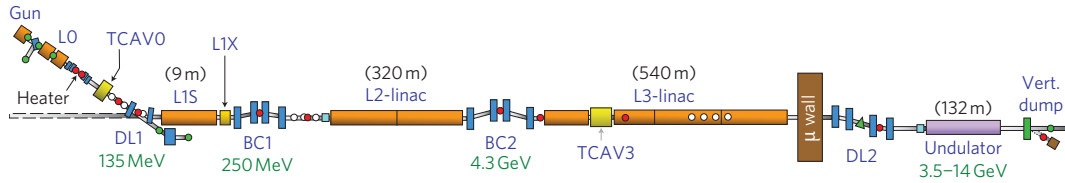


Figure 3.1 – Layout of the LCLS from the electron gun to the main dump, with two bunch compressors, BC1 and BC2, and a 132 m long undulator¹.

3.1.2 Light Generation by the Undulators

A uniformly moving charge creates both, an electric and a magnetic field. In order to produce an electromagnetic wave, it is necessary to have charge acceleration. The generation of electromagnetic waves by accelerated charges was predicted by Maxwell in 1864 and experimentally demonstrated by Hertz in 1886. In a Hertzian dipole antenna, a radio frequency voltage drives a charge oscillation in a conductor, where the electrons move according to the force of the alternating electric field.

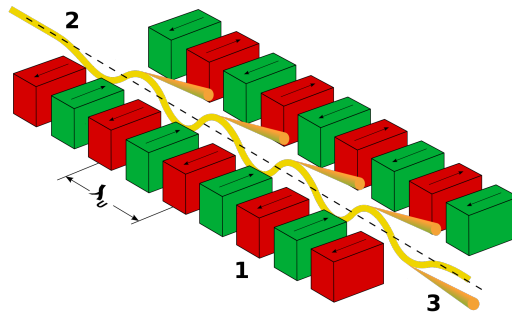


Figure 3.2 – Undulator working principle². An electron beam (2), deflected in an array of permanent magnets (1) of period λ_U , is radiating electromagnetic waves (3).

In an undulator, a charge oscillation is induced by an array of permanent magnets with alternating poles (see figure 3.2), where an electron beam experiences a Lorentz

¹Source: P. Emma et al. Nature Photonics 4, 641-647 (2010). Copyright by the Nature Publishing Group.

²Source: Wikipedia: The Free Encyclopedia. Wikimedia Foundation, Inc.

force, $\vec{F}_{Lorentz} = q\vec{v} \times \vec{B}$, perpendicular to the external magnetic induction field \vec{B} and its velocity vector \vec{v} . In the reference frame of the electron the emission pattern is that of a dipole antenna. The electron velocity, however, is relativistic and, thus, the radiation emission pattern has to be Lorentz-transformed into the laboratory frame of reference. Then, the emission pattern is very much tilted towards the direction of motion with an opening angle of $\pm 1/\gamma$, where γ is defined as

$$\gamma = \frac{1}{\sqrt{1 - \beta^2}} = \frac{1}{\sqrt{1 - (\frac{v}{c})^2}} \quad (3.1)$$

where v is the electron velocity and c the speed of light.

The period of the magnet arrangement is called λ_u and the deflection of the electrons within the array of permanent magnets is described by the deflection parameter K

$$K = \frac{e}{2\pi m_e c} \lambda_u B_0 = 0.934 \cdot \lambda_u [cm] \cdot B_0 [T] \quad (3.2)$$

A derivation of this and other formulae mentioned in this section can be found in the textbooks on synchrotron radiation [46] and free-electron lasers [78].

The deflection angle is approximately $\pm K/\gamma$. For undulators, the maximum deflection of the electrons is within the opening angle of the radiation ($\pm 1/\gamma$), so $K \approx 1$. Hence, the radiation emitted at different points on the electron trajectory can overlap and increase the irradiated power. For constructive interference the path difference between the light wave, emitted at point A, and the slower ($<c$) electron bunch has to be a multiple n of the wavelength λ_n at point B, one undulator period λ_u later, where the electron bunch spatially overlaps with the light it had generated at point A. From this interference condition the undulator equation is derived, which connects wavelength λ_n of the n -th harmonic, the undulator period λ_u , the electron velocity described by γ and the deflection parameter K for radiation within an opening angle θ to the beam axis

$$\lambda_n = \frac{\lambda_u}{2n\gamma^2} \left(1 + \frac{K^2}{2} + \gamma^2 \theta^2 \right) \quad (3.3)$$

Accordingly, the wavelength of the radiation can be chosen by the undulator geometry (K) and the electron kinetic energy ($E_{kin} = \gamma m_e c^2$), which is tunable in the electron accelerator. In addition to the fundamental wavelength $n = 1$, there are higher harmonics with $n \in N$, but in forward direction only odd harmonics are observed. In an undulator with N_u periods the bandwidth of the fundamental and

its harmonics is

$$\frac{\Delta\lambda_n}{\lambda_n} = \frac{1}{n \cdot N_u} \quad (3.4)$$

The interference condition in equation 3.3 is valid for individual electron trajectories, but does not imply coherent radiation of the entire electron bunch. The electron bunch is orders of magnitude longer, i.e. $24 \mu\text{m}$ (or 80 fs [73]), than the wavelength in the optical and X-ray regime. To radiate *in phase*, which amplifies the radiant power dramatically ($\propto N_{electrons}^2$ instead of $\propto N_{electrons}$ with typically $N_{electrons} \approx 10^9$), the electron bunch has to be sliced into microbunches with elongations in the order of the wavelength. This so called microbunching is induced by the interaction of the electron bunch with its own radiation (see appendix A.1.1). Since the microbunching has to be induced by initially uncorrelated, spontaneously emitted photons, such a light amplification is called self-amplified-spontaneous-emission (SASE). Because SASE is based on shot noise, fluctuations in the generated X-ray beam appear from shot to shot [79–81]. In order to avoid shot-to-shot fluctuations, seeding schemes are planned for future FELs, see appendix A.1.2 for further details. For SASE, the interaction of the electron beam with the light field must be sufficiently long and intense, so that long undulators and electron beams with high peak current, small energy spread and low emittance are required.

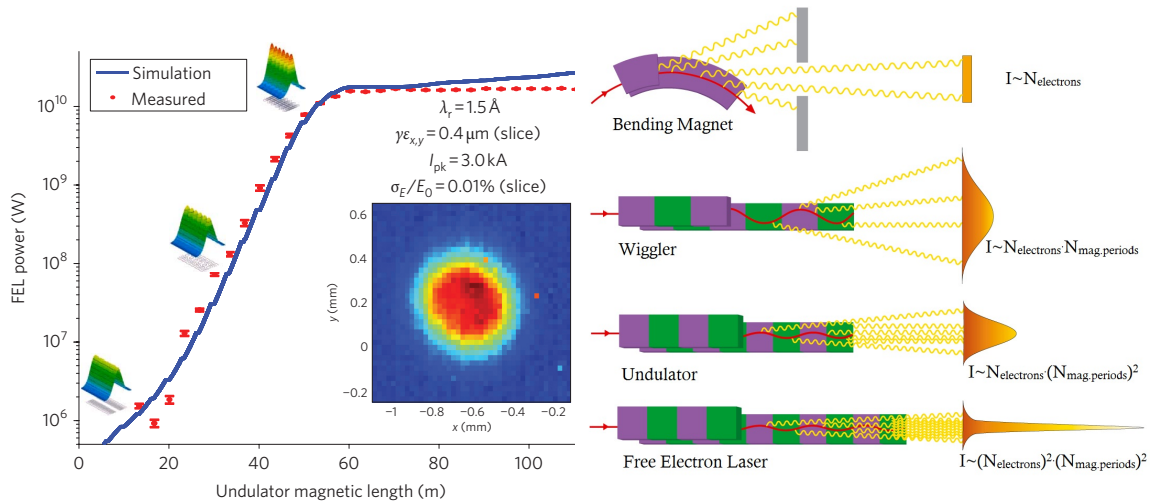


Figure 3.3 – LCLS gain length¹.

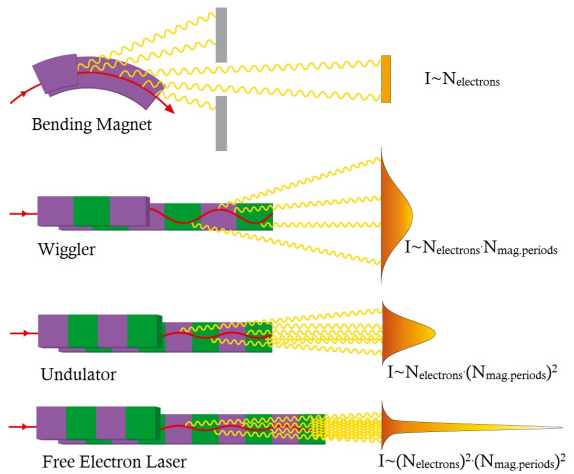


Figure 3.4 – Synchrotron-light sources².

In figure 3.3, the gain length of the LCLS is depicted along with a sketch illustrating microbunching. The gain length is defined as the distance over which the power increases by $e = 2.72$ and critically depends on the transverse emittance at the entrance of the undulator. The gain length of LCLS is 3.5 m for hard X-rays (1.5 Å) and 1.6 m for soft X-rays (15 Å), saturation occurs at 60 m [70] (for 1.5 Å) roughly the 20fold gain-length as predicted by theory [81]. The entire undulator system at LCLS is 132 m long consisting of thirty-three 3.4 m long undulator segments with an undulator period of $\lambda_U = 3$ cm, full gap height of 6.8 mm and a undulator deflection parameter of $K=3.5$, corresponding to a magnetic field of 1.5 T [70].

Figure 3.4 schematically compares the magnetic arrays, emission pattern and irradiated intensity of different synchrotron-light sources. As a result of microbunching, electrons in FEL undulators radiate in phase and the radiated intensity increases not only linearly with the number of radiating electrons (as for wigglers and undulators from synchrotrons) but quadratically, which gives an enhancement of about nine orders of magnitude in peak intensity.

3.1.3 Diagnostics

To date, all four operating short-wavelength FELs, those operating in the extreme ultraviolet (XUV) [82, 83] as well as those in the X-ray regime [70, 84], are based on self-amplified spontaneous emission implying significant shot-to-shot fluctuations. To sort the experimental single-shot data, an elaborated photon beam diagnostics is required.

3.1.3.1 Photon Energy

With a fixed undulator gap, the photon energy is set by the electron energy, adjustable in the accelerator (see equation 3.3).

At LCLS, the photon energy has a bandwidth of 0.2% to 1% (FWHM) and a photon energy jitter ("wavelength stability") of 0.2% (rms) [70]. In figure 3.5 the bandwidth is marked in red, the jitter in green. The blue curves illustrate a single-

¹Source: P. Emma et al. *Nature Photonics* 4, 641-647 (2010). Copyright by the Nature Publishing Group. and S.V. Milton et al. *Science* (New York, N.Y.) 292, 2037-41 (2001). Copyright by the American Association for the Advancement of Science (AAAS)

²Source http://www.desy.de/forschung/forschungsbereiche/forschung_mit_photonen/einblick/lichterzeugung, slightly changed

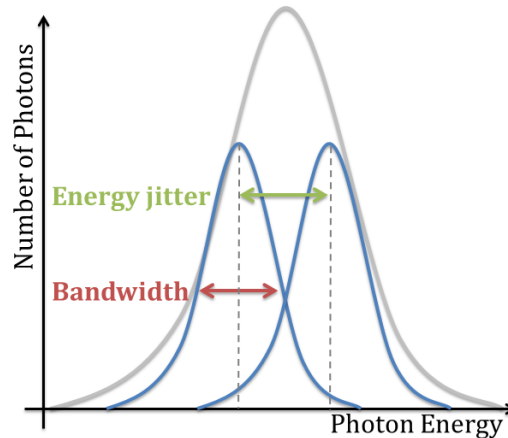


Figure 3.5 – Photon energy bandwidth and energy jitter.

shot spectrum, the grey curve the averaged spectrum. The bandwidth is found in every shot and, e.g., plays a role for energy resolution of photoelectrons and for the accessibility of narrow transitions (resonances). The jitter shifts the total photon energy distribution per shot. The jitter is caused by varying start points of SASE in the undulator. It is monitored shot-by-shot and can be eliminated by sorting routines a posteriori.

Omnipresent spontaneous radiation occurs as surrounding halo of the FEL beam [85]. Higher-energy spontaneous undulator radiation, Bremsstrahlung background radiation and higher harmonics are suppressed by the limited reflectivity of the steering mirrors to experimental hutches. At the AMO beamline, the second harmonic contributed 0.01% and the third-harmonic content was found to be 1% of the total energy over the full tuning range (0.8-2 keV) [20]. The high-harmonic content is very critical for unambiguously identifying very rare nonlinear direct two- or multiphoton absorption.

3.1.3.2 X-Ray Pulse Length

The X-ray pulse length is varied via the electron bunch length and its measurement provides an estimate of the former (see section 3.1.1.1). The actual photon pulse length, however, has been found to be shorter does not necessarily match the electron bunch length, as the X-ray pulses are generated in a highly collective process of lasing within the electron pulse [86, 87].

Various approaches to determine the FEL-photon-pulse length are summarized and compared to the nominal value (given by the electron bunch length) in table

3.1, a description of these approaches is given in the appendix A.1.3.

Measured at LCLS		
Measured by	Electron bunch length	X-ray pulse duration
L. Young et al.[19]	80 fs	40 fs or less
Ratio of double- to single-core-hole formation in neon		
S. Hau-Riege et al. [88]	300 fs, 150 fs, 70 fs	70 fs, 60 fs, 40 fs
Statistical analysis of single-shot photon energy spectra		
S. Düsterer et al. [89]	175 fs, 75 fs	120 fs, 40 fs
Laser-assisted Auger decay in the X-ray regime (sidebands)		
R. Kienberger et al. [90]	<10 fs	<5 fs
NIR streaking (photo-electron momenta)		
A. Cavalieri et al. [91]	>40fs	analysis in progress
THz streaking (photo-electron momenta)		
Measured at FLASH and SCSS		
Autocorrelation of the split FEL beam in an interferometer [92, 93]		
Intensity autocorrelation in non-linear multiphoton-ionization [94–97]		

Table 3.1 – Measurements of the X-ray pulse duration

It turns out for various independent measurements, that the X-ray pulse length was found to be at least 40% shorter than the electron bunch.

3.1.3.3 Pulse Energy

Before describing the pulse energy measurement at LCLS, some clear definitions should avoid any confusion about three terms, which are often used freely in the context of quantifying radiation levels:

Pulse energy is the total energy content of a pulse, i.e. the sum-energy of all individual photons:

$$\text{pulse energy} = \text{number of photons} \cdot \text{energy per photon} \quad (3.5)$$

The maximum pulse energy at LCLS in 2009 to 2011 has been 3 mJ at 2 keV photon energy (about 10^{13} photons).

Fluence is the total energy delivered per area:

$$\text{fluence} = \frac{\text{pulse energy}}{\text{area}} \quad (3.6)$$

Assuming a $3 \times 3 \mu\text{m}^2$ X-ray focus and 18% beamline transmission at 2.5 mJ pulse energy the fluence amounted to $44 \mu\text{J}/\mu\text{m}^2$ during the 2011 measurements (see section 4.1).

Intensity, also called irradiance or radiative flux, is the energy per area within the period of the pulse:

$$\text{intensity} = \frac{\text{pulse energy}}{\text{pulse length} \cdot \text{area}} \quad (3.7)$$

The intensity with a pulse energy of 2.5 mJ, a pulse length of 100 fs, a $3 \times 3 \mu\text{m}^2$ X-ray focus and 18% transmission is $5 \cdot 10^{16} \text{ W}/\text{cm}^2$.

3.1.3.4 The LCLS Gas Monitor Device

At LCLS, two pulse energy detectors to characterize hard X-ray free-electron-laser pulses are permanently installed upstream of the experimental hutches.

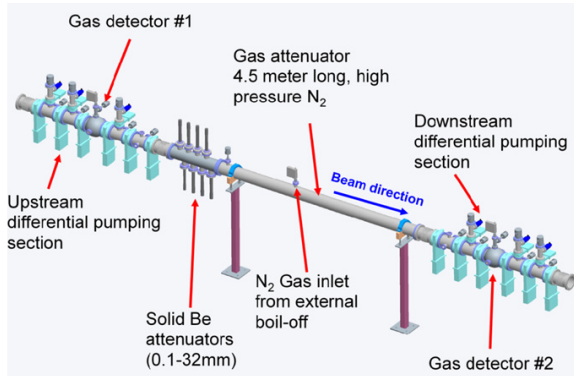


Figure 3.6 – The LCLS attenuator system¹.

They are positioned in the front and in the back of an attenuation chamber, where the incident pulse energy can be reduced, up to an attenuation of 10^4 , either by adjusting the nitrogen gas pressure (up to 16 mbar) within the 4.5 m long beamline section or by inserting a choice of seven beryllium plates of various thickness (0.5, 0.5, 1, 2, 4, 8 and 16 mm) resulting in an adjustable total thickness of 0 to 32 mm [75]. The solid attenuators, however, significantly disturb the wavefront of the beam, as imprint studies have demonstrated [98, 99]. With both detectors working in parallel the

¹Source: S. Moeller et al. Nuclear Instruments and Methods in Physics Research Section A: Accelerators, Spectrometers, Detectors and Associated Equipment 635, S6-S11 (2011). Copyright by Elsevier Ltd.

²Source: S. Hau-Riege et al., PRL, 105, 043003, 2010. Copyright by the American Physical Society.

incident as well as attenuated pulse energy is monitored simultaneously from shot to shot and their ratio determines the transmission at certain attenuation. The transmission can also be calculated from the attenuation (equation 3.8). For the beamline transmission - the actual transmission in the experimental chamber - see section 3.1.4.

$$\text{transmission} = \exp\left(-\frac{\text{absorption length} \cdot \text{gas pressure}}{\text{energy dependent constant}}\right) \quad (3.8)$$

The pulse energy measurement is based on the X-ray induced photoluminescence of nitrogen in a 30 cm long chamber (figure 3.7). The upper bound for the gas pressure is about 2.5 mbar and is regulated by the gas inlet which competes with pumping. At 8.3 keV photon energy only 0.06% of the photons are absorbed, at lower photon energy a higher cross section increases the absorption and the gas pressure has to be reduced. Photons are mainly absorbed through K-shell photoionization which are rapidly (few fs) followed by Auger relaxations. Both, the photoelectrons and the Auger electrons, are confined in the 200 G axial magnetic field of an external solenoid in order to increase the residence time of the electrons in the nitrogen gas. Thus, their kinetic energy can effectively be transferred to the nitrogen molecules via molecular excitation and ionization until termination on the chamber walls. Electron impact ionization yields secondary electrons, while molecular excited nitrogen relaxes under radiative decay of 300 nm to 400 nm [100]. Eventually, the UV light is detected and amplified by two photo multipliers positioned parallel and perpendicular to the polarization vector of the FEL beam and shielded by a near-UV filter transparent to light between 300 and 390 nm [101, 102].

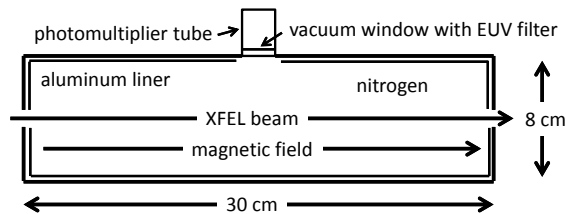


Figure 3.7 – Setup of the LCLS gas monitor device².

The measurement of the UV radiation provides the relative shot-to-shot pulse energy. Thereby gas pressure, magnetic field and photon energy have to be monitored and stabilized to the recommended operating range. The photon pulse energy is

estimated by measuring the electron beam energy loss in the undulator and is taken for an absolute calibration of the gas detectors.

3.1.3.5 The ASG Intensity Monitor

A second intensity monitor has been installed downstream of the experimental chamber as back-up option and to check the LCLS GMD on its linearity. In contrast to the LCLS luminescence detector, it is based on the photoionization of a gas at a low target density (the same effect is exploited in the DESY gas-detectors designed for the use at the XUV FEL, FLASH, and the upcoming X-ray FEL, the European XFEL [103]).

At the Japanese XUV-FEL, SCSS, and X-FEL, SACLA, a third detector type, a cryogenic radiometer, is used. It is based on the calorimetric technique, that means the temperature rise of a cavity absorber, which corresponds to the radiant power of the FEL, is measured [104].

The intensity monitor was mounted in a CF63 double cross between the CAMP endstation and the boron carbide (B_4C) beam-stop. The gas pressure was kept low (10^6 mbar) to avoid any gas leakage through the 5 mm aperture into the experimental chamber. The six ports of the cross were distributed to: the incoming beam, the beam stop, the intensity monitor, a needle valve for gas inlet, a pressure gauge and a YAG-crystal on a movable linear manipulator to monitor the beam position. Figure 3.8 shows the setup and position within the vacuum tubing. The intensity monitor is built as time-of-flight spectrometer, where ion acceleration and drift region are chosen to fulfill the McLaren geometry for optimized time-of-flight resolution [105], also called time focusing geometry. Accordingly charged particles starting from the interaction point in the middle of the 40 mm acceleration region pass an acceleration length of 20 mm before they enter the field-free 40 mm long drift region. Different voltage regions are separated by copper meshes. The spacing between each electrode is 7 mm. Ions, extracted with 200 V across the total extraction region i.e. 62 V/mm, are amplified by a commercial¹ open MCP detector with two V-stack multi-channel plate and a single metal anode (for a description of MCPs, see section A.2.4 in the appendix). The amplification is 10^7 and decoupled MCP signals are further amplified by a fast pulse preamplifier².

¹TOPAG MCP Detector MCP-MA33/10

²Philips scientific fast pulse preamplifier model 6954ds

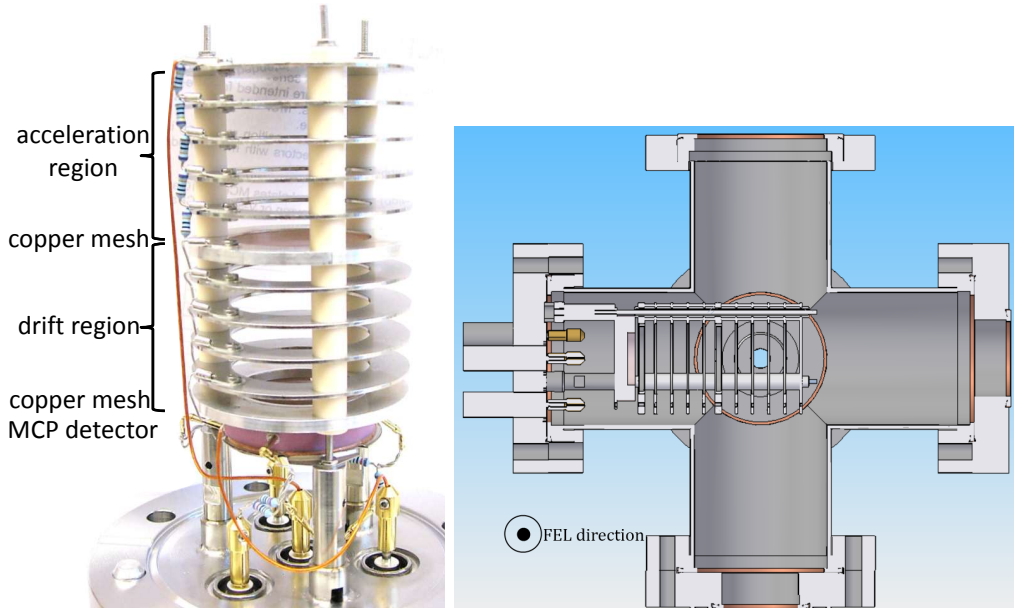


Figure 3.8 – Intensity monitor within the CF63 double cross. On the left the time-of-flight spectrometer in McLaren geometry and V-stack MCP detector is pictured, on the right the mounting of the intensity monitor.

Located at more than 1m distance from the beam focus in the CAMP endstation, the fluence is estimated to be sufficiently low to suppress any two photon absorption. Thus, the integrated ion yield is anticipated to be linearly proportional to the pulse energy. Figure 3.10 depicts a scan over the entire available pulse energy. The time-of-flight spectra are drawn on the x-axis for pulse energies between 0 mJ and 2.75 mJ in steps of $30 \mu\text{J}$ on the y-axis. The incident photon energy was set to 1200 eV, the pulse length to 150 fs and the working gas pressure in the double cross to $3 \cdot 10^{-6}$ mbar.

Due to its high cross section (see figure 3.9) at X-ray energies, xenon was chosen as target gas. In the charge-state spectrum, singly, doubly and triply charged xenon is nearly absent as M-shell photoionization is followed by a cascade of Auger decays which increases the final charge state. In addition, the MCP detection efficiency decreases for lower charged ions [109]. The depicted spectrum in figure 3.10 starts with the Xe^{4+} peak at about 4800 ns which, as well as the Xe^{5+} peak, remains almost of constant peak-height throughout the pulse energy scan. The main feature for Xe^{6+} and Xe^{7+} is the significant decrease, which coincides with an increase of the neighboring higher-charged ion (also see figure 3.12). The dominant peak in the spectrum is Xe^{8+} , which just depletes with the rise of Xe^{9+} at the highest pulse

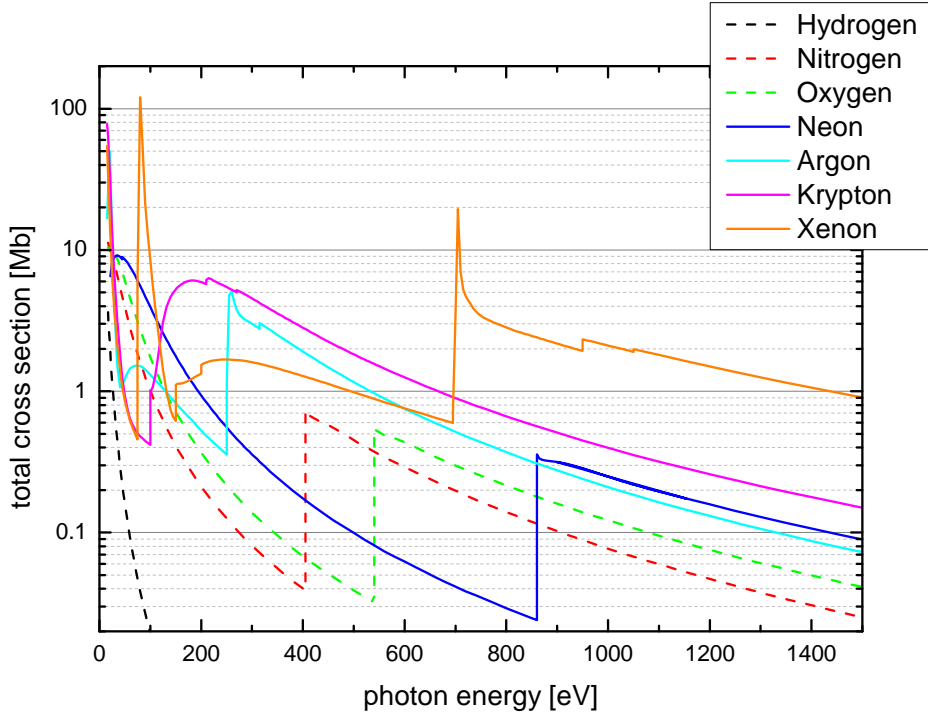


Figure 3.9 – Calculated total cross sections of rare and typical residual gases [106–108].

energies. No depletion is observed for Xe^{9+} since the highest charge state, Xe^{10+} , is detected in negligible amounts. In a 44 eV to 1300 eV photon energy scan at the TERAS synchrotron radiation facility, Saito [110] reports a maximum charge state of Xe^{8+} , which is in agreement with the charge-state distribution measured using the FLASH GMD at the LCLS SXR beamline [111]. In contrast, Carlson [112] shows an ion yield up to Xe^{10+} for photoionization of 3s, which is accessible at 1200 eV incident photon energy, and Mukoyama [113] measured even small yields of Xe^{11+} at 4.5 keV, which is still beyond the L-shell ionization threshold.

Thus, charge states above Xe^{8+} reported here, are attributed to 3s and 3p photoionization, which then decays with enhanced double Auger and autoionization processes as compared to 3d ionization at 800eV. Without any focus characterization and detector efficiency calibration possible during short experimental runs, a quantitative analysis of the individual peak ratios in the time-of-flight spectrum was not undertaken.

Residual gas contributes to the spectrum as seen as C^{1+} (from carbohydrates), N^{1+} , O^{1+} , O^{2+} , O^{3+} and H^{1+} . The light peak at the beginning of the spectrum

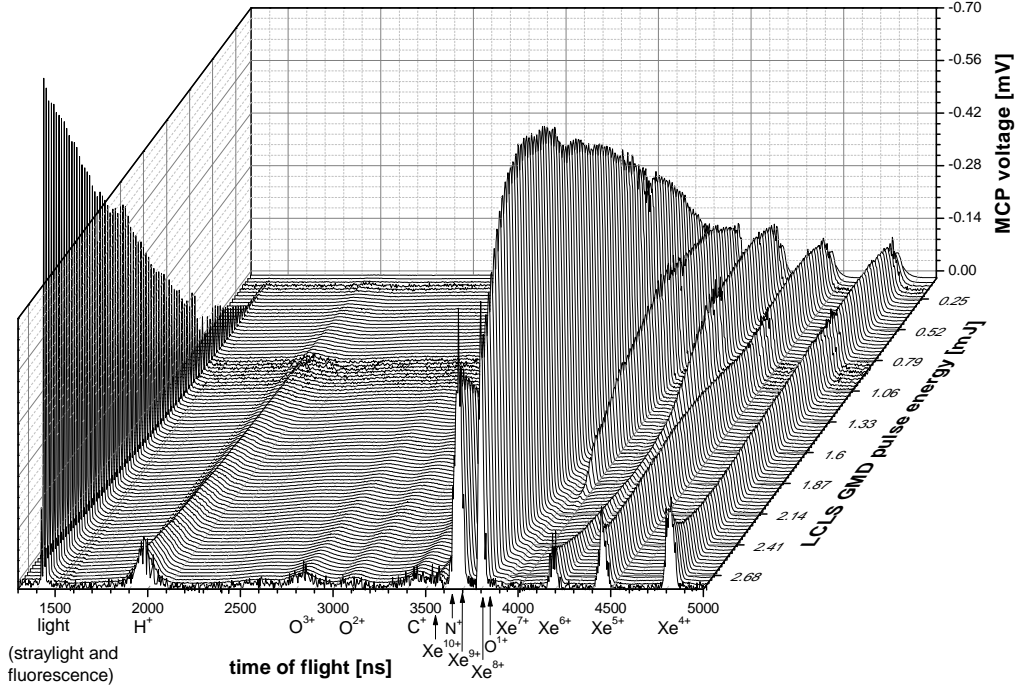


Figure 3.10 – Xenon time-of-flight spectra (normalized on the number of shots) vs. pulse energy (measured by the LCLS GMD).

may not only come from stray light but also from fluorescence-photons created by the beam when impinging on the solid beam stop.

To cross calibrate the LCLS gas monitor device and the ASG-intensity-monitor, the ion yield for protons from the residual gas and Xe^{9+} from target gas is plotted against the GMD pulse energy in figure 3.11. To determine the ion yield, the proton and Xe^{9+} peaks were integrated, normalized to the number of integrated bins and the non-zero baseline was subtracted in the shot to shot time-of-flight spectra. The resulting distribution of peak heights for every pulse energy interval was fitted with a Gaussian-shaped curve to yield mean and standard deviation.

The cross calibration shows good agreement between both pulse energy measurements for values between 0.2 mJ and 1.8 mJ. In that region two additional measurements, one by means of an electron loss scan of electrons kicked on various orbits in the undulator and another one by the *Total Energy Monitor (TEM)*, a bolometer, which measures the total energy of each pulse based on the temperature rise in a 0.5 mm Si substrate [114], have found a similar good linearity of the LCLS GMD (at 8.3 keV) [75].

In figure 3.11, the mean height of the integrated peaks increases linearly with

pulse energy as indicated by the dark blue lines. The x-scale on top of the graph was chosen to match both pulse energies in the linear region. However, at about 1.8 mJ the ion yield exceeds the interpolated pulse energy. This behavior is in very good agreement with a previous calibration curve performed by the FLASH GMD (figure 3.11 right side) and proofs a saturation of the LCLS GMD at high pulse energies. Considering this recalibration, a pulse energy of 2.5 mJ measured by the LCLS GMD becomes 3.5 mJ, 2.75 mJ becomes 4.25 mJ.

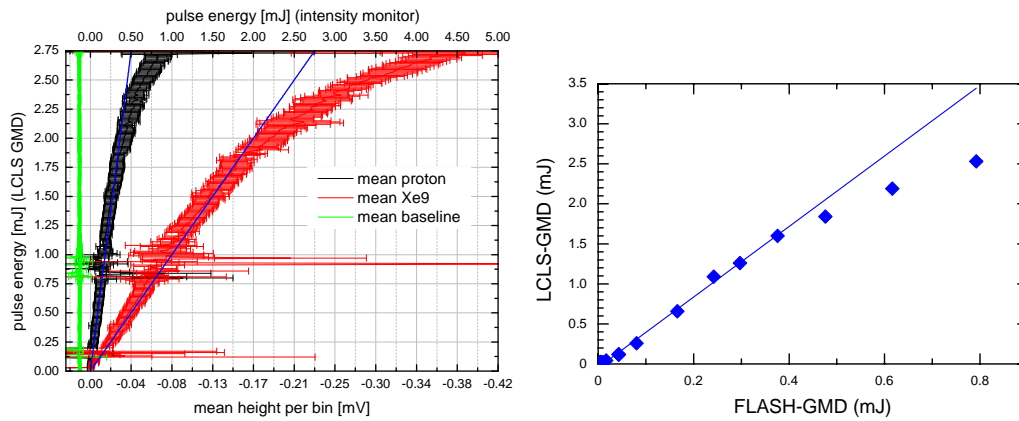


Figure 3.11 – Left: Average photon pulse energy measured by the LCLS gas detector versus the integral of H⁺ (in green) and Xe⁺⁹ (in red) peaks (normalized to the number of integrated bins). The error bars are derived from the standard deviation of the peaks. The dark blue line interpolate the linear region of the curves. The upper x-axis-scale is chosen to match the interpolated line of the Xe⁺⁹ curve to the pulse energy scale. Right: LCLS GMD pulse energy versus the pulse energy measured by the FLASH GMD [111].

Finally, the baseline-corrected ion yield for all peaks of the spectrum is drawn in a double logarithmic plot with recalibrated pulse energy (figure 3.12). For the recalibration the experimental proton yield is divided by a constant factor so that the proton yield-curve has a slope of one, assuming that an proton is liberated upon one-photon absorption. Then, up to 0.3 mJ, all but the Xe⁺³ curve rise linearly. As the ion yield per shot exceeds two units on the y-axis, saturation of the next lower ion charge state occurs. Interestingly, the ion yield does also seem to increase again, when the next higher ion charge state is depleted and falls below the level of two units on the y-axis.

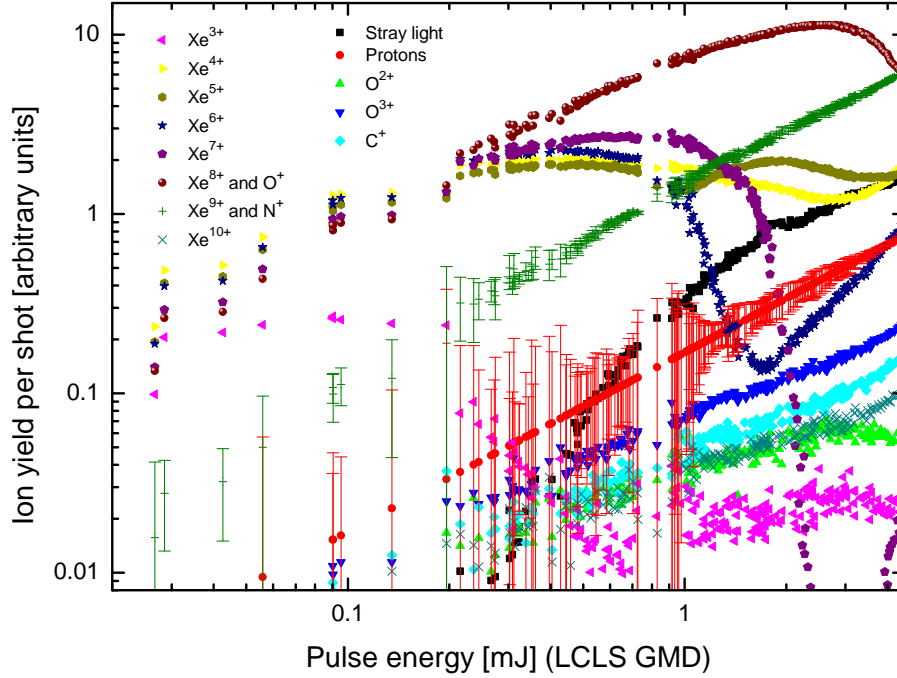


Figure 3.12 – Xenon ion yield vs. pulse energy measured by the ASG intensity monitor. The pulse energy is recalibrated by the recorded proton yield.

3.1.4 Beamlines

The experiment described in this thesis was performed at the AMO beamline. In table 3.2 all currently available beamlines are listed.

The AMO beamline went online first to gain experience on fundamental processes in the interaction of the ultra-intense X-FEL light with atoms and molecules. The X-ray beam is reflected into the AMO beamline by three boron-carbide (B_4C) coated silicon wafers (SOMS, see figure 3.14) with nominal reflectivity of 0.921, 0.931 and 0.898 at 800 eV, 1050 eV and 2000 eV, respectively [19] (figure 3.19), and focused by a set of Kirkpatrick-Baez parabolic-curved grazing-incidence mirrors of the same material. The reflectivity sharply decreases at about 2 keV. So the K-edge up to neon and the L-edge up to krypton are accessible. High-harmonics are efficiently suppressed by the limited reflectivity, which is favorable when non-linear multiphoton ionization is investigated.

From the nominal reflectivity R of the five mirrors, the maximum total beamline transmissions is calculated to be R^5 , that is 0.663, 0.699 and 0.584 for the above photon energies, but the measured absolute transmission turned out to be significantly

lower:

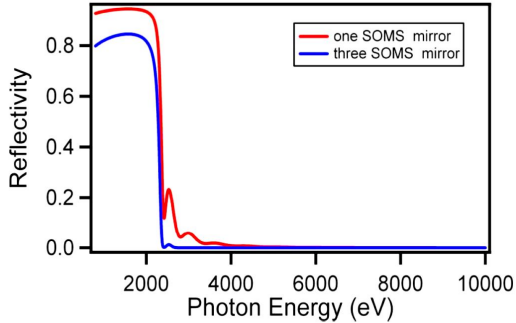


Figure 3.13 – Reflectivity of the Soft X-ray Offset Mirror System, that delivers X-rays to the SXR and AMO beamlines.

the FLASH GMD positioned downstream of the AMO endstation showed pulse energies from 12% to 15% of the pulse energy determined by the LCLS gas monitor upstream of the first steering mirror. This surprisingly low value might be due to additional transmission losses in the beamline or by a positive offset in the LCLS GMD.

If the focal spot size can be assumed from other techniques (see next section 3.1.4.1), the transmission can be inferred from fluence-dependent ion charge-state yields measured in the main experimental chamber. For neon at 800 eV photon energy the charge-state spectra matched best when a transmission of $R^5/3 = 20\%$ was multiplied to the pulse energy determined by the LCLS GMD [19]. For the CAMP endstation (see section 3.2) a similar approach was undertaken to derive the transmission (see figure 4.1).

The other five beamlines at LCLS are summed up in the following table (3.2). The abbreviation is explained, further reading cited and their purpose indicated. Figure 3.14 depicts the beam line layout in the experimental halls and the steering optics.

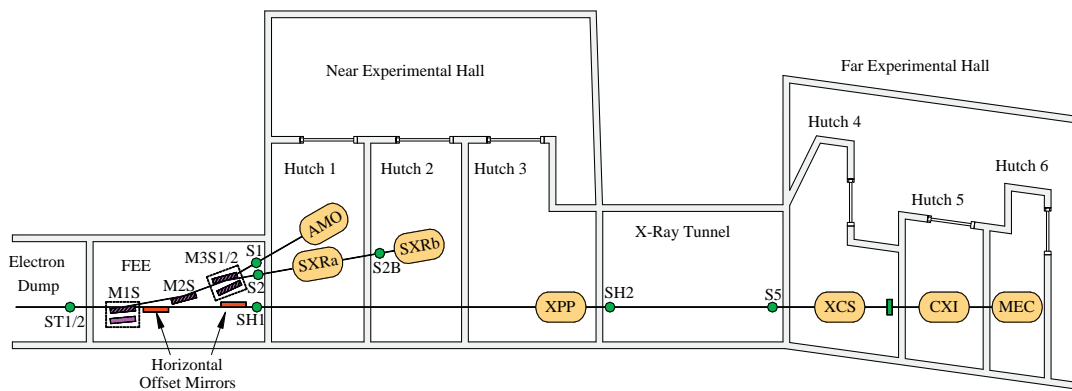


Figure 3.14 – The LCLS photon beam line layout with instrument stations¹ [75].

Atomic, Molecular and Optical Science (AMO) [115] Soft X-rays, high resolving electron and ion spectroscopy, CDI and pump-probe
Soft X-ray Research (SXR) [116] Monochromatic or full non-monochromatic soft X-ray beam, various endstations
X-ray Pump Probe (XPP) [117] Optical laser pump, hard X-ray probe; X-ray scattering shows structural changes
Coherent X-ray Imaging (CXI) [118] Image single sub-micron particles in a hard X-ray focus of 0.1 μm diameter
X-ray Correlation Spectroscopy (XCS) [119] Hard X-ray scattering in condensed matter systems; X-ray - X-ray pump-probe
Matter in Extreme Conditions (MEC) [120] High power optical laser beams pump, hard X-ray probe of very dense matter

Table 3.2 – Beamlines and their particular purpose at LCLS [121]

3.1.4.1 Focus Size

Focus size and fluence are crucial parameters for the majority of experiments presently performed at FEL sources. Both parameters directly alter the power density at the target. They are strongly influenced by the optical system upstream of the experiment due to its focussing and transmission properties. The multi-photon interaction investigated in this work is very sensitive to the power density and the focal volume.

The focus size can either be determined in a designated invasive experimental set-up or traced back from calculated charge-state distributions of small atoms (e.g. Ne), which are fit to data at given focus size. In an intensity scan, the onset of saturation of ion yields for low charge states can also provide a direct estimate of the focus size [122].

Three invasive methods to characterize the spatial beam profile have been used at FELs so far [123]. In the XUV region a direct imaging of the beam wave-front and intensity distribution through the pinholes of a Hartmann-sensor was possible [124]. The pinhole mask in front of a CCD separates the wave-front into evenly spaced point sources, where the local tilt of the wave-front across each pinhole can then be

¹Source: S. Moeller et al. Nuclear Instruments and Methods in Physics Research Section A: Accelerators, Spectrometers, Detectors and Associated Equipment 635, S6-S11 (2011). Copyright by Elsevier Ltd.

calculated from the position of the spots on the CCD and the intensity distribution from the brightness of each spot. This method requires that several pinholes are illuminated and, thus, cannot be applied in the very focus of the FEL beam. At X-ray energies the lack of commercially available fast CCD cameras has hindered this approach so far.

The XUV or X-ray light can be converted to visible wavelengths by luminescence crystals or phosphorescent coating on a transparent substrate. Then, the spot size, magnified by a microscope, is easily measurable with commercial CCDs. Owing to radiation damage and limited optical resolution, the focus should neither be too intense nor too small.

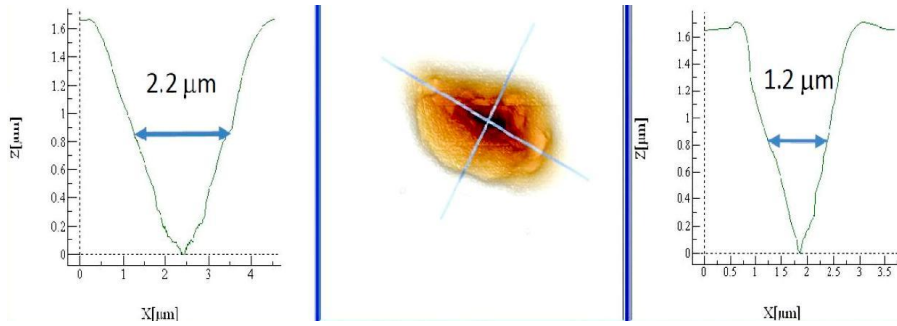


Figure 3.15 – Imprint studies in the HFP chamber of the AMO beamline [99].

Radiation damage, on the other hand, has been used for an in-focus *caustic* measurement at FLASH [125] and at LCLS. Here a solid sample is inserted into the focus area to obtain single-shot imprints of the FEL beam at various z positions. With simultaneous intensity measurements by the GMD and the spot-size determined ex situ by atomic force microscopy (AFM), the intensity profile can be reconstructed from the observed depth under consideration of Lambert-Beer’s law and the sample-specific threshold fluence for ablation. A scan along the FEL propagation direction yields the Rayleigh length, i.e. the distance from the focal point to the place where the area of the focal diameter is doubled. The size and possible astigmatism of the incident beam is directly seen in single shot imprints [123].

It should be noted that the standard spot size description by means of the FWHM fails, when the incident beam is distorted or non-homogeneous. Wavefront imperfections may occur from mirror surface roughness [126] or the light generation by amplified spontaneous emission itself. At LCLS, Bogan et al. found that, while the structure of each FEL pulse is unique, the average intensity profile deviates consid-

erably from that of the Gaussian beam [85]. For inhomogeneous beams, the crater size will rise non-linearly with the pulse energy [98].

3.2 The CAMP Endstation

The measurements presented in this report have been performed at the AMO beam-line which was equipped with the CAMP endstation. CAMP is a multi-purpose endstation designed and operated by a collaboration headed by the Max Planck Advanced Study Group at CFEL (thus, *CFEL-ASG Multi-Purpose* endstation). This endstation is described in broad detail in reference [127]. This section presents and discusses the main features of CAMP relevant for the measurements described in chapter 4. In the appendix further details about the vacuum system (A.2.2), MCP-detectors (A.2.4) and pnCCD detectors (A.2.5) can be found. Figure 3.21 gives an overview of the dimensions of the CAMP endstation.

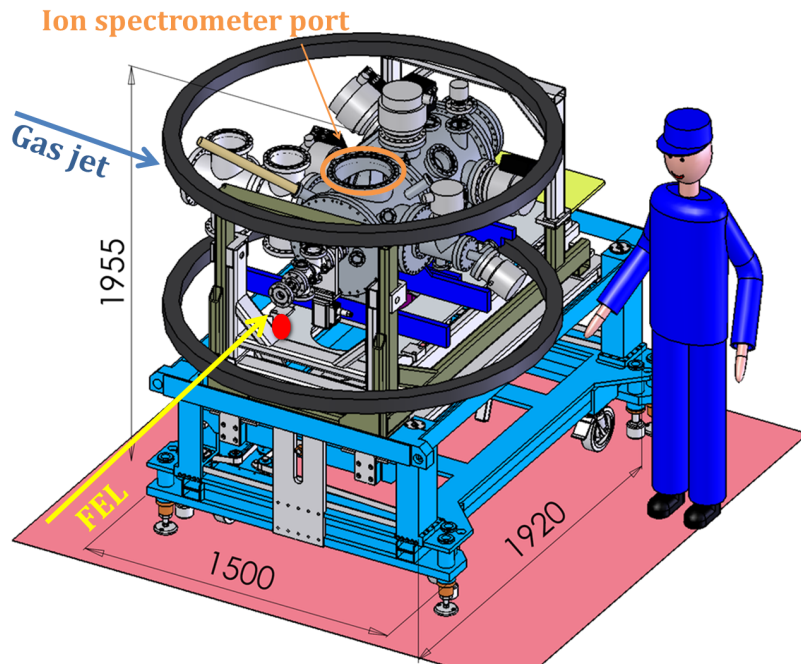


Figure 3.16 – Overview of the CAMP endstation. The FEL entrance is marked by the yellow arrow. The target gas is injected perpendicular to the FEL beam ("gas jet", blue arrow). Ion spectrometers are mounted perpendicular to FEL beam and gas jet via a CF250 port, indicated in orange. The chamber assembly can be remotely adjusted via translational motions of the inner support (greenish brown) along each of the three spatial directions and tilt motions along the vertical and horizontal angles around the pivotal point (marked with the red dot). The base support (blue) remains fixed [127].

3.2.1 Gas Jet

During the course of various beamtimes in the CAMP-chamber conducted by collaborations from different fields of science, a variety of samples and sample-delivery systems have been employed, such as gas jets for atomic rare gases and rare gas cluster, a liquid jet for hydrated bio-samples, an aerosol jet for nano particles, molecular beams and also solid samples.

In this work a gas jet was used to provide a continuous wave (CW) beam of atomic rare gases (2011 data) as the target for the photons. In 2009 the beam was pulsed (10 Hz) by a commercial valve³ to reduce the gas load, when the jet was tuned for rare gas cluster. Also, a low-flow metering valve (leak valve) allowed to flood the chamber to increase the target density.

The jet design is optimized for high resolution momentum spectroscopy. The average energy of an atom at room temperature ($T = 300$ K) and with three degrees of freedom is, according to the equipartition theorem, $E = 3/2 \cdot k_B \cdot T = 39$ meV, which sets an upper limit of the momentum resolution. To cool the target gas it is expanded to supersonic speed. In addition, the target volume is reduced to improve the momentum resolution (Approaches to estimate target density and temperature are described in the appendix A.2.3).

In the current set-up, the *supersonic jet* passes four chambers at different vacuum conditions: expansion chamber, skimmer chamber, experimental chamber and dump chamber, see figure 3.17. Here, the dump chamber was equipped with a residual gas analyzer. Then, the alignment of the gas jet through the various skimmers and apertures can be checked with higher sensitivity.

The target gas is forced through an aperture of $30 \mu\text{m}$ diameter by a pressure up to 10 bar. To avoid obstruction the gas is cleaned by a Swagelok ceramic particulate filter with $2 \mu\text{m}$ pore-size where the gas-line enters the jet. If the pressure before the aperture is at least twice as high as after the aperture the gas will expand adiabatically and faster than the speed of sound [128]. For an ideal gas its enthalpy, the sum of internal energy and the product of pressure and volume, will be converted into kinetic energy, leaving a fast and cold beam.

$$H = U + pV = \frac{3}{2}Nk_B T + Nk_B T = \frac{5}{2}Nk_B T = \frac{1}{2}m\bar{v}^2 = E_{kin} \quad (3.9)$$

³<http://www.parker.com/literature/Literature%20Files/Precision%20Fluidics%20Division/UpdatedFiles/PulseValves.pdf>

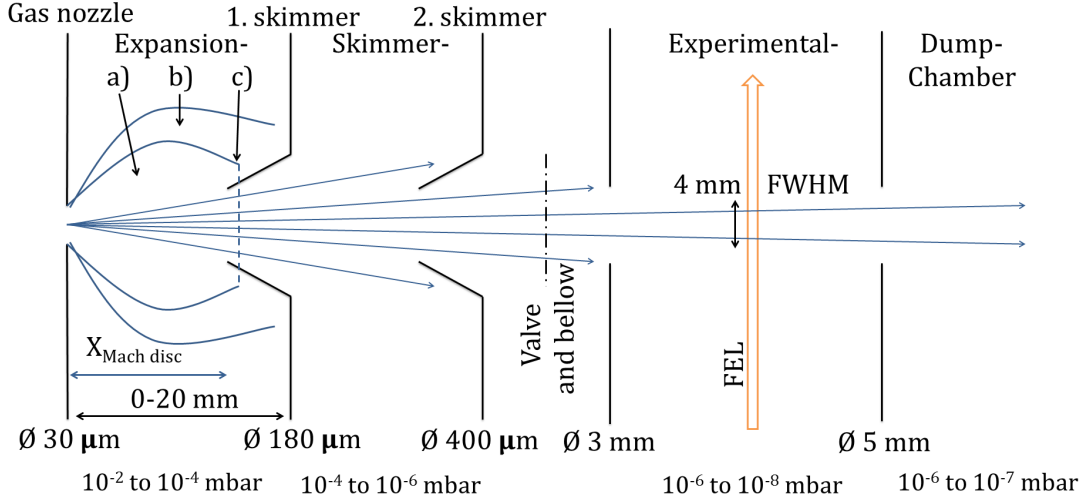


Figure 3.17 – Setup of the supersonic gas jet (not in scale). In the expansion chamber a) marks the zone of silence, b) the shock waves and c) the Mach disc. The diameters of apertures and skimmers are indicated below the drawing as well as the typical gas pressures in the chambers.

The velocity of an ideal atomic gas jet after expansion would hence amount to $v_{jet} = \sqrt{5k_B T/m}$, for example for neon ($m = 20$) $v_{jet} = 778$ m/s. The jet velocity influences in the spatial distribution of ionization fragments on the detector (figure 3.18).

Additionally to corrections for non-ideal gases, the interaction with the residual gas within the expansion chamber has to be considered. The supersonic jet sends out shock waves where the residual gas is compressed and perturbs the free expansion. Only in an area bordering the gas-inlet-aperture, the so called zone of silence, the gas can expand freely. The form of the zone of silence is close to a \cos^4 distribution around the jet axis and several millimeters long. The exact length X up to the Mach disc, that is the end of the zone of silence, is given by

$$X_{Mach\ disk} = \frac{2}{3} d_{aperture} \sqrt{\frac{p_{gas}}{p_{expansion}}} \quad (3.10)$$

where d is the diameter of the aperture, p_{gas} the gas pressure and $p_{expansion}$ the pressure in the expansion chamber [129]. To take advantage of the cooled beam the unperturbed inner part has to be cut out before turbulences occur. A skimmer, that is a thin cone with a small opening on top, is positioned at a distance $X_{1st\ skimmer} < X_{Mach\ disk}$. The skimmer opening-diameter was chosen to be $180\ \mu\text{m}$ and the distance $X_{1st\ skimmer}$ could be varied between 0 mm and 20 mm. A second

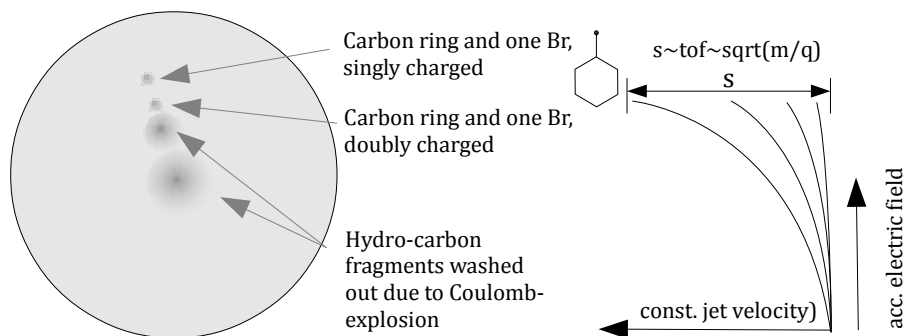


Figure 3.18 – The jet velocity is conserved in the ionization fragments, which experience an additional acceleration by the electric field of a spectrometer (illustrated on the right). As a result, fragments with different time of flights (TOF) also have different detector-hit positions (illustrated on the left for a dibromobenzene-target, a carbon ring with bromine atoms on two opposing sides, recorded on a spatially resolving detector).

skimmer with a diameter of $400 \mu\text{m}$ was installed 18 mm downstream to further skim the atomic beam and reduce the gas load in the main experimental chamber. The diameter of the atomic beam in the interaction zone is about $d_{\text{target}} = 4 \text{ mm}$ (FWHM). The shape, however, was recorded not to be fully Gaussian but to have pronounced tails [130].

Additional differential pumping sections and apertures can be implemented to achieve even more confined and dilute targets. Here, an additional differential pumping section was needed to implement a valve to separate the vacuum of jet and experimental chamber and a bellow for alignment of the jet chambers. (see figure 3.17)

3.2.2 Momentum Imaging Charged-Particle Spectrometers

When the target gas is ionized, ions and electrons have to be guided by a spectrometer to the detectors, so that the momenta and kinetic energies can be retrieved from the time and position of the detector-hit. The spectrometer axis is defined by the extraction direction. Two kinds of ion spectrometers have been used in the CAMP endstation to acquire the data discussed in this work: a reaction microscope (REMI) and a velocity map imaging (VMI) spectrometer. The main difference is, that a VMI cannot measure all fragments in coincidence to retrieve the molecular

frame. Moreover, as the imaging of electrons is concerned, extraction using just an electric field (combined electric and magnetic in a REMI) yields very short time-of-flight prohibiting sufficient momentum resolution along the spectrometer axis. Thus, symmetry conditions have to be fulfilled to calculate the 3D momenta from the detector images.

3.2.2.1 Reaction Microscope

The development of high-resolution momentum spectrometers started with the investigation of collisions of heavy ions with rare gas targets, where the momentum of the recoiling target ion instead of the slightly scattered projectile was measured. In this recoil-ion momentum spectroscopy [131] the high-resolved recoil traverse momentum could not only be attributed to the small momentum transfer from the heavy-ion projectile, but also to the ejected electrons. The momentum resolution was, however, limited by the thermal motion of the target gas. To resolve the tiny momentum transfer from the electron onto the recoil ion, the target gas had to be cooled. The implementation of a cool supersonic jet, described above, led to the *cold target recoil ion momentum spectroscopy* (COLTRIMS) with a high-resolution 4π -detection of the recoil-ion.

Simultaneous recoil-ion and electron momentum detection was the final step to reaction-microscopes (see various review articles [132–134]). Here, the electrons are taken to trigger the ion detection and, thus, enable coincident measurements.

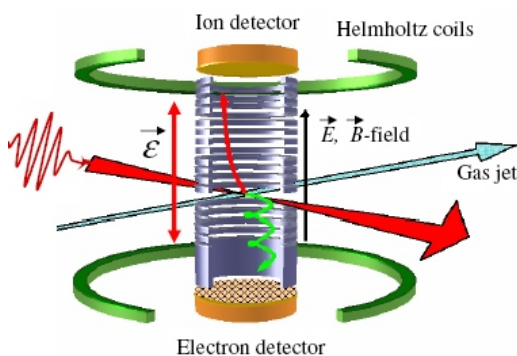


Figure 3.19 – REMI sketch¹

The electron trajectory is confined by the magnetic field of a pair of solenoids that is parallel to the detector-axis (Helmholtz-coils). With both, magnetic and electric fields, the electrons are forced on spiral trajectories which lead to a time and position sensitive detector opposite to the ion detector. While the ions are hardly influenced by the magnetic field and the 4π -detection of the recoil-ion is still valid, electrons are simultaneously detected with close to full solid

¹Source: O. Herrwerth et al., *New Journal of Physics* 10, 025007 (2008). Copyright by the Institute of Physics

angle. Thus, kinematically complete experiments are possible, where the vector-momenta of all reaction-products are retrieved. The downturn of such a coincidence experiment is the limited single-hit rate. All detector signals from the impinging fragments have to be disentangled and attributed to the individual ionization process, which becomes impossible for high count rates. Usually that is compensated for by high repetition rates of the pulsed incoming beam (up to MHz for ion and electron beams, several kilohertz for optical lasers). In the case of present FEL sources, operated up to 120 Hz, this is a serious limitation.

The actual ASG reaction microscope as used in the CAMP endstation is depicted in figure 3.20. It consist of 30 flat and 16 conical electrodes with an inner diameter of 84 mm and an outer diameter of 130. The electrodes are evenly spaced (8.2 mm distance at inner diameter) to build up a homogeneous electric field of few volts per centimeter. The electrodes are isolated by ceramic-discs and connected in series via 100 k Ω resistors to distribute the voltage. All electrodes are made of aluminum and are gold-plated to avoid voltage-inhomogeneities due to non-conducting aluminum oxide. The opening angle of the conical electrodes are chosen such to provide an unrestricted line of sight from the scattering volume in the interaction center to the pnCCD detectors (blue vertical lines on the very right in figure 3.20). Thus, the total pnCCD solid angle is covered, while the conical electrodes also suppress scattered stray radiation emerging from outside the interaction center. The circular shape of the electrodes is cut on one side to allow a minimum distance of 59 mm between the pnCCDs and the interaction center. Both ion spectrometers, REMI and VMI, are orientated perpendicular to the FEL axis and perpendicular to the target jet.

3.2.2.2 Velocity Map Imaging Spectrometer

If more fragments per FEL shot are expected than the reaction microscope can disentangle in a coincidence measurement (several tenth of charged particles), a velocity map imaging spectrometer is preferable. It extracts the fragment with up to several kilovolts per centimeter in a small acceleration region ahead of a field-free drift region of about twice the length (McLaren criterium [105]). Due to the strong electric fields, electrons can be detected without an additional magnetic field. The covered solid angle depends on the actual voltage setting and electron kinetic energies; for the ASG VMI electrons up to 150 eV can be detected over the full

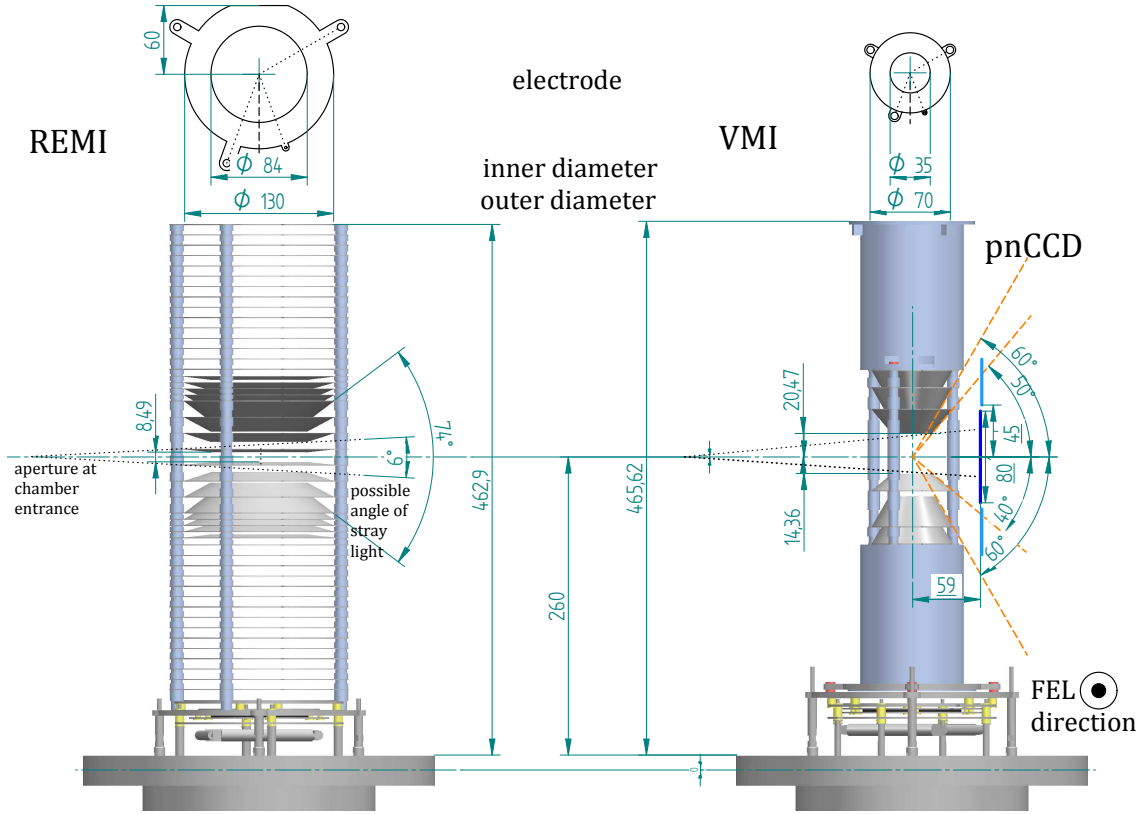


Figure 3.20 – Sketches of the ASG reaction microscope and VMI spectrometer. The linear dimension of the depicted lengths is millimeter. On the very right the pnCCDs are drawn in closed (dark blue) and fully opened position (light blue). The taper of the VMI electrodes is chosen such, that the pnCCDs have a unrestricted line of sight onto the interaction center (orange lines).

solid angle of 4π with a maximum of 10 kV acceleration voltage at the end of the acceleration region.

To account for the high rates (several hundred or even thousands of charged particles per shot), the spatial resolving detector combined with a VMI is usually a MCP-phosphor screen assembly.

On ion or electron impact, the MCP emits an electron cloud at the impact position (see appendix A.2.4), which excites the attached phosphor screen. The radiation of the de-exciting phosphor screen is read out by a CCD camera.

The VMI offers two modes of operation, which are demonstrated in figure 3.21 within an ion trajectory simulation [135]:

On the one hand the spatial imaging mode, where the interaction zone is imaged without focusing electro-static lenses. In figure 3.21 on the left, for example, the

800 nm Ti:sapphire laser ionizes the residual gas along its passage through the spectrometer center and also the krypton in the target gas jet, which is slightly offset in the detector image due to its initial momentum. In the spatial imaging mode the time-of-flight is well resolved.

On the other hand, there is the focussing mode, where a non-homogeneous extraction field focuses fragments of different origin but the same initial velocity vector by means of open electro-static lenses onto the same point on the detector; the time-of-flight resolution, however, is worse than for the spatial imaging mode (on the right in figure 3.21). The focusing mode is used to retrieve the full 3D momentum vector of the fragments via Abel transformation from the measured 2D distribution for symmetric fragment emission. In a REMI and a low-rate VMI with fast spatial-resolving detectors (delay line anodes, see section 3.2.2.3) [136], the molecular frame can be traced back by the 3D coincidence-measurement, where spatial and temporal information of the detector-hit is available. In a standard VMI, the nanosecond-precise time information is lost owing to the high extraction field and the millisecond-long integrating time of phosphor screen and CCD. Then, a coincidence measurement is not possible and the molecular frame cannot directly be retrieved. Instead of an arbitrarily oriented e.g. molecular ensemble, axial alignment has to be applied with an axis of cylindrical symmetry parallel to the surface of the detector. Then, the 3D information can be calculated from the 2D picture via a mathematical inversion procedure [137, 138]. Velocity map imaging has been employed at the FLASH soft X-ray laser and demonstrated that high-resolution momentum distributions can be retrieved at high rate from non-linear FEL ionization processes [139].

The six electrodes of the ASG VMI have smaller inner (35 mm) and outer (70 mm) diameters than the REMI electrodes to provide a higher electric field in the center (figure 3.20). The first generation of VMI spectrometers consisted of a closed repeller, an open extractor and a grounded drift electrode [140]. Later an open repeller was chosen to detect either electrons [136] or ions [141] on a second detector as a trigger for the ion time of flight or electron angular distribution, respectively. Here, the VMI is *double-sided and symmetric* (apart from the first electrode). It has a drift tube on both sides and the extractor electrode of one side works as repeller electrode for the other side. The symmetric design allows the simultaneous measurement of the ion and electron momenta. For instance, the electron diffraction patterns of photo electrons in a laser aligned molecule could recently be measured

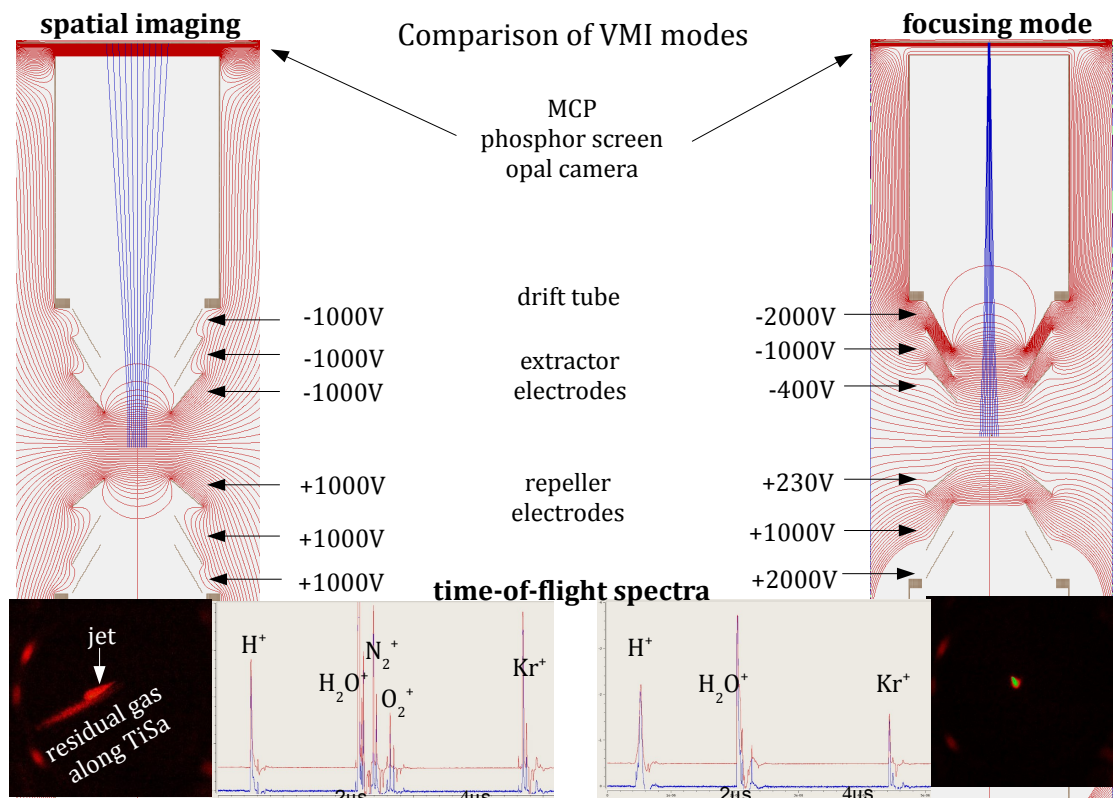


Figure 3.21 – Two modes to run a VMI spectrometer: spatial imaging and focusing. The detector image (spatial information) and the time-of-flight spectrum is shown for both modes. Analogue to standard one-side VMIs the electrodes are labeled as repeller, extractor and drift tube.

on one side while the other side imaged the ion distribution to monitor the degree of molecular alignment. The voltage on each electrode is set independently to adjust the focusing for the expected electron kinetic energy or to change between focusing and spatial imaging mode. The electric field of the spectrometer is defined at the end of the drift tubes by a fine copper mesh with 80% transmission on fixed voltage. An additional unique feature of the ASG VMI are the conical electrodes. With the pnCCDs downstream of the interaction zone (blue vertical lines on the very right in figure 3.20), simultaneous measurements of ion time-of-flight spectra and diffraction patterns or the fluorescent yields can be performed.

3.2.2.3 Time and Spatial Resolved Ion Detection

The ion signal is amplified by a set of multi-channel plates (MCPs, see appendix A.2.4) by a factor of about 10^7 . While the MCP amplifies the signal of the charged

particle and provides the time coordinate, an additional anode is required to retrieve the spatial information of a detector hit. Delay line anodes provide high position resolution over a large area and fast read-out allowing high count-rates [142].

The basic idea is to derive the signal start position on a transmission line of fixed length from the times the signal needs to propagate to both ends of this line. The transmission line, however, is not straight but has a meander-shape causing a time delay; delayed, that is longer, times are detected with higher accuracy resulting in higher position resolution. By its meander-shape the transmission line covers an area and thereby yields a one dimensional coordinate for all signals starting in this area. To get a two dimensional position read-out a second delay line is added perpendicular to the first one.

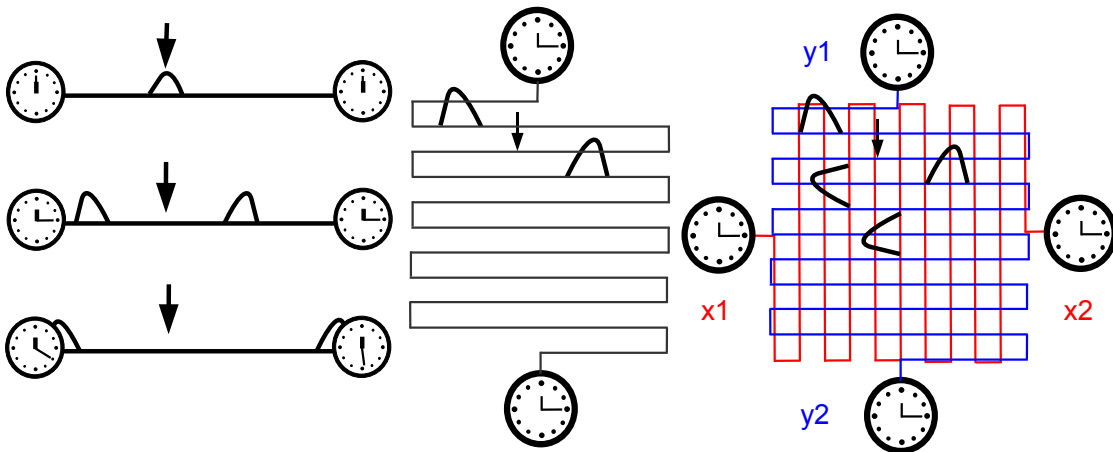


Figure 3.22 – The working principle of the delay line anode: the position is derived from signal propagation times (left), meander-shape delay line (middle), two dimensional delay line anode (right).

Although the delay lines form a discrete anode pattern the position read-out is continuous. This is achieved by interpolating the center-of-mass of the charge cloud which spreads out starting from the impact position of the particle on the MCP and which is collected by several wires.

Additionally to the signal transmission line, there is a second so called reference line on lower voltage relative to the signal line (36 V). The reference line serves as reference to electronic noise which is found on both lines. Moreover, these two parallel lines form a Lecher line decreasing the impedance for the high-frequency signals when it runs to the readout.

A detector assembly with an MCP and quadratic delay line can resolve and disentangle the position and time-of-flight information of up to 30 particles per shot, with a hexagonal anode, with three instead of just two layers, up to 100 particles per shot can be processed [143].

For high rates, a phosphor-screen is used. In an assembly of an MCP and a fiber-optic with phosphorescent coating, the output charge distribution of the MCP is converted into a visible image (wavelength around 545 nm). The spatial resolution of an MCP is limited in principle by the center-to-center pore spacing which is $32 \mu\text{m}$ in the implemented Photonis assembly⁴. With a two-stage MCP, the resolution is about $90 \mu\text{m}$ [144].

3.2.3 Photon Detection

Photon detectors were implemented in the CAMP-chamber to investigate photon diffraction and scattering as well as fluorescent emission. In this work the fluorescence spectrum of xenon is analyzed.

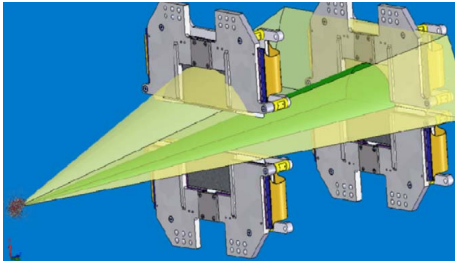


Figure 3.23 – The mounting of two pnCCD-detector pairs in the CAMP endstation; the front pair is moveable in 3D, the back pair is fixed.

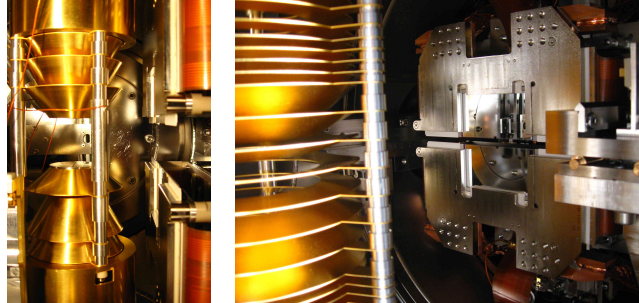


Figure 3.24 – VMI (left) and reaction microscope (right), respectively, mounted in the CAMP endstation with the movable front pnCCDs at closest distance from the interaction point for spectroscopic use.

For CAMP, a large format semiconductor detector was used, a pn-junction charge coupled device (pnCCD) [127, 145]. In summary these pnCCDs are large-area (58 cm^2 ($78 \text{ mm} \times 74 \text{ mm}$), 1024×1024 pixels of $75 \times 75 \mu\text{m}^2$ area each), low signal noise (2.5 electrons (rms)), broadband (100 eV-25 keV), high-dynamic-range,

⁴Model *APD 2PS 75/32/25/8 D 60:1 NR P20* for explanations see <http://www.ilphotonics.com/cdv2/Photonis-PMT-MCP-EM-II-%20ICCD/Detectors/APD.pdf>

single-photon-counting X-ray detectors capable of imaging and spectroscopic applications. A detailed description can be found in the appendix, section A.2.5. For small-angle diffractive imaging experiments, one set of pnCCDs is mounted 500 mm downstream of the interaction point (and can be moved to any longer distance by inserting adaptor tubes). Another set of pnCCDs is moveable along the beam direction over 250 mm and these detectors can be moved vertically (i.e. perpendicular to the beam) by 45 mm for larger scattering angles (see figure 3.23). In the spectroscopic setting the detectors should be as close as possible to cover the highest solid angle. In figure 3.24 the pnCCDs are moved to the closest distance to the interaction point allowed by the ion spectrometer. The resolution at 1500 eV photon energy was found to be 98 eV.

3.3 Data Acquisition and Analysis

3.3.1 From Analogue Pulses to Digitized Data

3.3.1.1 High-Pass Filter

Pulses from the MCP-delay-line detector are decoupled through an RC-filter (resistor-capacitor circuit). The bias-voltage is applied on the resistor side, the high-frequency pulses are read out on the capacitor side (fig. 3.25 and 3.26).

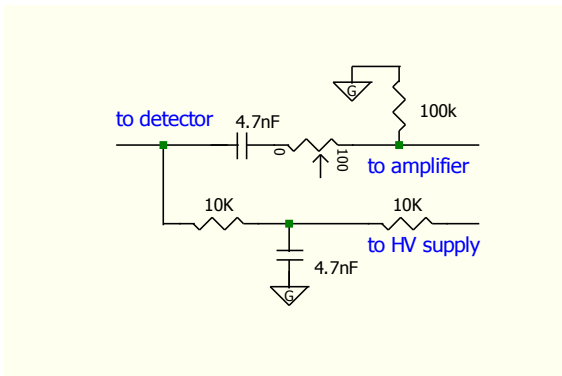


Figure 3.25 – High-pass MCP read-out.

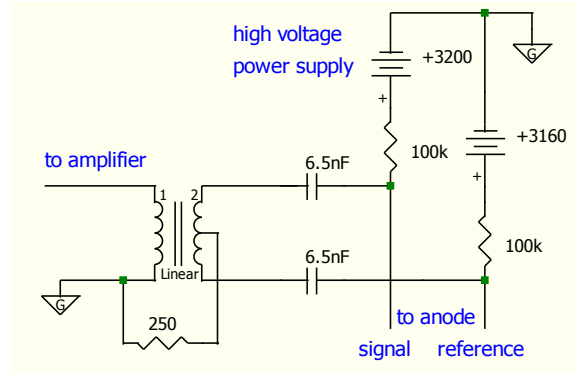


Figure 3.26 – Differential anode read-out.

Signal and reference line are connected to the ends of the secondary coil of a transformer. Electric noise is equally distributed on both lines, such that the voltage on both ends of the coil is the same and the transformer does not deliver this DC-like voltage rise to the primary coil. Due to the slightly higher bias voltage on the signal line, real pulses have a higher amplitude on the signal than on the reference line. Thus, real (AC-like) pulses are transformed to the primary coil.

3.3.1.2 Digital Converter

For the delay line anode, the analogue detector pulses are digitized by an Acqiris ADC [146]. It provides four channels with a sampling rate of 2 GHz. That means, the maximum time resolution of a detector signal is 500 ps, when all four channels are used in parallel, and 125 ps, when only one channel is used. The resolution of the pulse height is 10 bit. The Acqiris Digitizer records the complete wave form of the signal and is, therefore, especially capable for multi-hit detection. Any peak

recognition and filtering is then done on the software site (see sec. 3.3.2.1). The maximum length of the waveform was limited by the LCLS network speed to 20000 data points, such that the waveform was 20 μ s long at a 1 ns resolution.

The phosphor screen image is recorded by commercial CCD cameras. LCLS provided Adimec OPAL-1000 cameras, implemented in their data acquisition system, with megapixel resolution and 120 frames per second acquisition rate [147]. For non-LCLS experiments a Pulnix TM-6740CL camera with an acquisition rate of 200 frames per second, but a lower resolution of 640 times 480 pixel is used with the ASG VMI spectrometer [148].

3.3.1.3 Analysis Software

The LCLC data files (".xct" file format, "extended tagged container") are analyzed with the C++ based CFEL-ASG Software Suite (CASS) [149]. It handles all data from the different detectors used in CAMP: from Acqiris analogue-to-digital-converters (ADC) [146], Acqiris time-to-digital-converters (TDC) [150], commercially available charge coupled devices (CCD) and pnCCD cameras, and also the machine-related data, i.e. fast shot-to-shot beamline data (e.g. pulse or photon energy) and slow 1 Hz "epics"-data [151] (e.g. voltage or pressure settings).

Analysis tasks are listed as postprocessors in a text file (".ini file" format). Postprocessors are user definable procedures to handle and analyze recorded raw data of the experiment. They include data operations as, for instance, putting requested measurements from a data file into a user defined spectrum, computing logical and arithmetic values from the dataset or relating different measurements and computations within one FEL event. The resulting 0D, 1D or 2D histograms can either be saved in hdf5 [152] or in root [153] file format. Here, the root format was chosen so that histograms could be evaluated further in the ROOT C++ framework. Eventually, histograms have been processed by the analysis software originpro [154] because of its superior graphical presentation and ease of use.

3.3.2 Ion Time-of-Flight Spectra

In a time-of-flight (TOF) spectrometer, the time between the creation of the ion and its detection is proportional to its charge-to-mass-ratio. While the recorded Acqiris trace already comprises the main features of a time-of-flight spectrum, particular

peak heights and positions have to be addressed in a more quantitative analysis.

3.3.2.1 Constant Fraction Discriminator

The Acqiris trace depicts the voltage history on the MCP detectors within an adjustable time window and temporal resolution, here $20 \mu\text{s}$ and 1 ns , respectively. In a so called counting mode, where the ion rate is intentionally set low to reduce the overlap of signals in the Acqiris trace, the actual pulse shape and amplitude can be disregarded. The only important information is the (temporal) peak position. For further analysis, it is practical to discretize each peak position. The simplest method to find peak positions and suppress noise peaks, is to set a threshold. This approach, however, yields different times for different peak heights as seen in figure 3.27 on the left. The determination of the center of mass addresses this issue but fails when neighboring peaks superpose.

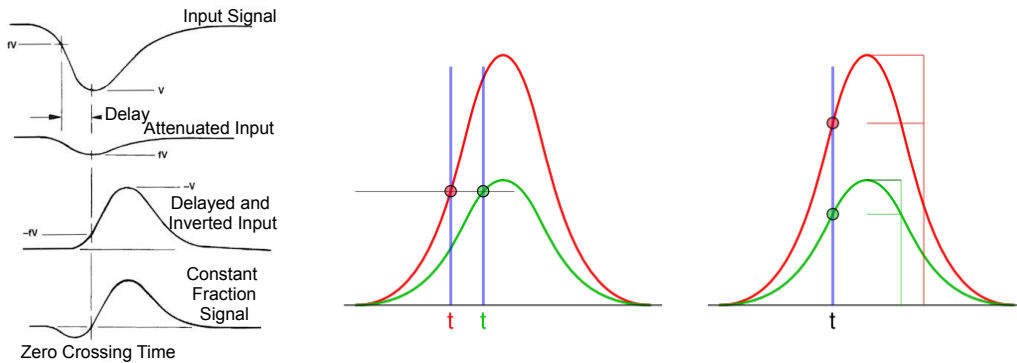


Figure 3.27 – The CFD creates a zero-crossing by adding a delayed and inverted pulse to a fraction of the original input. This way, the triggering time becomes independent of the pulse amplitude (right), in contrast to triggering by a threshold (left).

The constant fraction discriminator (CFD), depicted in fig. 3.27, is able to discriminate peaks even when they (slightly) superpose. The CFD algorithm delays the incoming pulse by few nanoseconds and subtracts it from a fraction, typically 60%, of the undelayed pulse:

$$f_{CFD}(x) = f(x) \cdot \text{fraction} - f(x + \text{delay}) \quad (3.11)$$

3.3.2.2 Calibration of a Time-of-Flight Spectrum

The utilized time-of-flight spectrometer has, except at edges and lenses, a homogeneous electrostatic field, where the kinetic energy induced on a particle with mass

m and charge q by the accelerating voltage U is $E_{el} = q \cdot U$, thus

$$E_{el} = q \cdot U = \frac{1}{2}mv^2 = E_{kin} \Rightarrow v = \sqrt{\frac{2qU}{m}} \Rightarrow t = s \cdot \sqrt{\frac{m}{2qU}} \quad (3.12)$$

So at fixed spectrometer voltages, the ion time-of-flight t is specific for a certain m/q value (and specific for the ion momentum along the spectrometer axis). With the linear equation

$$\sqrt{\frac{m}{q}} = a \cdot \text{time of flight} + b \quad (3.13)$$

peaks in a time-of-flight spectrum can be attributed to meaningful values of m and q . Typical ions from residual gas, which can be found in most TOF spectra, are hydrogen, $\sqrt{\frac{m}{q}} = 1$, and oxygen singly or doubly charged, $\sqrt{\frac{m}{q}} = 4$ or $\sqrt{\frac{m}{q}} = 2.8$, respectively. When the peaks of these ions are clearly distinguishable in the TOF, their time-of-flight and $\sqrt{\frac{m}{q}}$ value serve as calibration points for the whole TOF spectrum.

In the case of the xenon and krypton, irradiated by ultra-intense x-rays, oxygen peaks were superimposed by target gas ions and the recorded 20 μs Acqiris trace missed the lowest xenon and krypton charge states, so that simple enumeration along $1+, 2+, 3+, \dots$ was not possible. Then, the calibration has to be found by the determination of the lowest recorded charge state q . The higher charge states can then be enumerated starting from that q .

In figure 3.28 every time-of-flight peak is attributed to $\sqrt{\frac{m}{q}}$ values, assuming that the lowest recorded charge state at 17.2 μs is either Xe^{1+} (green), Xe^{3+} (blue) or Xe^{5+} (red). It turns out that only the blue curve follows the linear equation (3.13), so the peak at 17.2 μs must belong to Xe^{3+} . With the lowest recorded charge state attributed to Xe^{3+} the subsequent higher charge states are attributed to $q+n$. This way, the time-of-flight spectrum is calibrated.

3.3.2.3 Deconvolution of Merged Charge States

To determine the precise abundance of each charge state, every peak should be integrated within TOF adjusted limits. However, for short time-of-flights, due to high extraction fields or for highly charges ions, and in the presence of many isotopes, densely spaced peaks may superpose in the averaged spectrum and also in single shot spectra; for example with 50 V extraction voltage $^{126}\text{Xe}^{15+}$ starts to overlap with the heavier isotope $^{136}\text{Xe}^{16+}$, and, at even shorter time of flights, consecutive charge states increasingly merge.

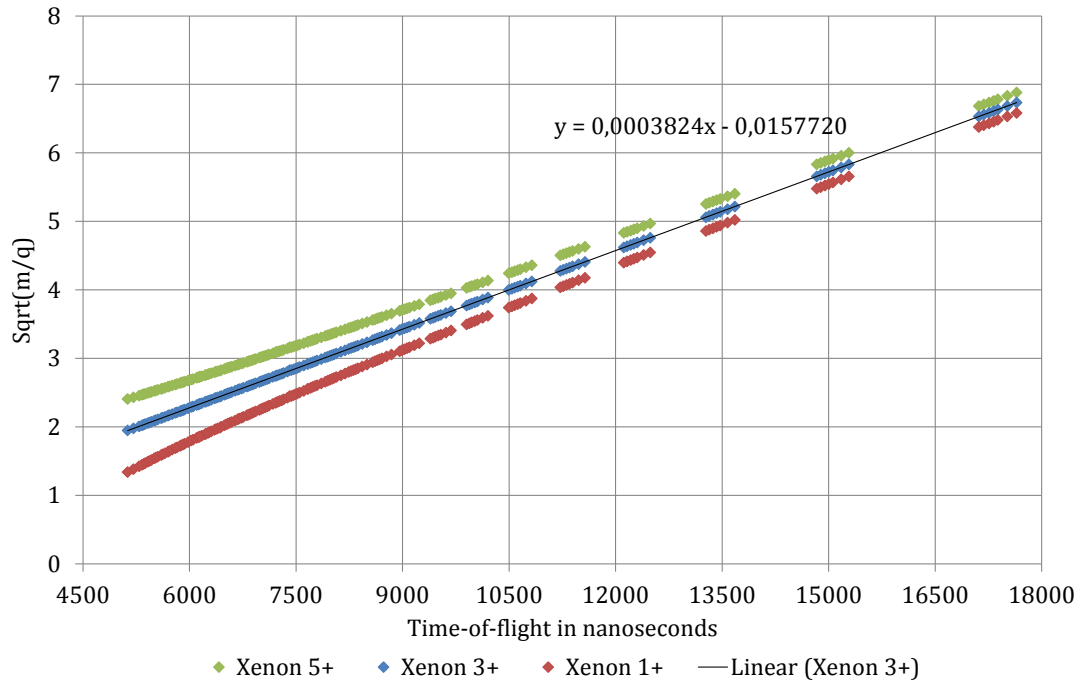


Figure 3.28 – Xenon time-of-flight calibration at 50 V spectrometer voltage: the $\sqrt{\frac{m}{q}}$ ratios are plotted against the TOF. The green, blue and red line assume that the charge state with the longest time-of-flight is Xe^{5+} , Xe^{3+} and Xe^{1+} , respectively. The $\sqrt{\frac{m}{q}}$ values linearly depend on the TOF and as only Xe^{3+} is described by a linear function, charge state with the longest time-of-flight must be Xe^{3+} .

To deconvolve the (averaged) spectrum, the height of each individual charge state is adjusted in a simulated charge-state distribution, until the sum of all simulated Gaussian-shaped peaks matches the experimental data. Three parameters have to be determined experimentally: the isotopic composition of the target gas as well as time-of-flight dependent peak positions and peak widths. For lower charge states of xenon, the isotopic composition is resolved. The integral of a Gaussian fit for each mass yields an isotopic ratio:

Xenon mass in [u]	128	129	130	131	132	134	136
Measured percentage	2.26	25.13	4.59	20.76	25.79	11.58	9.89
Literature value	1.91	26.40	4.10	21.29	26.90	10.40	8.90

Table 3.3 – Isotopic composition of xenon

From the equation 3.13 of the calibration, the individual peak position for merged ion signals is derived. The peak width was found to decrease linearly starting from

Xe^{11+} and, thus, could be interpolated to higher charge states.

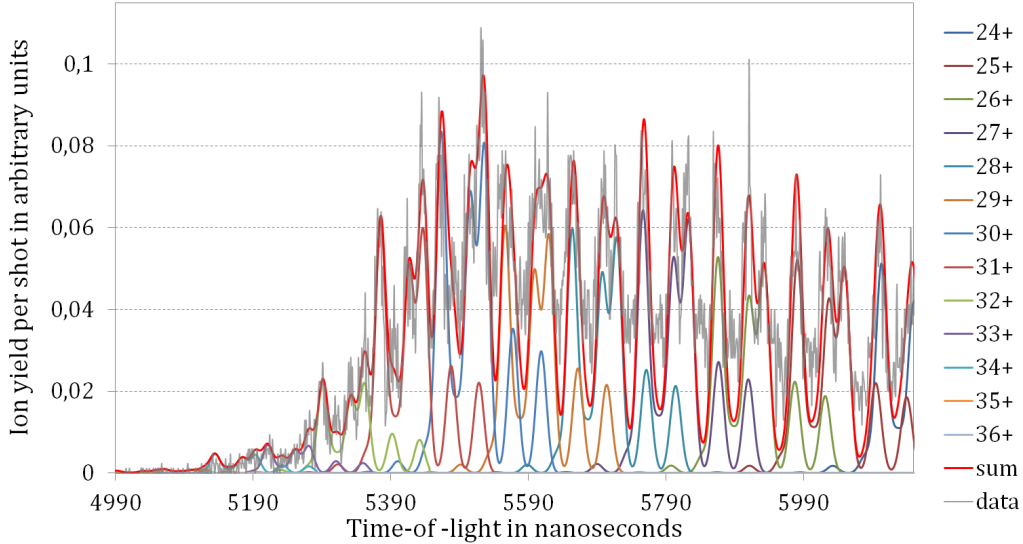


Figure 3.29 – Deconvolution of merged xenon time-of-flight peaks at 1500 eV photon energy, 80 fs pulse length and 2.5 mJ pulse energy. The height of the individual charge state peaks (colored) are adjusted so that their sum (red) matches the data (grey).

The deconvolution is manually performed for the experimental spectrum at 2.5 mJ pulse energy (fig. 3.29). For a scan over different parameters, in particular different pulse energies, manual adjustment becomes impractical. Instead, one peak per charge state (i.e. ^{132}Xe instead of all isotopes) is integrated within time-of-flight adjusted limits and merged peaks are weighted according to the overlap with neighboring peaks within the limits of integration. For example, the percental contribution in the limits of integration for Xe^{30+} is: 1.5% Xe^{29+} , 78.5% Xe^{30+} and 20% Xe^{31+} . These weight factors should be used with care, as they are determined at a certain pulse energy (2.5 mJ), whereas the charge-state distribution and, thus, the percental contribution will change non linearly at different pulse energies. As this approach was limited to a small pulse energy region and few highly charged ions, the effect of changing percental contribution has been neglected.

3.3.3 Analysis of the Fluorescence Spectra

The analysis of spectroscopic pnCCD data requires several calibration steps and a careful choice of readout-parameters. To understand the necessity of these steps, the measurement process should shortly be summarized (according to reference [155],

modified and extended):

Absorption of impinging X-ray Photons The photon energy of a photon impinging on the pnCCD detector is converted to electron-hole pairs via the photo-effect, a fraction also into phonons. At X-ray energies 3.6 to 3.7 eV are required for the creation of one electron-hole pair in silicon. Because the electron emission processes are not independent, a statistical uncertainty of this conversion factor, the Fano-noise, has to be considered. Fano-noise describes that it may require less or more energy to create electron-hole pairs. For silicon the Fano-factor, the measure of the Fano-noise, is 0.115. The Fano noise is energy dependent, roughly $\propto \sqrt{\text{Fano-factor} \cdot \text{constant} \cdot \text{Energy}}$.

Charge Drift, Diffusion and Distribution over several Pixels As electrons drift towards the potential minimum $7 \mu\text{m}$ under the pnCCD readout site (see fig. A.6 in the appendix), the electron cloud widens up due to Coulomb repulsion and diffusion. This Gaussian shaped cloud may extend over one to four neighboring pixels, so that the total charge may be split in fragments. Charges can be created thermally or by hot spots in the crystal which is why the pnCCD is cooled down to -50°C and less.

Transfer of Charges to Readout Anode In each readout line, electrons might be trapped at crystal defects during the transfer from the pixel-potential well to the anode. They can either catch up with the charge train or be delayed into the charge package of a succeeding pixel which smears out the spatial distribution. Charge-transfer efficiency (CTE) is a statistical process and adds noise.

Frontend Electronics The combination of a low capacitance anode and on-chip JFET amplifier provides an excellent signal-to-noise ratio. However, electronic noise might be added by non-linearities from the output driver of the CAMEX-chips or the limited bandwidth of the transmission line to the ADCs which themselves might add a small digitization noise.

That means for each measurement read noise, gains, charge-transfer efficiencies, charge splitting between neighboring pixels, energy resolution, and bad pixels have to be determined individually either line or pixel wise.

3.3.3.1 Correction Maps created from Dark Frames

Line and pixel corrections are saved in distinct maps. To avoid "false positives", corrections maps are taken as dark maps with all light sources shielded. The following

correction maps are used:

- Offset Map: Leakage currents may shift the baseline of each pixel. Also the total readout channel may show an additional offset.
- Noise Map: To derive the statistically leakage currents of each pixel the standard deviation of 200 sampled frames is taken.
- Common-Mode Correction: Cross talk during the parallel electronic readout of all channels is addressed in the common mode correction.
- Bad Pixel Map: Bright and noisy pixels are recognized by the offset and noise correction. In the analysis settings a noise level can be chosen to automatically set pixels as bad-pixel, so that these pixels will be disregarded in the further analysis. Additional bad pixels can be set by the user.

In CASS, common mode, noise and bad pixel correction are individually switched on and off and read in via the dark calibration file.

3.3.3.2 Clustering of Pixels and Pixel Threshold

In photo frames, the offset map is subtracted, the common-mode correction performed and the noise threshold applied. Additional to the pixel coordinates and pulse heights, the frame index and quality value are recorded, which indicates if an event is in the vicinity of a bad pixel, a border or has an over- or underflow. Charges distributed over neighboring pixels are combined to one event (clustering). At maximum four pixels can be combined, if the resulting pattern is allowed [155] (e.g. three pixels in a row are forbidden). Charge-transfer efficiency (CTE) and gain calibration are loaded from a gain map [156].

3.3.4 Machine Data

Machine data includes fast changing shot-to-shot beamline data (e.g. pulse or photon energy) and slow changing 1 Hz "epics"-data [151] (e.g. voltage or pressure settings). Here, ion yield curves could be correlated to the pulse energy and the linearity of pulse energy to attenuation pressure was shown.

Chapter 4

Multiple Ionization of Heavy Atoms by Intense X-Ray FEL Pulses

4.1 Experimental Parameters

The data presented in this work were taken during two beamtimes at the LCLS XFEL using the CAMP endstation at the AMO beamline. The experimental parameters are summarized in table 4.1.

Beamtime	December 2009	January 2011	
Focus	$\approx 3 \times 3 \mu\text{m}^2$	$\approx 3 \times 3 \mu\text{m}^2$	
Rayleigh length	10-20 mm	5-10 mm	
Gas jet diameter	2 mm or flooded	4 mm	
Ion detector-acceptance	1 mm, VMI with slit	80 mm, open REMI	
Fluorescence detector-acceptance	38.4 mm x 76.8 mm, 67 mm downstream	none	
Target	Xe	Xe	Kr
Pulse length	300 fs	80 fs	80, 3 fs
Photon energy	1.5 keV	1.5, 2 keV	2 keV
Pulse energy	2.5 mJ	2.5 mJ	2.5, 0.4 mJ
Attenuator transmission	12%, 37%, 100%	0.01-100%, 5 steps	

Table 4.1 – Experimental parameters during the beamtimes in 2009 and 2011.

In the beamtime 2009 an aluminum-disk with a 1 mm wide, 20 mm long slit

orientated perpendicular to the FEL direction was inserted into the first electrode of the VMI spectrometer to confine the detector acceptance to the high-intensity part of the interaction center.

The pair of front pnCCDs were positioned 67 mm downstream of the interaction center. One of the pnCCDs could not be used due to problems with the readout electronics. About one third of the analyzed detector area was masked (set as bad-pixel) to disregard pixels with too much stray light and broken pixels after direct exposure to the focused beam [157]. Then, the analyzed detector area covered a solid angle of 0.37 sr or 39.3° opening angle, respectively.

With the thin gas jet only, meaningful fluorescence spectra at several pulse energies and for various gas targets could not be recorded within the available beamtime. Besides, at a base pressure of few 10^{-7} mbar, relatively small time-of-flight signals of xenon were superimposed with signals from residual gas. Thus, to increase the fluorescence yield the experimental chamber was flooded with xenon to a gas pressure of $1 \cdot 10^{-6}$ mbar. The LCLS gas attenuator was set to three different transmissions to scan the focus intensity.

In 2011, the ion time-of-flight spectrum of xenon was remeasured under improved vacuum conditions (10^{-8} mbar) where contributions from residual gas were negligible in time-of-flight spectra taken with the gas jet only. The intensity was varied in five steps from 0.01-100%. In addition to photon energies of 1.5 keV (corresponding to 0.6 nm wavelength), xenon time-of-flight spectra were measured at 2 keV (corresponding to 0.83 nm wavelength). For krypton at 2 keV data for two pulse lengths were compared, namely 80 fs and < 10 fs, which will hereafter be referred to as 3 fs (3 fs is an estimate, which was used in the calculations. For a discussion of the pulse length determination see section 3.1.3.2).

Here, the REMI, instead of the VMI spectrometer, was used. The total acceleration voltage was much lower as compared to the VMI settings in 2009, 50 V instead of 2 kV, allowing for a much better time-of-flight resolution. With the 80 mm electrode opening, the spectrometer was also sensitive to ions created out of focus at lower intensities.

The pulse energy in table 4.1 is given by the LCLS GMD in front of the steering and focusing optics of the AMO beamline. For calculations of the actual photoionization the fluence at the interaction point has to be estimated considering the AMO beamline transmission and focus size. The experimental beamline

transmission was reported to be about 20% while the design value is about 60% [19]. In reference [19] a focus size of $3 \mu\text{m}^2$ is assumed for the HFP chamber about 2 m further upstream of the CAMP endstation. The focus size in CAMP is larger due to the larger distance to the KB focusing optics. The smallest measured focus in CAMP so far is about $12 \mu\text{m}^2$ [158]. Imprint measurements [98] (see section 3.1.4.1) in the CAMP endstation determined an effective focal area of about $45 \mu\text{m}^2$ in 2009 and about $37 \mu\text{m}^2$ in 2011. However, both measurements were performed at a later time possibly not reflecting the focal parameters of the actual experiment any more. Besides, with these focal sizes, calculations do not at all reproduce the experimental charge-state distributions suggesting, that the imprint studies overestimate the focus size.

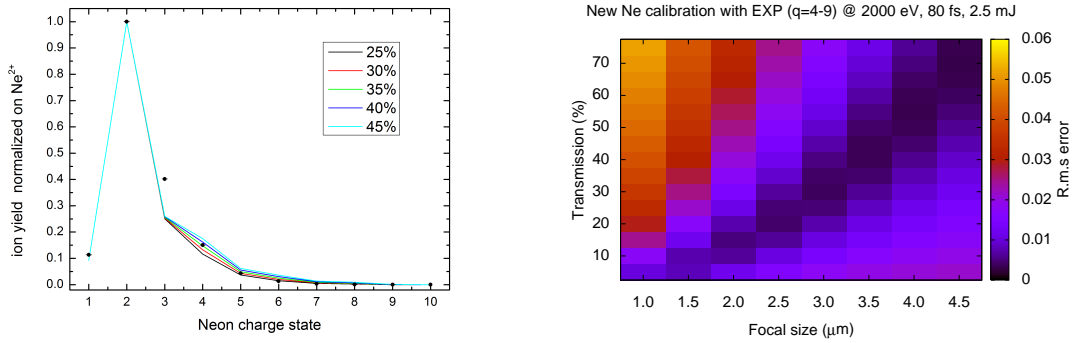


Figure 4.1 – Determination of beamline transmission by the use of the neon charge-state distribution at 2 keV photon energy, 80 fs pulse length, 2.5 mJ pulse energy. On the left the experimental data (black dots) along with calculations for a $3 \mu\text{m} \times 3 \mu\text{m}$ FWHM Gaussian-shaped focus size, 4 mm FWHM gas-jet diameter, 80 mm detector acceptance and several transmissions indicated in the figure are plotted. On the right the quadratic deviation between data and theory at different sets of focus diameters and transmissions is shown.

To determine the transmission and focus size during the actual experiment, the experimental charge-state distribution for a Ne target was compared to theoretical calculations that had consistently explained previous measured data [19]. For this purpose, the experimental charge-state distribution of neon at 2 keV photon energy was taken immediately before the xenon measurement. The deviation between experiment and calculation was determined for neon charge states from Ne^{4+} to Ne^{9+} neglecting charge states up to Ne^{3+} which might be created by one photon ioniza-

tion far out of focus. The quadratic mean of these deviations is depicted in figure 4.1 on the right for various transmissions and focus sizes. The darkest color marks the lowest deviation. From the dark-purple diagonal a combination of transmission and focus size was chosen, which fits within the range of previously reported values: $3\ \mu\text{m} \times 3\ \mu\text{m}$ FWHM Gaussian-shaped focus size and 35% transmission at 2 keV photon energy ($3.5\ \mu\text{m} \times 3.5\ \mu\text{m}$ and 48%, would fit as well).

With these parameters and a nominal pulse energy of 2.5 mJ, the focal intensity was $1.2 \times 10^{17}\ \text{W}/\text{cm}^2$.

At 1.5 keV photon energy a transmission of 18% and $3\ \mu\text{m} \times 3\ \mu\text{m}$ focus size was assumed to fit the calculated intensity-dependent ion yield to the data (see figure 4.11; here 35% transmission and a $4.2\ \mu\text{m} \times 4.2\ \mu\text{m}$ focus size would yield the same fluence). This assumption is based on predictions that the fluence decreases at lower photon energies [126]. With the lower transmission at 1.5 keV, the focal intensity is $6.3 \times 10^{16}\ \text{W}/\text{cm}^2$.

4.2 Ion Spectra: Charge-State Distribution after X-ray FEL Irradiation

4.2.1 Ion Spectra of Xenon

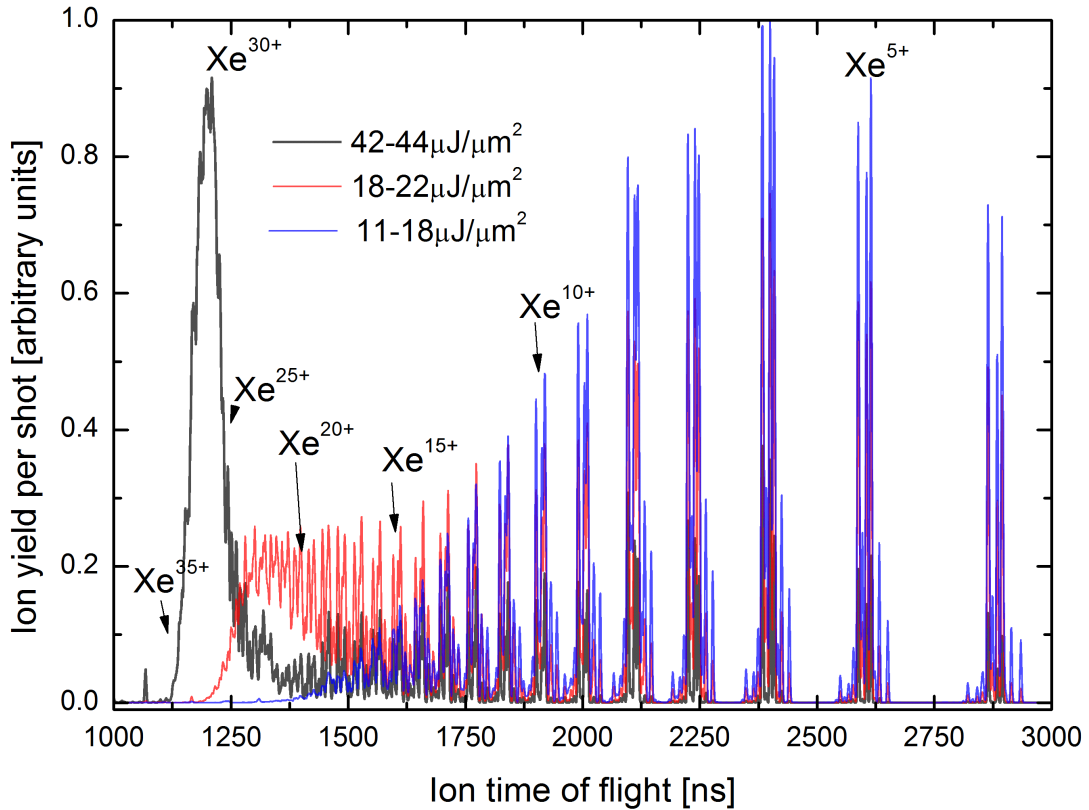


Figure 4.2 – Xenon ion time-of-flight spectra at 1.5 keV photon energy for three fluences (2009 data).

The xenon time-of-flight spectrum in figure 4.2 compares the ion yield at three fluences. At lowest fluence (blue) the largest ion yield is recorded for Xe^{6+} , the highest charge state is Xe^{20+} . Then, at medium fluence (red), lower charge states ($< \text{Xe}^{11+}$), which can be reached by single-photon ionization [110, 113], have a smaller yield, but the ion yield for Xe^{12+} to Xe^{24+} is enhanced and charge states up to Xe^{30+} are observed, with fast decreasing yield, though. For the highest fluence (black) the charge-state distribution changes dramatically. Up to Xe^{25+} the ion yield for all charge states is below 0.3 arbitrary units. Beyond Xe^{25+} the ion yield increases tremendously with Xe^{30+} being more than three times higher than the

lower charge states. Here the highest observed charge state is Xe^{36+} . Note that the height of the peaks in the TOF-spectra for different charge states does not directly relate to their respective yields due to the $\sqrt{q/m}$ compression of the scale towards shorter TOFs.

Due to the high extraction voltages the time-of-flight spectrum is confined on to just $2 \mu\text{s}$, so that the time resolution is rather low and neighboring peaks merge quickly with increasing charge state. For instance, the large peak at Xe^{30+} is partly due to contributions from neighboring peaks and, using the deconvolution procedure its height of 0.9 units is actually found to be 0.6 units. Thus, the time-of-flight spectrum of xenon depicted in 4.2 was measured under improved conditions in 2011, see figure 4.3. Note that also other experimental parameters change slightly, see table 4.1; most notably the detector acceptance was 80 mm in 2011 as compared to 1 mm in 2009. Hence, not only ions experiencing the highest fluence in the interaction center are detected, but also ions created by single-photoionization far out of the focus.

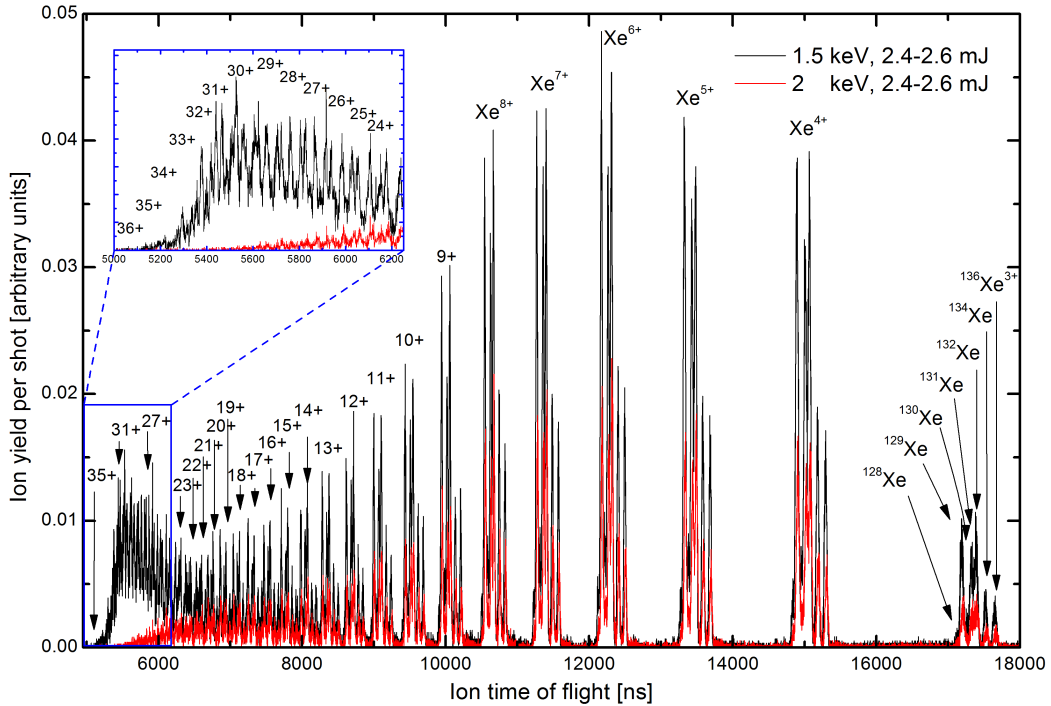


Figure 4.3 – Xenon ion time-of-flight spectrum at 1.5 keV (black) and 2 keV (red) photon energy and 2.4 to 2.6 mJ pulse energy.

In figure 4.3 the xenon time-of-flight spectrum is presented for 1.5 keV (in black)

and 2 keV (in red) photon energy, integrated over a pulse energy interval of 2.4 mJ to 2.6 mJ. This corresponds to a peak fluence of approximately $42\text{-}46 \mu\text{J}/\mu\text{m}^2$ (1.5 keV) and $82\text{-}89 \mu\text{J}/\mu\text{m}^2$ (2 keV) at the target.

For lower charge states, i.e. long time-of-flights, the REMI spectrometer features isotope separation with all seven stable isotopes of xenon clearly distinguishable. At Xe^{15+} , mass 126 starts to overlap with mass 136 of Xe^{16+} and, at even shorter times, consecutive charge states increasingly merge. To obtain the charge-state distribution depicted in figure 4.4, a deconvolution procedure was employed for charge states above Xe^{23+} by adjusting the height of individual charge states in a simulated distribution until their sum matched the experimental spectrum (see section 3.3.2.3). Those charge states, where deconvolution becomes necessary, are magnified in the inset of figure 4.3. To determine the ion yield for the other charge states the time-of-flight peak for the isotope ^{132}Xe was integrated.

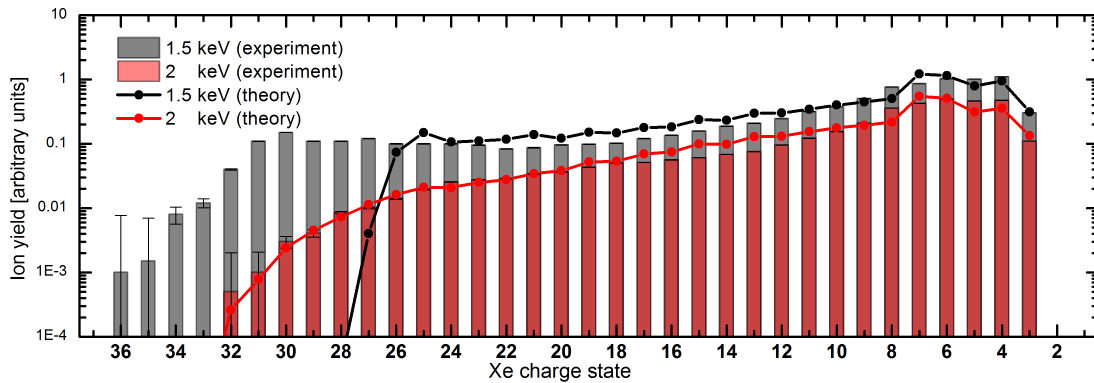


Figure 4.4 – Xenon charge-state distribution at 1.5 keV and 2 keV photon energy.

The data in figure 4.4 is compared to a theoretical model by S.-K. Son and R. Santra. In this model more than a million coupled rate equations -with photoionization cross sections and decay rates from non-relativistic Hartree-Fock-Slater calculations- were numerically solved (see section 2.2.4.2). The sum of each theoretical charge-state distribution is normalized to the sum of the corresponding experimental distributions; a logarithmic scale is chosen to zoom into low yields of highly charged ions. The calculated yields for the charge states Xe^{1+} and Xe^{2+} are not displayed as they were out of range in the experimental time-of-flight spectrum.

In general, the ion yield per X-ray pulse is found to be lower for 2 keV than for 1.5 keV photon energy throughout the time-of-flight spectrum. Apparently, the higher fluence at 2 keV is more than compensated by the lower cross sections for

M-shell ionization (at 2 keV the L-shell is still out of reach even for two-photon ionization). Additionally, the number of photons is lower at higher photon energy when the same pulse energy is chosen.

For both photon energies the experimental spectra are somewhat smoother than the predicted ones if one inspects them in detail on a linear scale. Then in the theoretical distributions a pronounced minimum at Xe^{5+} and a maximum at Xe^{7+} are observable and between Xe^{10+} and Xe^{20+} odd-even charge-state alternations appear. Such alternations have been previously attributed to the disregard of shake-off and double Auger processes by the calculations [19]. Here, the shake-off process (see section 2.2.2.4) is included for 0+ and 1+. Double Auger or Auger satellites (see section 2.2.2.5) are not considered.

The overall trend of the charge-state yields for the 2 keV case is predicted very well with some divergence in the relative yield between Xe^{10+} - Xe^{20+} , which is experimentally found to be lower. For Xe^{31+} and Xe^{32+} the relative ion yield is smaller than 10^{-3} and the absolute experimental error (indicated as thin black lines) increases to the same order of magnitude. For 1.5 keV photon energy, however, the experimental charge-state distribution deviates drastically from the theory values. The calculations predict a maximum charge state of $\sim\text{Xe}^{27+}$, while the recorded data show charge states up to Xe^{36+} .

4.2.2 Discussion of the Xenon Charge-State Distribution

Photoionization of xenon at FEL-typical irradiance levels of 10^{16} W/cm² has previously been investigated at the Extreme Ultra-Violet (XUV) free-electron laser in Hamburg, FLASH [31]. Surprisingly high charge states q up to Xe^{21+} have been observed at 93 eV photon energy, i.e. $\lambda = 13.3$ nm. While resonant excitation ionization processes have been considered as catalyzers of sequential multiphoton ionization, the main contribution to multiple ionization at highest q has been attributed to direct multiphoton ionization by up to seven photons [31, 159]. Also, non-perturbative strong-field phenomena [31] and many-electron effects [160] have been speculated to play a role.

While pulse intensities here are comparable to those achieved in the FLASH experiment, much higher photon energies of 1.5 keV and 2.0 keV, respectively, were used. Due to the $1/\omega^2$ dependence of the ponderomotive force, strong-field effects are expected to play a negligible role and any non-perturbative effects can be safely

neglected. Also, direct multiphoton ionization was found to play a minor role [20, 24, 25]. At X-ray energies, photoionization in general proceeds predominantly via a sequence of single-photon ionization steps of the lowest accessible inner-shell orbitals (see section 2.2.2.4 and 2.2.4.1) and, hereafter, the inner-shell vacancy is filled by outer-shell electrons in a decay cascade (section 2.2.2.5).

The lowest accessible inner-shell orbital is shown in figure 4.5, where the orbital binding energy of the electronic ground-states from 3s to 20s orbitals are plotted against the xenon charge state. The ground-state configuration of neutral xenon is

$$1s^2 2s^2 2p^6 3s^2 3p^6 3d^{10} 4s^2 4d^6 4f^{14} 5s^2 5p^6, \quad (4.1)$$

hereafter abbreviated as $[Ne]3s^2 3p^6 3d^{10} 4s^2 4d^6 4f^{14} 5s^2 5p^6$. To indicate the available photon energies dashed red horizontal lines are drawn, which intersect the M-shell (3s, 3p, 3d) binding energies at certain charge states. Sequential single-photon ionization implies, that the photoionization will stop as soon as the binding energies of the not-yet-ionized electrons falls below the respective red line denoting a given photon energy.

Accordingly, for 2 keV photon energy single-photon ionization closes at the charge state Xe^{32+} : With the ground-state configuration $[Ne]3s^2 3p^6 3d^4$, the least-bound electrons are those in 3d, which have a binding energy of 2018 eV. In the charge-state distribution for 2 keV depicted in figure 4.4 the highest charge state predicted and detected experimentally nicely coincide to be exactly $q = 32$. Apparently, the underlying basic process of sequential single-photon ionization is well described by the theoretical model and no additional processes appear for 2 keV according to the experimental spectrum.

For 1.5 keV photon energy single-photon ionization closes at the charge state Xe^{26+} where, in ground-state configuration, all electrons higher than 3d are emitted, $[Ne]3s^2 3p^6 3d^{10}$. The binding energy for 3d electrons at $q = 26$ is 1509 eV so that a maximum charge state of Xe^{26+} is expected.

In striking contrast to these simple considerations as well as to the theoretical prediction, charge states as high as 36+ are observed at a photon energy of 1.5 keV (figure 4.4). Here, sequential single-photon ionization can not explain the total ionization process and additional pathways have to be considered above Xe^{26+} .

At low charge states ($q < 18$), ionization from the $n = 3$ core-shell is most efficient as obvious from figure 4.5, blue arrow. Photoionization cross sections for the individual orbitals in the ground-state configuration of neutral xenon at 1.5 keV photon

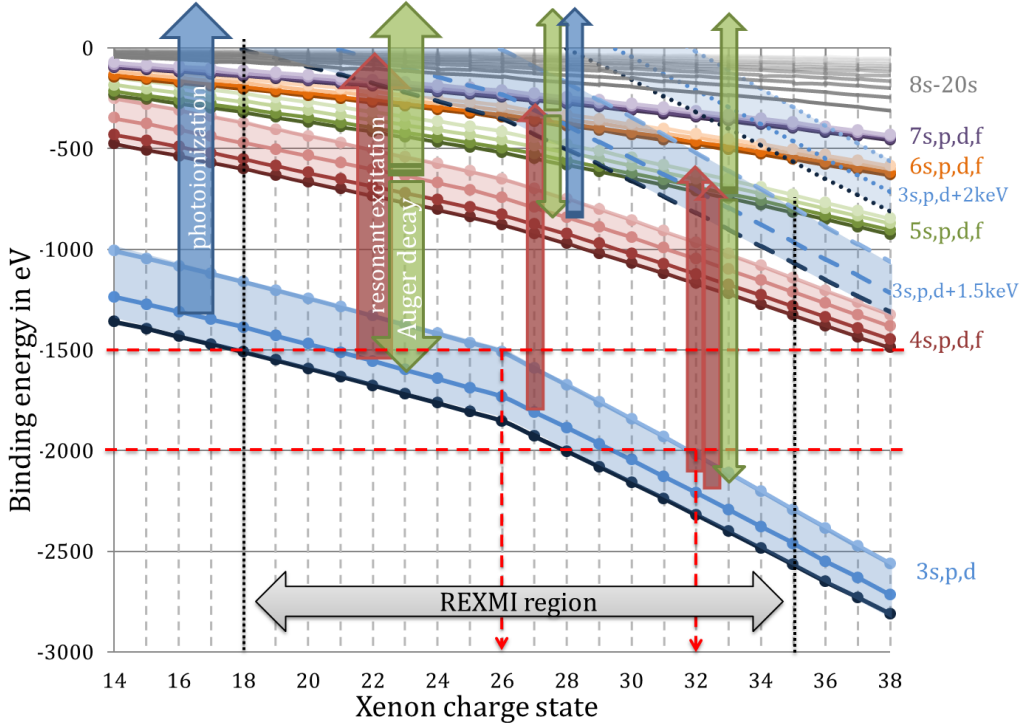


Figure 4.5 – Xenon orbital binding energies as a function of the degree of ionization calculated with the Hartree-Fock method; the states 8 to 20 are calculated with the formula for the binding energy of Rydberg levels, equation 2.32. The dashed and dotted blue lines mark the resonances from 3s, 3p and 3d states at 1.5 keV and 2 keV photon energy, respectively.

energy are summed up in table 4.2. Upon photoionization, the $n=3$ vacancies are

Orbital	3d	3p	4d	3s	4p	4s
Photoionization cross section	494 kb	223 kb	63 kb	54 kb	48 kb	14 kb

Table 4.2 – Photoionization cross sections in the ground-state configuration of neutral xenon at 1.5 keV photon energy [106–108].

filled via Auger decay, which further increases the charge state.

Towards $q = 24$ the 3d-hole Auger lifetime becomes comparable to the average 3d photoionization rate for 1.5 keV photon energy and at a fluence of $50 \mu\text{J}/\mu\text{m}^2$, see figure 4.6. For this configuration $n = 3$ electrons will be ionized faster than the remaining holes can be filled via Auger decay resulting in the creation of multiple core-holes. M-shell ionization ends at a charge state of 26+, so direct ionization is closed, but Auger decay of multiple core holes still lead to charge states slightly

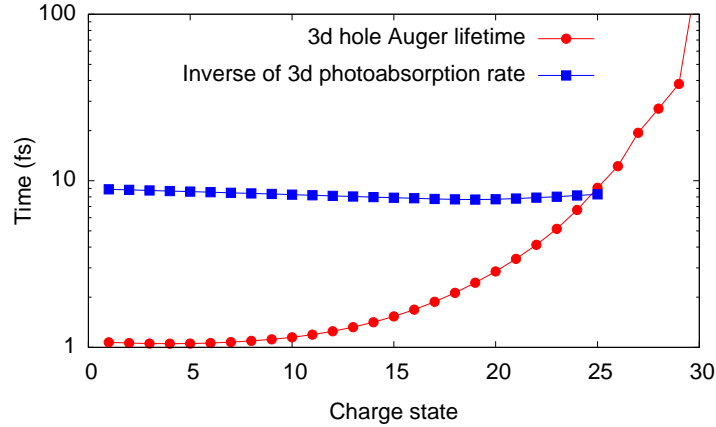


Figure 4.6 – Xenon 3d single-hole Auger life time and inverse 3d photoabsorption rate as a function of charge state for a fluence of $50 \mu\text{J}/\mu\text{m}^2$.

above Xe^{26+} as seen in the calculated charge-state distribution in figure 4.4.

The creation of hollow atoms under ultra-intense X-ray irradiation is a well accepted phenomenon at X-FELs. It was predicted even before the first X-FEL was operating [24] and has been investigated in detail for small systems such as neon [19] and nitrogen [21–23] since LCLS started operation. While Auger decay into multiple core holes can indeed push the ionization above the limit for sequential single-photon ionization, it cannot account for the strong enhancement of photoionization observed in the recorded xenon time-of-flight spectrum 4.3.

At $26+$, an extremely efficient process, that is not included in the calculation, starts boosting multiple ionization as illustrated schematically in figure 4.5. Above Xe^{18+} electrons can be resonantly excited (red arrows) into Rydberg states (grey). Then subsequently, with increasing charge state, into $n = 7$, $n = 6$ and $n = 5$, when the 3s, 3p and 3d orbitals have a 1.5 keV energy difference with those valence states. The resonant excitation stops at around $q = 35$ due to the large energy gap between $n = 4$ and $n = 5$.

Auger or autoionizing transitions of these multiple and highly excited hollow-atom states efficiently deplete the higher shells (green arrows), and, furthermore, refill the 3s, 3p and 3d levels continuously. Electrons from refilled 3s, 3p and 3d states may then again be resonantly excited. Because these resonances enable ionization at charge states, where direct single-photon ionization is forbidden, this process may be called resonance-enabled X-ray multiple ionization (REXMI) pathway.

The effectiveness of fast Auger and autoionization decay processes of hollow atoms

has experimentally been observed [161] and theoretically proven [162] in electron emission and hollow-atom formation occurring when highly charged ions slowly approach insulator and metal surfaces. This effect was first observed by Briand [163] in 1996 and extensively investigated in the following years [164].

Direct photoionization of the $n = 4$ shells (and above), filled by resonant excitation or during Auger decay of resonant excited states, is energetically possible as well. However, the direct photoionization of Rydberg or valence states immediately after resonant excitation has a very low cross section. The highest cross section is found for 5p valence ionization of Xe^{35+} ($[\text{Ne}]3s^23p^65p^1$) where the ionization potential is closest to 1.5 keV. It amounts to 0.01 Mb [165]. In comparison, photoionization of the 3d orbital from neutral xenon has a cross section of about 0.5 Mb and bandwidth convolved resonant excitations have cross sections of about 1 Mb, see figure 4.18. With the cross section of 0.01 Mb, the fluorescence rate is higher than the photoionization rate even at the highest fluence of $44 \mu\text{J}/\mu\text{m}^2$ [165]. Therefore, resonant excited states cannot be regarded as intermediate states involved in direct multiphoton ionization, but rather as starting point of Auger decay and autoionization. Thus, the REXMI mechanism is fundamentally different from resonance-enhanced multiphoton ionization (REMPI), discussed in section 2.2.3.1.

Interestingly, from the level diagram in figure 4.5 one might expect that REXMI becomes already less effective for charge states larger than about $q = 31$ where resonant excitation into $n = 6$ ends. Resonances into $n = 6$ enable an efficient two-step ionization pathway with only one additional Auger decay involving $n = 4$ and near continuum levels. Indeed, the experimental charge-state distribution in figure 4.4 clearly shows a plateau in multiphoton ionization probability until $q = 31$ with a strong decrease towards $q = 36$. In ground-state configuration the 3d orbital is depleted at Xe^{36+} , $[\text{Ne}]3s^23p^6$, and resonant excitation from the 3d orbital to the 5th shell is energetically not possible anymore implying a maximum charge state of Xe^{36+} , as observed in the time-of-flight spectrum.

It should also be mentioned that resonance-enhanced multiple ionization is not limited to the 1.5 keV case (dashed line in figure 4.4), but is expected for 2 keV photon energy as well, which is indicated with dotted lines in figure 4.4. Nevertheless, with the reduced photon flux and cross section at 2 keV photon energy and the maximum fluence of $86 \mu\text{J}/\mu\text{m}^2$, the charge-state distribution ends already at $q = 32$ just before entering the photon-energy-specific REXMI region (see also figure 4.17).

4.2.3 Ion Spectra of Krypton

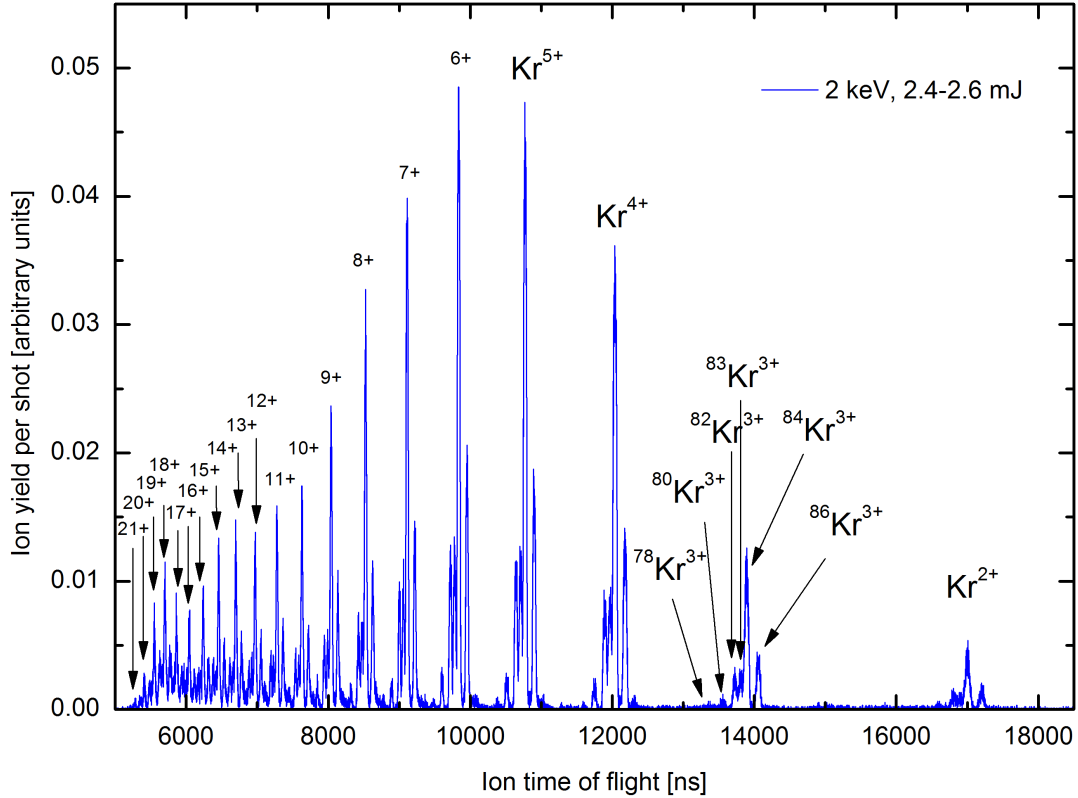


Figure 4.7 – Krypton ion time-of-flight spectrum at 2 keV photon energy.

Figure 4.7 depicts the krypton ion time-of-flight spectrum integrated over a pulse energy interval of 2.4 mJ to 2.6 mJ. The six stable isotopes are distinguishable for low charge states. Krypton has less stable isotopes than xenon and its isotopic distribution has a pronounced peak at mass ^{84}Kr with 57% isotopic abundance. Therefore, and because the krypton time-of-flight spectrum shows a maximum charge state that is considerably lower than in the xenon spectrum, a deconvolution of the time-of-flight spectrum is not necessary and integration of the $^{84}\text{Kr}^{q+}$ peak directly yields the charge-state distribution shown in figure 4.8.

In figure 4.8 the krypton data is drawn as blue bars and the corresponding calculation as blue line. Krypton has been investigated at the same experimental parameters as xenon at 2 keV photon energy ($\lambda = 0.6$ nm), so the theory also assumes the same parameters (80 fs pulse length, 2.5 mJ pulse energy with 35% beamline transmission and a $3 \mu\text{m} \times 3 \mu\text{m}$ FWHM of a circular Gaussian-shaped pulse). Again, the shake-off process is included for 0+ and 1+, double Auger or Auger satellites

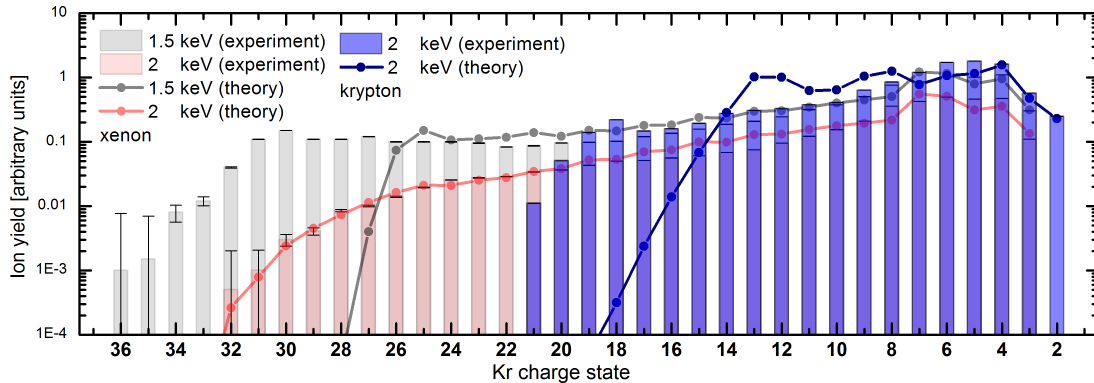


Figure 4.8 – Krypton charge-state distribution at 2 keV photon energy (in blue).

are not considered. For comparison the xenon results are plotted in the background (light red and black).

The experimental charge-state distribution peaks at Kr^{5+} , then decreases for higher charge states, but shows another local peak at Kr^{18+} . The highest recorded charge state is Kr^{21+} . With respect to the overall shape, the krypton charge-state distribution is closer to the Xe 1.5 keV than the Xe 2 keV case. The calculated charge-state distribution has three peaks, at Kr^{4+} , Kr^{8+} and Kr^{13+} . The predicted peak at 8+ in the theory line appeared for multi- as well as for single-photon ionization and was attributed to the lack of relativistic effects in the calculations [166] (spin-orbit splitting of the 2p shell could open more decay channels and smoothen the 8+ peak). After the Kr^{13+} peak the ion yield constantly decreases. The highest calculated charge state (in the depicted scale) is Kr^{18+} .

4.2.4 Discussion of the Krypton Charge-State Distribution

At 2 keV photon energy, L-shell ionization for krypton is open and photoionization of the krypton 2s and 2p shells have the highest cross section. Photoionization is accompanied by shake-off processes and Auger decay. Single-photon ionization of the 2s orbital leads via an Auger cascade to a charge state up to 10+ with the highest yield for Kr^{7+} according to synchrotron measurements [112] and calculations [167]. An exemplary Auger cascade upon 2s photoionization in krypton is shown in table 4.3.

As the orbital binding energies increases during the ionization process, the 2s ionization channel of krypton is closed at Kr^{+9} and direct 2p photoionization is

Transition	Name	Lifetime
$\text{Kr}^+(2s^{-1}) \rightarrow \text{Kr}^{2+}(2p^{-1}3d^{-1})$	LLM-Auger	$\tau = 160$ as
$\text{Kr}^{2+}(2p^{-1}3d^{-1}) \rightarrow \text{Kr}^{3+}(3d^{-3})$	LMM-Auger	$\tau = 560$ as
$\text{Kr}^{3+}(3d^{-3}) \rightarrow \text{Kr}^{4+}(3d^{-2}4s^{-1}4p^{-1})$	MMN-Auger	$\tau = 7$ fs
$\text{Kr}^{4+}(3d^{-2}4s^{-1}4p^{-1}) \rightarrow \text{Kr}^{5+}(3d^{-1}4s^{-2}4p^{-2})$	MNN-Auger	$\tau = 18$ fs
$\text{Kr}^{5+}(3d^{-1}4s^{-2}4p^{-2}) \rightarrow \text{Kr}^{6+}(4s^{-2}4p^{-4})$	MNN-Auger	$\tau = 155$ fs

Table 4.3 – Exemplary Auger cascade upon 2s photoionization in krypton [68].

closed at Kr^{+13} at 2 keV photon energy (see dashed red arrow in figure 4.9). The peak at $q = 13$ in the calculated charge-state distribution is mainly due to closing of the direct 2p photoionization, where the photoionization cross section for further ionization dramatically decreases after $q = 13$. The higher charge states beyond $q = 13$ are generated by multiple-core-hole formation, within the current theoretical model. At $q = 13$ the electronic configuration of krypton in the ground-state is $[\text{Ne}]3s^23p^63d^5$ so that M-shell ionizations may occur but with very low cross sections compared to L-shell ionization at lower charge states [166]. That is why the theory curve rapidly decreases after $q = 13$. In the experimental spectrum, however, charge states up to $q = 21$ are observed.

The ground-state binding energies of the L, M, N, O and P shells for krypton ions up to a charge state of 22+ are illustrated in figure 4.9. The purple area parallel to the binding energies of the L-shell mark possible resonances at 2 keV photon energy. At Kr^{9+} , 2s direct photoionization is closed and resonant excitation from 2s into Rydberg orbitals opens instead. Figure 4.9 illustrates that, as for xenon, resonance-enabled X-ray multiple ionization (REXMI) can occur between Kr^{9+} and Kr^{20+} at 2 keV photon energy. Within the REXMI region, Auger decay is refueling the ongoing ionization after resonant excitation. At 20+ the energy difference between 2p and 4s exceeds the available photon energy of 2 keV and resonant excitation is stopped. Auger decay may remove another electron of excited Kr^{20+} resulting in a maximum charge state of 21+. Again this simple model is in astonishingly good agreement with the experimental results.

4.3. Ion Yield vs. Fluence: How Many Photons are Involved in the Ionization?

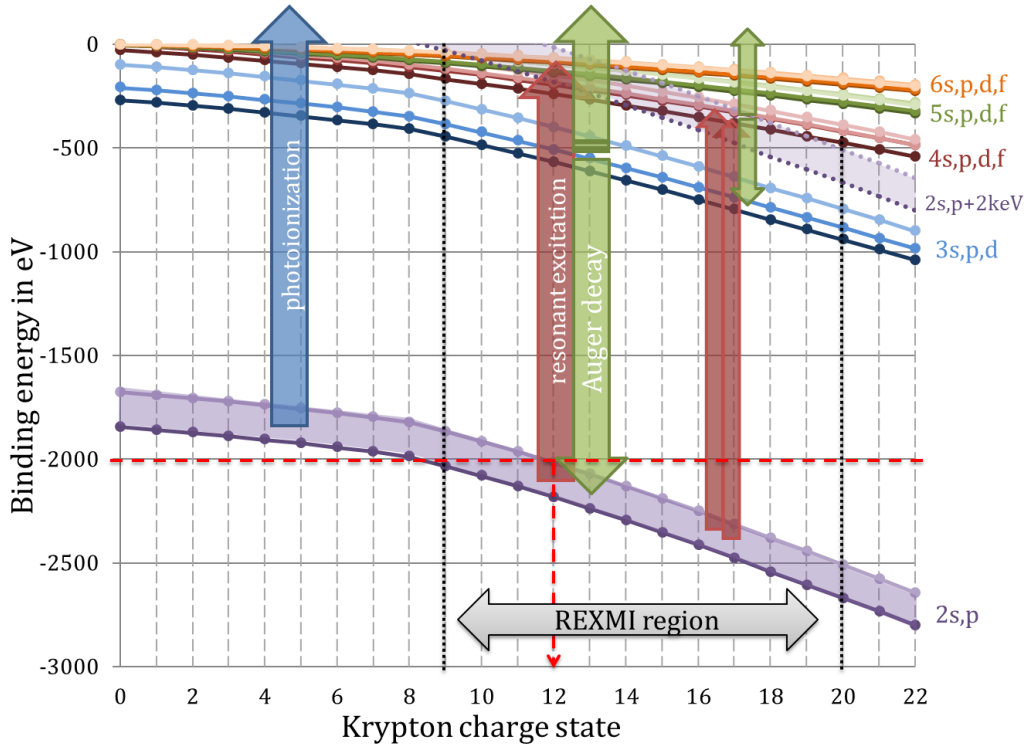


Figure 4.9 – Krypton orbital binding energies as a function of the degree of ionization. The dotted blue lines mark the resonances from 2s and 2p at 2 keV photon energy.

4.3 Ion Yield vs. Fluence: How Many Photons are Involved in the Ionization?

4.3.1 Xenon at 80 fs Pulse Length

The minimum number of absorbed photons during the ionization process can easily be estimated by summing up ground-state binding-energies of ionized orbitals: in table 4.4 the sum is calculated for exemplarily charge states with the binding energies taken from figure 4.5. This approach assumes that the total energy of an absorbed photon is used for the ionization process, whereas in an actual photoionization a significant fraction of the total energy is carried away by the photo- and Auger-electrons. Hence, these numbers can just be regarded as lower limit for the number of absorbed photons.

In the second chapter (2.2.3.1) multiphoton ionization was treated with perturbation theory and it was derived that the multiphoton transition probability is a

Charge state	Sum of binding energies	Divided by 1500 eV	Divided by 2 keV
5	156 eV	0.1	0.1
10	804 eV	0.5	0.4
15	2252 eV	1.5	1.1
20	4610 eV	3.1	2.3
25	8064 eV	5.4	4.0
28	12185 eV	8.1	6.1
30	15785 eV	10.5	7.9
32	19734 eV	13.2	9.9
34	24041 eV	16.0	12.0
36	28794 eV	19.2	14.4

Table 4.4 – Minimum number of absorbed photons needed to create a given charge state

function of the intensity to the power of n , where n is the number of absorbed photons (see equation 2.37). In the experiment the transition rate is measured by the ion yield. To derive the number of photons, the detected ion yield is plotted against the pulse energy measured by the GMD in a double logarithmic plot so that the slope of the yield curves implies the number of absorbed photons.

To correlate pulse energy and ion yield, the time-of-flight spectrum is sorted with respect to the pulse energy for every shot and plotted into a 2D graph with the GMD value on the y- and the time-of-flight spectrum on the x-axis (figure 4.10 on the left). Then a y-projection, within the time-of-flight window for a particular charge state, yields its pulse energy dependence of that charge state; for charge states with coalesced peaks a deconvolution factor is applied (see section 3.3.2.3).

The projection has to be divided by the pulse energy distribution to normalize on the number of shots at certain pulse energy; here, the binning of both, projection (numerator) and distribution (denominator), has to be coarse enough to avoid normalization artifacts.

Finally, the linearity of the GMD signal has to be verified by cross calibration with the measured proton signal as discussed in section 3.1.3.3. For low pulse energies, i.e. high gas pressures in the attenuator, the GMD was found to yield higher pulse energies than estimated by means of the proton count rate and, thus, the pulse energy has been recalibrated in this region. Saturation at pulse energies above

4.3. Ion Yield vs. Fluence: How Many Photons are Involved in the Ionization?

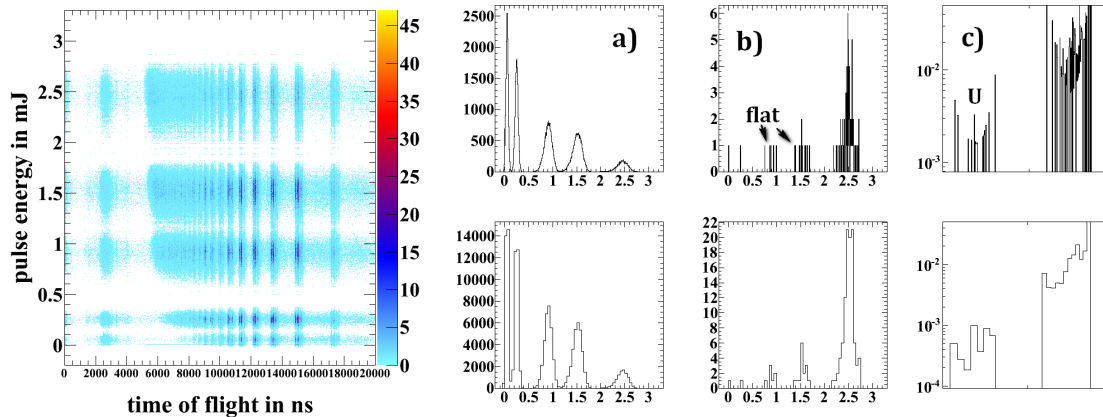


Figure 4.10 – On the left: 2D graph with the GMD pulse energy value vs. time-of-flight spectrum filled shot by shot. a) GMD pulse energy distribution of all shots; b) y-projection of the 3D graph within the Xe^{33+} time-of-flight window; c) y-projection divided by GMD distribution, i.e. the normalized ion yield for Xe^{33+} , zoomed in and in double-logarithmic scale. In the lower row the spectra are rebinned to 10-fold larger bins to avoid flat y-projections, which lead to U-shaped artifacts in the normalized ion yield.

2 mJ, as indicated by the FLASH GMD and the ASG intensity monitor (see section 3.1.3.5), has not been corrected for. A correction would move data points to higher pulse energies (2.5 mJ to 3.5 mJ, for instance) and thereby flatten the slope of the yield curves beyond ~ 1.8 mJ. However, above 2 mJ the ion yields for all but the highest charge state are already saturated anyways, such that a correction would not affect the slopes of these yield curves which are only evaluated below saturation occurs.

The pulse-energy-dependent ion yield of several exemplary charge states are depicted in figure 4.11 and compared to theory for a) 1.5 keV and b) 2 keV photon energy. Both graphs have double logarithmic scales with the peak fluence on the x- and the ion yield on the y-axis, so that the slope of a straight line yields the number of absorbed photons. To guide the eye, lines with integer slopes are matched to the data, from which the number of absorbed photons can be estimated. The lines are attached to regions in the intensity dependence below the experimental ion yields start to saturate due to target depletion.

The theoretically calculated ion yields in figure 4.11 are integrated over the 3-dimensional interaction volume defined by the intersection of two Gaussian pro-

files, the circular Gaussian X-ray beam ($3 \times 3 \mu\text{m}^2$ FWHM) and the circular Gaussian gas jet profile (4 mm FWHM). Due to the large detector acceptance of 80 mm, tails of the Gaussian gas jet distribution, which reach far into the low-fluence part of the FEL beam, are included in the calculation.

Error bars are calculated including error propagation from the standard deviation of the individual ion yields at certain fluence and the total number of shots at this fluence, which is used for normalization. The standard deviation of a count rate is the square root of that count rate.

4.3. Ion Yield vs. Fluence: How Many Photons are Involved in the Ionization?

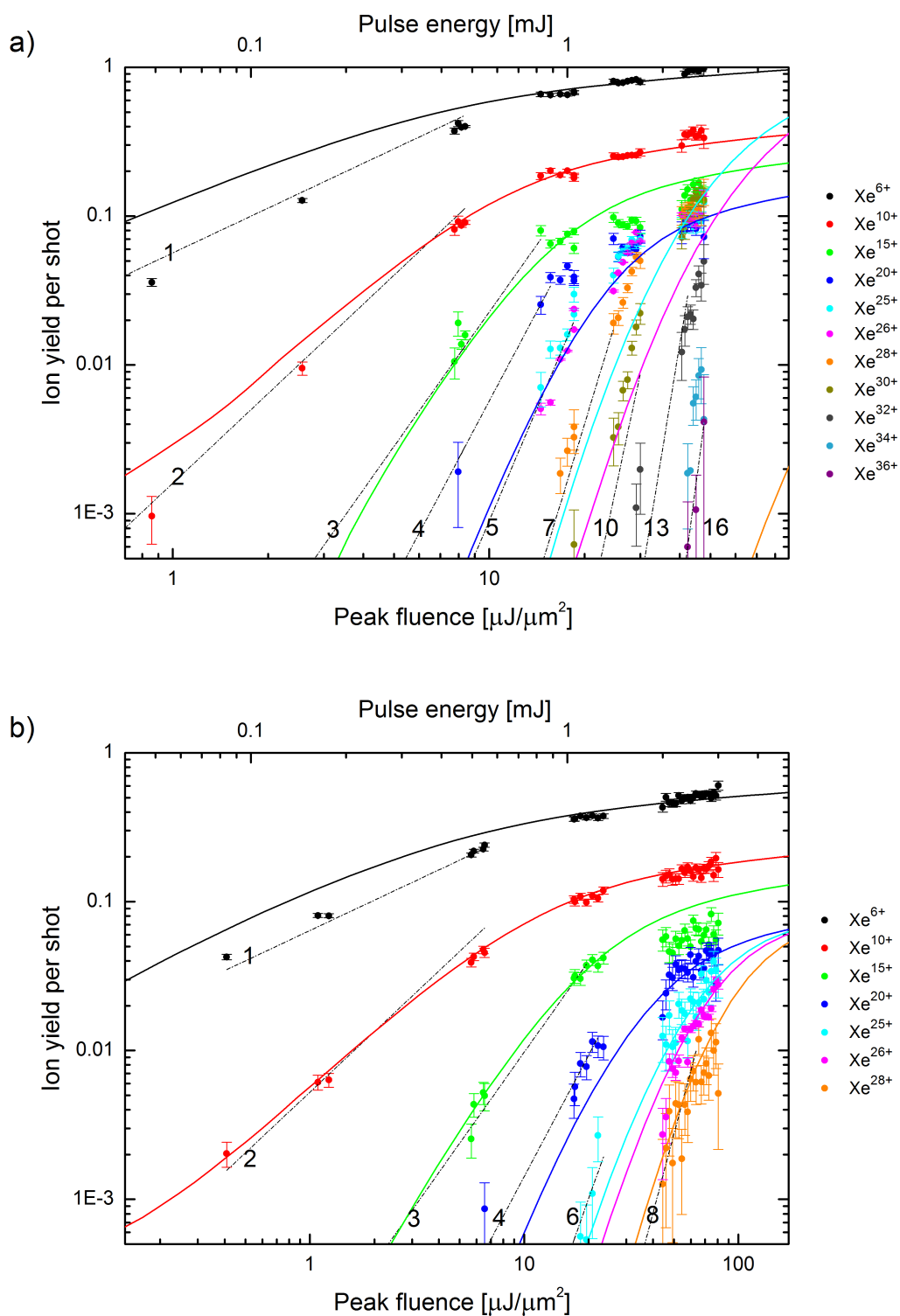


Figure 4.11 – Experimental (data points) and calculated (solid lines) xenon ion yield vs. peak fluence at a) 1.5 keV photon energy, and b) 2 keV photon energy. Integer slopes are added to guide the eye.

4.3.2 Discussion of the Ion Yields for Xenon

Synchrotron data provides information about the charge-state distribution upon single-photon absorption. For xenon single-photon M-shell ionization, charge states up to 11+ are reported [112, 113]. In these publications the charge-state distribution peaks at 7+ where the ion yield is more than two orders of magnitude higher than for 11+. Consistently, the Xe^{6+} yield curve follows a line with slope one. In average the ionization to Xe^{9+} requires the absorption of two photons and, thus, is best fitted by a line with slope two. The number of absorbed photons for Xe^{15+} is 3, for Xe^{20+} 4, for Xe^{25+} roughly 5, for Xe^{28+} about 7; for 30+, 32+ and 36+ the slopes suggest numbers of 10, 13 and 16, however, with large uncertainty.

Within that uncertainty the number of absorbed photons for photoionization at 1.5 keV and 2 keV photon energy is about the same. That is reasonable, as ionization proceeds through M-shell photoionization at both energies with the L-shell far out of reach even at 2 keV. Double ionization processes, which might be enhanced at 2 keV by the higher excess energy, are not considered in the calculations and the experimental statistics is too low to resolve such rare processes.

The calculated yield-curves are in very good agreement with the experimentally determined slopes as long as resonances play a minor role: they fit for all charge states at 2 keV photon energy and up to $q = 20$ in the 1.5 keV case. For 1.5 keV resonant excitation starts at $q = 18$ according to figure 4.5. With the very efficient ionization through the REXMI pathway, the actual photoionization cross section is higher than predicted by the theory. Thus, the experimental yield curves are shifted to lower fluences, as soon as multiple ionization via resonant excitation plays a role. The calculated yield curve for $q = 28$, in particular, is very much off, since 3p photoionization is closed at $q = 26$ and further ionization in the theoretical model can just proceed via Auger decay of multiple core-excited states.

The number of absorbed photons, derived from the yield curves, gets closer to the estimated minimum in table 4.4 with increasing charge state. On one hand the ionization potential is closer to the impinging photon energy at high charge states and less energy is carried away by the photoelectron. Thus the minimum number of absorbed photons in table 4.4 is closer to the actual number of photons required for the ionization. On the other hand resonances may reduce the slope of experimental yield curves, as discussed in section 2.2.3.1, so that the number of absorbed photons,

derived from the yield curves, is reduced.

4.3.3 Krypton at 80 fs Pulse Length

As described for the case of xenon above, the minimum number of absorbed photons for krypton is depicted in table 4.5. Accordingly, ionization by a single photon may lead up to Kr^{10+} , which also was the highest charge state created by L-shell photoionization in synchrotron measurements [112]. The average charge state in these experiments, however, was 6.7 for 2s photoionization and 5 for 2p photoionization.

Charge state	Sum of binding energies	Divided by 2 keV
5	183 eV	0.1
10	1000 eV	0.5
15	3003 eV	1.5
20	6392 eV	3.2

Table 4.5 – Minimum number of absorbed photons needed to create a given charge state.

In figure 4.12, the experimental and calculated ion yields for selected krypton charge states are plotted as a function of the peak fluence. The theory lines are 3D volume-averaged as for xenon and normalized as in the charge-state distribution at 2.5 mJ pulse energy (figure 4.8).

4.3.4 Discussion of the Ion Yield of Krypton

While the experimental and calculated slopes fit quite well in general, some curves differ in the absolute ion yield per shot and the position on the fluence axis, for example Kr^{14+} , Kr^{16+} and Kr^{20+} .

Moreover, the experimental Kr^{6+} curves saturates later than predicted. As Kr^{6+} is created by single-photon ionization, the delayed saturation implies that areas of low-fluence contribute more than assumed by the theory. The theoretical Kr^{9+} curve is higher for all fluences, probably due to the lack of relativistic effects in the calculations (as discussed for Kr^{8+} in section 4.2.4). According to the slope in figure 4.12, Kr^{9+} is created by two-photon ionization.

At 2 keV, the 2s ionization channel of Kr is closed at $q = 9$ and 2p ionization is closed at $q = 12$. Further ionization within the theoretical model is driven by

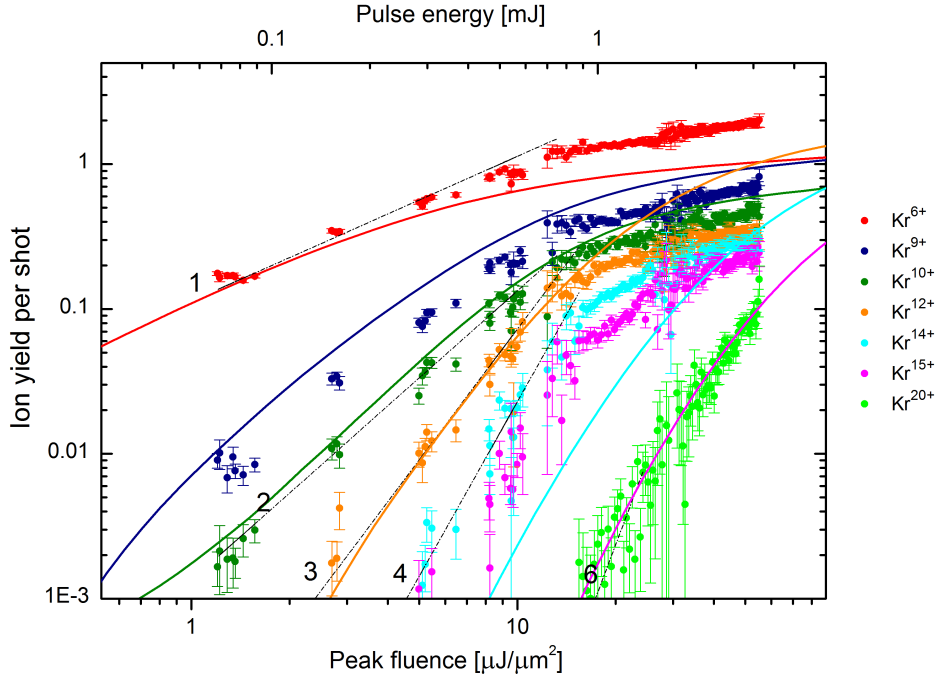


Figure 4.12 – Experimental (data points) and calculated (solid lines) krypton ion yield vs. peak fluence at 2 keV photon energy. Integer slopes are added to guide the eye.

Auger decay into multiple core holes or valence ionization, which, however, has a much lower cross section. In the actual experiment, resonances govern the ionization process after closing of the direct L-shell photoionization and enhance the photoionization dramatically. Thus, the experimental data is shifted towards lower fluences due to higher cross sections as soon as resonant transition play a role in the photoionization process, i.e. beyond Kr^{12+} . From the slopes of the ion yield curves the number of absorbed photons is 3 for Kr^{12+} , about 4 for Kr^{14+} and about 6 for Kr^{20+} . As the slopes of the experimental and theoretical curves do not significantly differ, the resonant transitions do not seem to be saturated, which would result in a reduced slope in the experimental data (see section 2.2.3.1).

4.3.5 Photoionization of Krypton at 3 fs Pulse Length

Figure 4.13 depicts the time-of-flight spectra for krypton at 2 keV photon energy at two different pulse lengths. To achieve pulses as short as 3 fs the accelerator had to be operated in low-charge mode [77] (see section 3.1.1.2). Hence, the maximum pulse energy was decreased from 2.5 mJ to 0.5 mJ. In order to compare data with

4.3. Ion Yield vs. Fluence: How Many Photons are Involved in the Ionization?

long and short pulse lengths, the 80 fs pulse length beam was attenuated by gas absorbers (see section 3.1.3.4) from the maximum pulse energy of 2.5 mJ down to about 0.5 mJ. In figure 4.13 the short pulse data is drawn in red, the long pulse data in black. Because the short pulse data was recorded with higher spectrometer voltage, the time-of-flight spectrum is shifted to shorter times. To match short and long pulse data, both data sets have their own time-of-flight axis (in red and black, respectively).

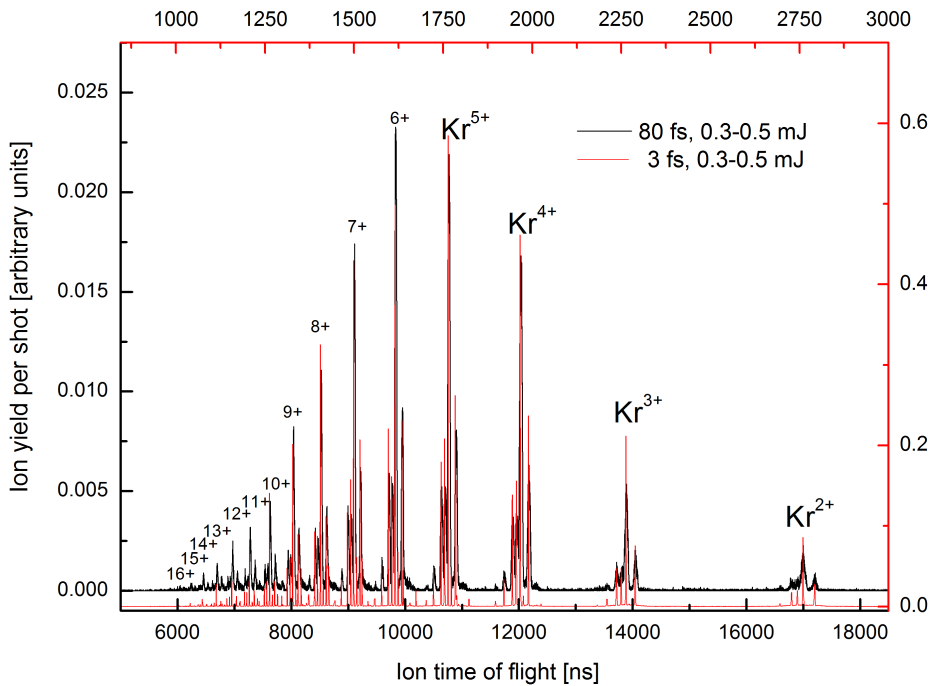


Figure 4.13 – Krypton ion time-of-flight spectrum at 2 keV photon energy and 0.3 to 0.5 mJ pulse energy for 3 fs pulse length (red) and 80 fs pulse length (black).

In figure 4.14 the ion yields of the 3 fs measurement is plotted as a function of pulse energy as stars together with the 80 fs data (transparent data points) and theory curves from figure 4.14 (the same charge states as for the 80 fs data are shown). As seen in the time-of-flight spectrum, figure 4.13, the ion yield per bin in the short-pulse data is about twice as high as in the long-pulse data, since the higher extraction voltage on the spectrometer compresses the time-of-flight peaks to smaller time intervals. For the 3 fs data, the total time-of-flight peaks are integrated to determine the ion yield while the bounds of integration for the 80 fs data do not include the total time-of-flight peak. To account for the higher integrated ion yield, the 3 fs yield curves in figure 4.14 are divided by a constant factor to match the

80 fs data.

The calculated ion yield curves for 3 fs and 80 fs pulse length did not show any significant difference in the investigated pulse energy range, so that only the 80 fs ion yield curve is depicted in figure 4.14.

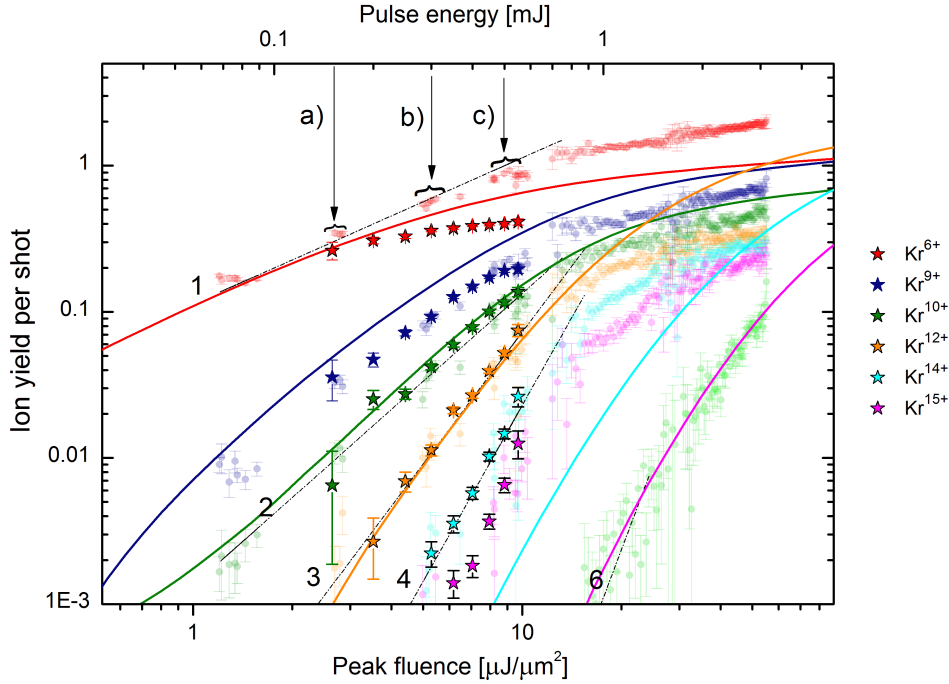


Figure 4.14 – Experimental (data points) and calculated (solid lines) krypton ion yield vs. peak fluence at 2 keV photon energy. The data for 3 fs pulse length is drawn as stars, the data for 80 fs pulse length as transparent dots. Integer slopes are added to guide the eye. The 3 fs data was recorded at one pulse energy setting with a width from 0.15 to 0.55 mJ. The pulse energy of the 80 fs data was reduced by the gas attenuator from full 2.5 mJ pulse energy down to three pulse energies a, b and c.

4.3.6 Discussion of the Ion Yields for Krypton (3 fs Pulse)

The photoionization of krypton was measured at two pulse lengths to investigate if it affects the photoionization pathways. When the pulse length is decreased but the pulse energy is hold constant, the pulse intensity increases (see equation 3.7). A higher intensity could, in principle, lead to direct two-photon absorption or to saturation of resonant excitation. Direct two-photon absorption would enhance the creation of highly charged states which cannot be reached with single-photon ionization. Saturation of resonances would decrease the slope of the ion yield curves

(sec. 2.2.3.1).

On the other hand, photoionization could be hampered in short pulses of high intensity. When the Auger decay time into an inner-shell hole exceeds the pulse duration, the cross section for total photoionization is reduced ("X-ray induced transparency for K-shell holes" [19, 21]) and the creation of highly charged states is suppressed.

In the experimental time-of-flight spectrum (figure 4.13), only charge states up to Kr^{16+} are observed due to the lower pulse energy of 0.5 mJ as compared to Kr^{21+} at 2.6 mJ (figure 4.7). The most intense peak is Kr^{6+} , which can be reached in one photoionization step. The fluence-dependent yield curves in figure 4.14 show, that a charge state up to 10+ can be reached by absorption of two photons of 2 keV photon energy. With three photons, krypton can be ionized to Kr^{12+} , but the total observed ion yield of Kr^{12+} is already ten times lower than for Kr^{6+} . The time-of-flight spectra for short and long pulse lengths do not significantly differ and neither do the slopes of the yield curves for 3 fs and 80 fs pulse length in figure 4.14. Apparently, the intensity is still too low for any two-photon ionization or saturation of resonances to occur. Moreover, no indication of X-ray induced transparency is observed, probably because too many electrons are accessible in the L-shell and because the Auger decay time into L-shell vacancies (see table 4.3) is too short.

The earlier saturation of Kr^{6+} and Kr^{9+} for the 3 fs pulses is probably due to the higher spectrometer voltage, which causes high but narrow time-of-flight peaks. These peaks can saturate the MCP-detector and merged peaks might be counted as one peak by the DAQ (sec. 3.3.2.1).

For the 3 fs data, a pulse energy interval of 0.15 mJ to 0.55 mJ, as measured by the LCLS GMD, is analyzed in figure 4.14. The width of this interval represents the stochastic pulse energy distribution due to the SASE process. At 80 fs pulse length a similar width around 0.3 mJ pulse energy is shown by the GMD. Here, however, the data was cross-calibrated with the measured proton signal as discussed in section 3.1.3.3. Due to this cross calibration, the pulse energy distribution of the attenuated data decreased to a small width, illustrated as (b) in figure 4.14 (the other data points at 0.15 mJ (a) and 0.5 mJ (c) were measured with a different attenuator pressure). From the comparison of initial stochastic pulse energy distribution of the FEL beam and the pulse energy distribution after attenuation, it seems that the initial distribution is somehow lost because of the attenuation by the gas absorber.

4.4 Fluorescence Spectra of Xenon: Radiative Transitions During Ionization

The evidence for resonant excitations of electrons from orbitals which are closed for direct photoionization at 1.5 keV photon energy is further substantiated by the simultaneous measurement of emitted fluorescence radiation indicating which inner-shell levels are depleted. In figure 4.15 a) the calculated fluorescence spectrum as provided by S.-K. Son for 1.5 keV photon energy and $50 \mu\text{J}/\mu\text{m}^2$, $25 \mu\text{J}/\mu\text{m}^2$ and $10 \mu\text{J}/\mu\text{m}^2$ fluence is shown. Neglecting resonances and, thus, with Xe^{26+} as the highest charge state, theory predicts fluorescent decay from 5s,p to 4s,p,d yielding lines between 100 eV and 400 eV as well as the 4p to 3d transition at around 700 eV.

This is compared to the experimental fluorescence spectrum in figure 4.15 b) with fluences between 11 and $44 \mu\text{J}/\mu\text{m}^2$. The spectra are normalized on the stray-light peak, i.e. the number of incoming photons, and smoothed by a running average over 35 eV.

Three general features occur for all fluences: electronic noise from the pnCCDs and its readout electronics below 150 eV (masked area), an oxygen line around 500 eV from background gas and the stray-light peak at 1500 eV. In addition, three clearly intensity-dependent Xe peaks appear centered at (i) 200 eV, (ii) 670 eV, and (iii) above 800 eV indicated in figure 4.15 as yellow, blue and red shaded areas, respectively. In contrast to the calculations, the low energetic 5s-to-4p,d transitions (i) seem to contribute less to the overall spectrum, while the 5p-to-4s fluorescence gives a significant onset to the oxygen $\text{K}\alpha$ line and the 4p-to-3d line (ii) is dominating at fluences from 18 to $41 \mu\text{J}/\mu\text{m}^2$. To explain the unexpected high fluorescence yield at 200 eV (i) and above 800 eV (iii), higher charge states than $26+$ as well as 3p hole creation after the direct 3d photoionization is closed - both missing in the theoretical model - have to be considered.

In figure 4.15 c) the energy of seven radiative decay channels in xenon ions from $20+$ to $36+$ are depicted as a function of charge state. The transition energies are calculated for ground-states. If other configurations were considered as well, the lines would gain a width of about plus minus 10 eV. Transition energies between shells increase with increasing charge state, while they decrease between subshells as electron repulsion within the ionized subshell is reduced (second Hund's rule).

4.4. Fluorescence Spectra of Xenon:
Radiative Transitions During Ionization

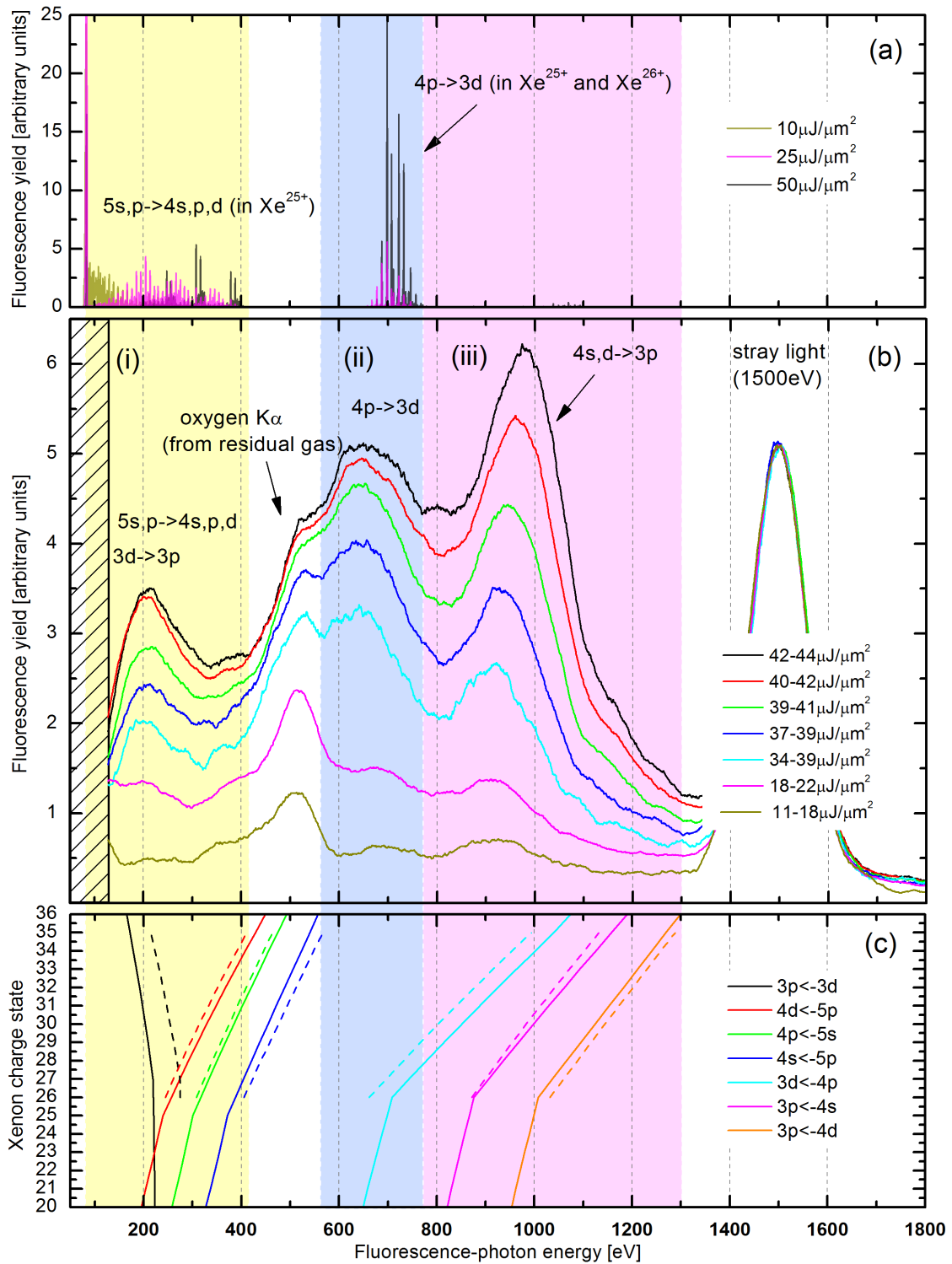


Figure 4.15 – Xe fluorescence spectra at 1500 eV photon energy. (a) depicts calculated spectra for three fluences, (b) is the experimental spectrum and (c) shows fluorescent transitions in charge states between Xe^{20+} and Xe^{36+} , for detailed description see text.

The solid lines are based on the non-relativistic Hartree-Fock-Slater method, whereas the dashed lines were calculated with the Cowan-code including relativistic effects [168]. According to these calculations in figure 4.15 (c), the fluorescence line at 200 eV can be attributed to the 3d to 3p transition and the lines above 800 eV to 4s to 3p or 4d to 3p transitions, respectively. The evidence of fluorescence decay into 3p, which has a binding energy well beyond the available photon energy for xenon ions above 20+, is a clear signature of resonant excitation.

neutral xenon contribute with 17%, but become less likely for higher charge states, e.g. for Xe^{6+} (after the Auger cascade of the first photoionization) the shake-off ratio is just 5% [68]. In the beginning even direct 3d double ionization is energetically possible. With increasing charge state, multi-electron ionization becomes negligible and Auger cascades shorter, as the number of partner-electrons for Auger decay is reduced.

At 18+ direct 3s ionization is closed for 1.5 keV photon energy and 3s can be resonantly excited into Rydberg orbitals hereafter. According to the calculated time-evolution of the charge state population shown in figure 4.17, charge state 18+ (thick green line) is reached at about the middle of the 80 fs pulse leaving enough time for further ionization enabled by transient resonances. In the 2 keV case, however, transient resonances at 28+ (thick red line) and above are reached too late in the pulse due to the lower cross section and, thus, cannot significantly contribute to the ionization process.

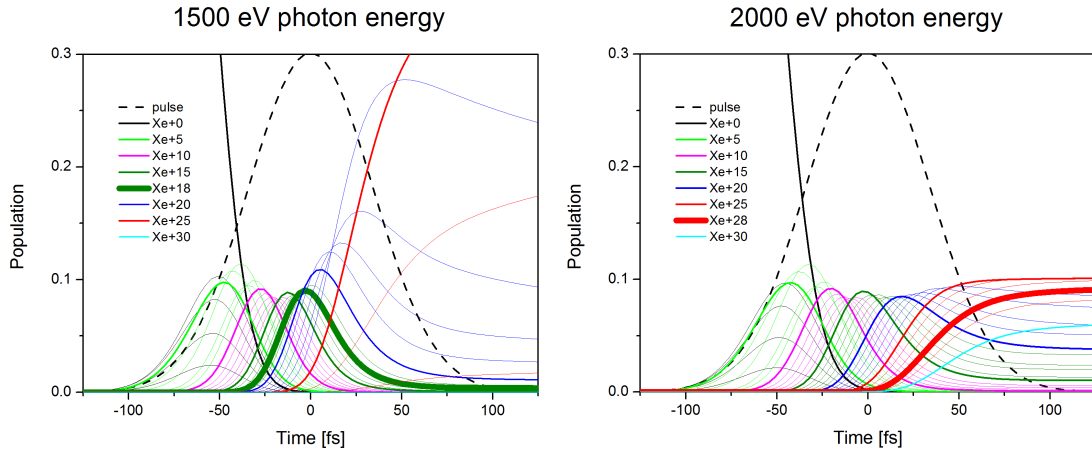


Figure 4.17 – Population of xenon charge states as a function of time during an 80 fs (FWHM) X-ray pulse calculated at 1.5 keV and 2 keV for an X-ray fluence of $50 \mu\text{mJ}/\mu\text{m}^2$ without inclusion of resonances.

Above Xe^{20+} the Auger decay time of the 3d hole exceeds the inverse 3d photoionization rate, resulting in multiple 3d holes. Direct photoionization of the 3d orbital can proceed until Xe^{26+} , but with multiple 3d holes Auger relaxation can lead up to $q = 28$, as seen in the charge-state distribution (figure 4.4).

4.5. Tracing back the Xenon Ionization Pathways

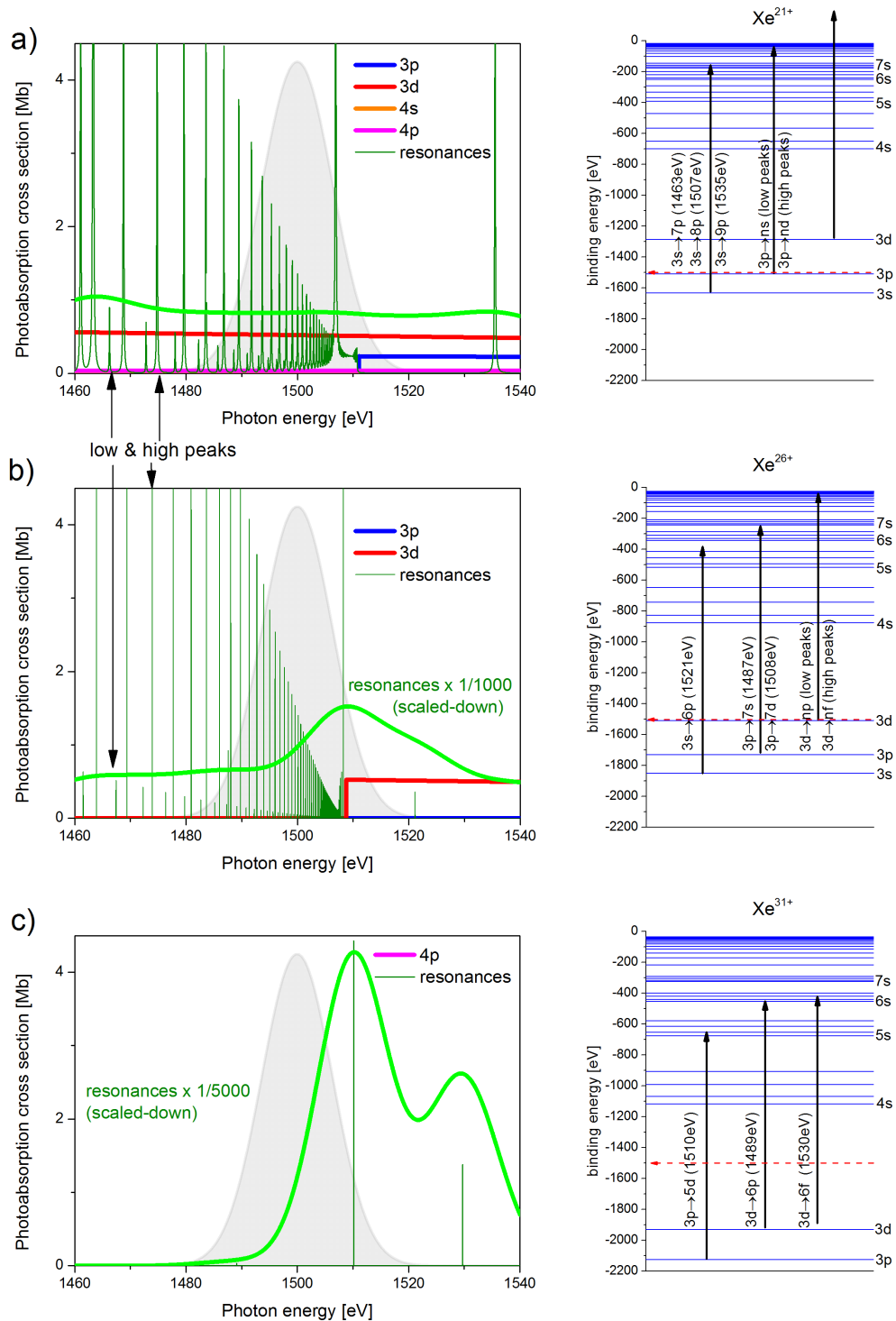


Figure 4.18 – Calculated photoabsorption cross sections around 1.5 keV photon energy for a) Xe^{21+} , b) Xe^{26+} and c) Xe^{31+} . Resonances are calculated from the ground-state configuration only. The photoabsorption cross sections for resonances and direct photoionization are convolved with a 15 eV bandwidth of the X-ray beam (light green line). The grey shaded area illustrates the photon energy distribution.

The cross sections for photoabsorption at three exemplary charge states in an energy window between 1460 eV and 1540 eV are shown in figure 4.18. All three graphs have the same scales. Resonant bound-bound transitions starting at the ground-state are included (dark green). The non-resonant photoabsorption cross section and cross sections for resonances are convolved with a 15 eV (FWHM) bandwidth and drawn in light green.

The step-size on the energy axis is 0.01 eV, but resonances can be even narrower. Because both, height and width, of the resonances are necessary to evaluate their strength, the overall strength of resonances cannot be directly read from the non-convolved sketch. The density of resonances ought to smoothly merge to the photoionization threshold of an orbital, here 3p and 3d (see section 2.2.2.3). In the energy level diagram on the right, possible transitions are indicated with arrows of 1500 eV length and the most prominent lines are named.

The selection rule for the angular momentum quantum number explains, why for example resonant excitation in xenon is possible between the 3p and 7s as well as 3p and 7d (for Xe^{26+} at 1487 eV and 1508 eV, respectively, see figure 4.18), but forbidden between 3p and 7p.

The three exemplary charge states are the following:

- In a), at a charge state of $21+$, direct 3d photoionization (red) is open and direct 3p photoionization (blue) is within the bandwidth of the photon energy (grey shaded area). Direct photoionization from 3d has the highest cross section, followed by direct the one from 3p; direct 4s and 4p photoionization are both negligible. Bound-bound-transitions between 3p and Rydberg states or 3s and the 7th and 8th-shell are possible as well. The broader width (compared to the resonances in graph b) and c) for Xe^{26+} and Xe^{31+} , respectively) is an artefact of the calculations, where Rydberg states are not fully converged and less accurate. The resonance just below the 3p ionization edge at 1507 eV is attributed to the 3s to 8p transition, the resonance above the 3p-edge at 1529 eV to the 3s to 9p transition.
- For $26+$ in b) direct 3p photoionization is closed, but direct 3d photoionization is within the bandwidth. In the ground-state configuration 4s and higher orbitals are not occupied at Xe^{26+} , but valence-ionizations would be energetically possible for excited states, albeit with a much lower cross section than

resonant transitions. At photon energies lower than the 3d photoionization threshold at 1509 eV an abundance of resonances into Rydberg orbitals is present, which enables multi-step ionization processes in a wide range of photon energies. The 3p-7d transition at 1508 eV almost coincides with the 3d ionization edge. Above the 3d-edge the 3s to 6p transition appears as isolated resonance at 1521 eV.

- Finally, for Xe^{31+} in c) no direct inner-shell photoionization is in reach. Still, however, further ionization is possible through Auger decay following three strong resonances from 3p and 3d to the $n = 5$ and $n = 6$ shells.

The bandwidth-convolved absorption cross sections including direct and resonant channels for all charge states between 21+ and 35+ are depicted in figure 4.19. Here, the individual shapes of the curves are less important than the fact that there is a significant photoabsorption cross section for *all* of these consecutive charge states because of the resonances within the broad bandwidth. Only for 35+ the cross section appears rather small on this scale (about 0.03 Mb at 1.5 keV photon energy).

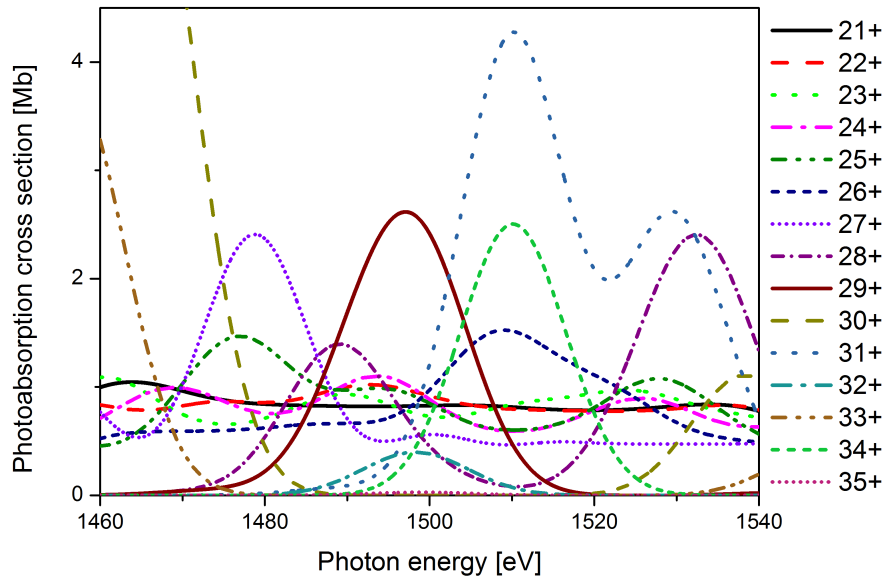


Figure 4.19 – Calculated photoabsorption cross sections around 1.5 keV photon energy for Xe^{21+} up to Xe^{35+} . Resonances are calculated from the ground-state configuration only and are convolved with a 15 eV bandwidth of the X-ray beam.

As indicated in the pathway sketch (figure 4.16), more than one resonant excitation may occur before the excited state relaxes via Auger decay. In this way, multiple resonances create highly excited states, where not only one, but several Auger decays may follow. Charge states without resonances within the 15 eV bandwidth of the photon energy may then not necessarily stop the ionization process, but may appear only in multi-excited electron configuration during the charge-up and, thus, might be simply "ran over" by consecutive Auger decays.

Chapter 5

Summary and Outlook

Multiphoton ionization in intense laser fields in the infrared, optical and ultraviolet spectral ranges has revolutionized the understanding of strong-field light-matter interaction and paved the way for various spectroscopic applications [26–28, 36]. The advent of free-electron lasers allowed investigating multiphoton ionization by intense laser radiation at photon energies reaching even beyond the ultraviolet regime, where photoionization pathways are fundamentally different from the strong-field effects observed with optical lasers. In the VUV and XUV spectral range of FLASH, measurements have been performed on light atoms, such as helium, neon and argon [170, 171], where significant contributions of non-sequential, direct two-photon photoionization pathways were found. For heavy atoms such as xenon, non-sequential, direct ionization by up to seven photons was discussed to explain the experimental spectra with charge states up to Xe^{21+} [29–31, 159, 160]. At X-ray energies, a light atom, neon [19, 20], has been studied in detail so far, but only negligible contributions from direct multiphoton photoionization were found in this case [20, 24, 25]. For heavier elements, the question arose if similarly high charge states as at FLASH may occur even though direct multiphoton ionization is much weaker at X-ray energies.

To answer this question, two heavy elements, xenon and krypton, have been investigated at the first X-ray free-electron laser operated world-wide, the LCLS. In a pioneering measurement in 2009, surprisingly high charge states were found for xenon irradiated with 1.5 keV photon energy. Simultaneously recorded fluorescence spectra showed a sudden increase of the fluorescence yield when highly charged ionic states were created. In order to quantify the charge-state distribution under

improved conditions, ion time-of-flight spectra were measured in 2011 with higher resolution and for a more comprehensive set of experimental parameters: The photon energy was set to 1.5 keV and 2 keV, the pulse energy varied by five different gas attenuator pressures and two pulse lengths could be compared. Additionally to the xenon data, photoionization of krypton was measured.

Confirming the previous findings of 2009, a maximum charge state of Xe^{36+} was observed at 1.5 keV photon energy or 0.83 nm wavelength, respectively, and $6.3 \times 10^{16} \text{ W/cm}^2$ intensity. This maximum charge state compares to previous measurements at other energies and intensities as follows: In strong laser fields (1.55 eV photon energy or 800 nm wavelength and peak intensities up to 10^{18} W/cm^2), the highest observed charge state so far is Xe^{20+} [172]; at FLASH (93 eV photon energy or 13.3 nm wavelength and an irradiance level up to 10^{16} W/cm^2), charge states up to Xe^{21+} have been reported [31]; and ionization by fast heavy-ion impact (highly charged uranium, U^{75+} , with 15.4 MeV/u kinetic energy) was demonstrated to yield charge states up to Xe^{35+} [173]. The charge state reported here thus represents the highest ever observed for an individual atom exposed to a single pulsed electromagnetic radiation.

For photoionization at 1.5 keV photon energy, a charge state of Xe^{36+} is unexpected on the basis of previous theoretical models. Considering *sequential* direct single-photon single-electron ionizations only, a maximum charge state of Xe^{26+} is anticipated, where the binding energy of 3d electrons increases to 1509 eV, thus exceeding the available photon energy. In contrast to the reported photoionization data on neon [19], sequential direct single-photon ionization alone can thus not explain at all the ionization process and additional pathways above Xe^{26+} have to be considered.

Simultaneously measured fluorescence spectra show decay from higher states into 3d and 3p vacancies for charge states where direct photoionization of these orbitals is already energetically closed. If direct photoionization is closed, inner-shell vacancies can only be created by resonant excitation. Such a resonance has been discussed in neon for one single charge state, the special case of K-shell excited Ne^{7+*} , where the electron excited to the 5p valence orbital may be photoionized before it is emitted in an Auger decay filling up the K-shell hole [20, 25]. In general, however, resonances are rare for light atoms at X-ray energies and unimportant at photon energies far above all absorption edges [19].

Theoretical analysis by Son and Santra of resonances and their cross sections for xenon reveal an abundance of resonant states accessible at 1.5 keV photon energy for charge states between 20+ and 36+. Hence, even beyond the limit for direct photoionization of Xe^{26+} , further ionization is enabled by densely spaced resonances, which can be excited within a single broadband FEL pulse for several subsequent high charge states created during the ionization process. The ionization of outer valence and Rydberg states after multiple resonant excitation of several electrons predominantly proceeds through Auger decays. While resonances in the optical multiphoton regime can enhance non-sequential direct multiphoton ionization, a direct photoionization of a resonantly excited state is negligible in the X-ray regime due to a very small photoionization cross section for Rydberg and outer valence states.

In contrast to the 1.5 keV case, photoionization at 2 keV photon energy but otherwise the same experimental parameters only proceeds up to Xe^{32+} , where the ground-state ionization energy exceeds the photon energy. This qualitatively different behavior is due to the fact that at higher photon energy suitable resonances appear at higher charge states, which are not reached effectively within a single shot for pulse intensities used in the experiment.

Krypton at 2 keV photon energy illustrates another example of resonant excitation during X-ray photoionization of heavy atoms. Here, photoionization starts with direct single-photon ionization of the L-shell electrons. However, the binding energy of the 2s state exceeds the available photon energy at a charge state of 9+ and direct 2p photoionization closes at 12+ already. At this charge state, 14 electrons in the M-shell are left which are energetically accessible by the photon energy but the cross section for M-shell photoionization is very small. Instead, further ionization proceeds through the resonant excitation of L-shell electrons and subsequent Auger decay into L-shell vacancies. At Kr^{20+} , the energy difference between 2p and 4s states exceeds the available photon energy of 2 keV and resonant excitation ends. Auger decay may remove another electron of excited Kr^{20+} resulting in a maximum charge state of 21+, exactly as recorded in the experimental krypton charge-state distribution.

In the comparison of krypton time-of-flight spectra and ion yield curves for 3 fs and 80 fs pulse lengths (at the same pulse energy), no significant difference was found. At relatively low pulse energy, the shorter pulse length apparently does

not sufficiently increases the intensity to cause direct two-photon ionization or to saturate resonances. For neon [19] and nitrogen [21], X-ray induced transparency was reported for intense, short X-ray pulses. It occurs when the Auger decay time is longer than the inverse photoionization rate and inner shell holes are not refilled by Auger decay during the X-ray pulse, such that the photoabsorption is drastically decreased. For krypton, no X-ray induced transparency was observed, probably because of the ultra-short of Auger decay times (< 1 fs) and the greater number of electrons available for photoionization.

The sudden increase of multiple photoionization for heavy atoms at high charge states and in certain photon-energy ranges is predicted to appear for all systems containing high-Z constituents. For imaging experiments, resonance-enhanced photoionization should be avoided as increased radiation damage in the vicinity of heavy atoms may appear. On the other hand, this highly efficient ionization process may be used to efficiently create highly excited, dense plasmas of high-Z atoms. The strength of resonance-enhanced multiphoton ionization can be varied by the FEL pulse energy, photon energy, and bandwidth.

In this work, the fundamental principle of resonance-enabled X-ray multiphoton ionization (REXMI) has been demonstrated. Now, a designated experiment to quantitatively investigate this photoionization pathway under newly available even higher peak intensities and for higher photon energies is the next logical step.

With imaging experiments taking advantage of the recently commissioned 100 nm focus at high photon energies (4 to 10 keV) at the coherent X-ray imaging (CXI) beamline at LCLS, an investigation of the REXMI mechanism at these parameters is most desirable. At 6 keV photon energy, for example, the xenon L-shell is accessible for direct photoionization, but closes at Xe^{30+} . At a peak intensity of 10^{22} W/cm² (assuming 3 mJ pulse energy, 3 fs pulse length and $0.01\mu\text{m}^2$ focus size), however, further ionization via the REXMI mechanism is expected to boost charge states up to Xe^{45+} (see figure 5.1). A measurement under these experimental conditions will clarify if the REXMI region can be reached with the increased intensity of the 100 nm focus but at reduced photoionization cross sections at high photon energies, and thus if resonance-enhanced ionization plays a role in radiation damage at experimental parameters typical for many imaging experiments.

For the experimental setup, minor changes are suggested. The pnCCDs should be placed facing downstream or perpendicular to the beam to avoid direct exposure to

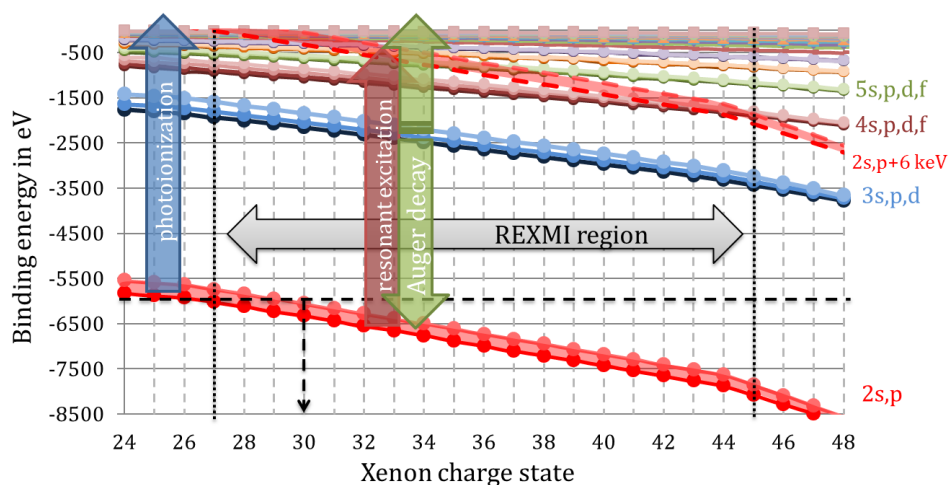


Figure 5.1 – Xenon binding energy as a function of the ionization level calculated with the Hartree-Fock method. The crossing of the dashed red lines with the outer orbitals labeled "2s,p+6 keV" marks the possible occurrence of resonances from 2s and 2p states at 6 keV photon energy.

stray light from the beamline. In this geometry and at the closest possible distance to the interaction zone allowed by the ion spectrometer, 59 mm, a pair of pnCCDs will cover a solid angle of 1.21 sr compared to 0.37 sr achieved in the setup discussed in this work. The ion spectrometer has to be operated at low extraction voltage to gain sufficient time-of-flight resolution for highly charged states. To investigate the influence of volume averaging on the final charge state distribution, one side of the double-sided ion spectrometer should be equipped with a narrow slit aperture limiting the detector acceptance in order to suppress signal generated outside the focus. Machine data has to be continuously recorded to account for FEL fluctuations. Furthermore, the LCLS GMD has to be calibrated for each scan of the pulse energy. Preferably, the GMD is continuously cross-calibrated by a second intensity monitor.

In this thesis, it has been demonstrated that resonant bound-bound transitions at high charge states lead to multielectron excitation. Accompanied by autoionization processes, these resonances drastically *enhance* the overall photoionization, even in regimes where direct inner-shell photoionization is still possible, and *enable* further photoionization steps, when direct photoionization is closed. This is a novel photoionization pathway unique to the X-ray regime and should be considered for X-ray scattering and absorption experiments at high intensity light sources, where heavy elements are probed.

Appendix A

Appendix to the Experimental Setup

A.1 Free-Electron Laser

A.1.1 Microbunching and SASE

Microbunching is based on the ponderomotive force which the light field exerts on the electrons. It is dependent on the phase difference between the sinusoidal electron trajectory and the oscillating light-field. The light field at frequencies ω_l and wavevector k_l can be assumed as plane x -polarized electromagnetic wave co-propagating in z with the relativistic electron beam

$$E_x(z, t) = E_0 \cos(k_l z - \omega_l t + \psi_0) \quad \text{with } k_l = \omega_l/c = 2\pi/\lambda_l \quad (\text{A.1})$$

The phase shift ψ_0 against the individual electron trajectory accounts for the various possible positions of an arbitrary electron within the bunch and will be discussed below. Whether the electron gains or loses energy in this field is described by the time derivative of the electron energy W

$$\frac{dW}{dt} = \vec{v} \cdot \vec{F} = -e \cdot v_x(t) E_x(t) \quad (\text{A.2})$$

With $dW/dt < 0$, the electron bunch loses energy and, obeying energy conservation, the light wave gains energy. This is the case when both vectorial factors in the scalar product point in the same direction.

Inserting the electric field (equation A.1), into the time derivative (equation A.2) and assuming for the sinusoidal motion of the electrons inside the undulators $v_x =$

$\frac{cK}{\gamma} \cos(k_u z)$, the following expression is derived

$$\begin{aligned}
\frac{dW}{dt} &= \vec{v} \cdot \vec{F} = -e \cdot v_x(t) E_x(t) = -e \frac{cK}{\gamma} \cos(k_u z) E_0 \cos(k_l z - \omega_l t + \psi_0) \\
&= -\frac{ecK E_0}{2\gamma} [\cos((k_l + k_u)z - \omega_l t + \psi_0) + \cos((k_l - k_u)z - \omega_l t + \psi_0)] \\
&= -\frac{ecK E_0}{2\gamma} [\cos(\psi) - \cos(\chi)]
\end{aligned} \tag{A.3}$$

where $\psi = (k_l + k_u)z - \omega_l t + \psi_0$ is called the *ponderomotive phase*; the fast oscillating term χ cancels out. The maximum energy transfer from the electron beam to the light wave is hence given when $\psi = \pm n2\pi$. The energy transfer is continuous over the entire undulator length when ψ is constant, which is only fulfilled at a certain wavelength. Inserting the trajectory equation for z into the condition $d\psi/dt = 0$, this wavelength turns out to be undulator specific wavelength at $\theta = 0$ (equation 3.3). So the spontaneous radiation in an undulator is indeed suitable to *seed* the SASE process.

With this distinct value of the ponderomotive phase ψ , a longitudinal coordinate inside the bunch is defined

$$\zeta = \frac{\psi + \pi/2}{k_l + k_u} \approx \frac{\psi + \pi/2}{2\pi} \lambda_l \tag{A.4}$$

where $\zeta_0(\psi_0 = -\pi/2) = 0$ sets the origin of coordinates at the phase of no energy exchange between electron and light wave.

With the initial bunch-internal coordinate ζ , and the ponderomotive phase ψ_0 at the time of entrance to the undulator and equation A.3 for the energy transfer between the electron beam and the light wave, three cases can be distinguished as seen in figure A.1: at $\psi_0 = \pi/2$ no energy is transferred between electron and light wave, for $\psi_0 < \pi/2$ the electron loses energy to the field, and for $\pi/2 < \psi_0 < \pi$ it gains energy from the field.

With an initial homogeneous distribution for ζ and ψ_0 in the electron bunch, the energy transfer between the electron beam and the light wave results in microbunching: Electrons with $\zeta > \zeta_0$ lose energy to the field due to $\psi_0 < \pi/2$, so the longitudinal velocity decreases, while their transversal amplitude ($\propto 1/\gamma$) increases; for electrons with $\zeta < \zeta_0$ vice versa. For both cases the absolute value of ζ and ψ_0 decrease, hence the electrons converge to similar values of ζ and ψ_0 . As the electron density is confined on a pulse length smaller than the wavelength, the radiation becomes coherent. Thus, not only the intensity but the amplitude of the light fields

is added. With ongoing microbunching the radiated power of coherently radiating microbunches increases exponentially along the undulator length.

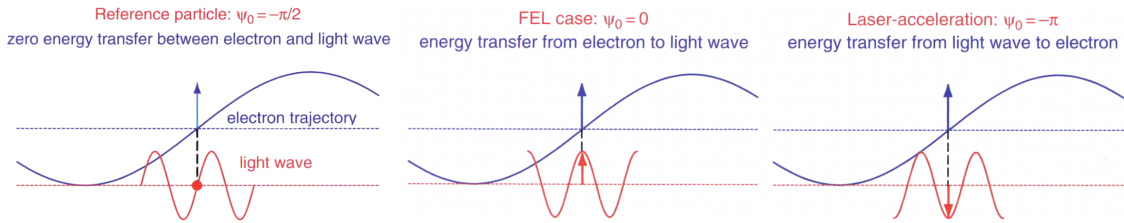


Figure A.1 – Energy exchange between electron and light wave¹

However, lasing becomes saturated when further microbunching is hindered by the internal Coulomb repulsion in the electron bunch, and when the electron energy falls below critical energy required for constructive interference in the undulator equation (equation 3.3). The region where increasing microbunching leads to an exponential growth in the radiated power is called linear regime, in contrast to the saturated regime where additional undulator length does not result in a higher radiated power.

In summary, an electron beam with high peak current, small energy spread and low emittance is sub-structured into microbunches due to electron-light-field interactions in a long undulator. As a result, the electrons radiate in phase, and thus the radiated power increases not only linearly with the number of radiating electrons (as for synchrotrons, see figure 3.4) but quadratically, which gives an enhancement of about nine orders of magnitude.

A.1.2 Seeding and Resonators

The SASE process starts up from spontaneous emission, which is generated stochastically by the in space and time randomly distributed electron density of the electron beam. Each of these density fluctuations may radiate spontaneously and seed a SASE process within the undulator bandwidth, where the wavelength fulfills the resonance condition. Ultimately, the resulting radiation pulse consists of a large number of independent wavepackets, which give rise to random and uncontrollable *spikes* in the radiated temporal profile and frequency-domain spectra. Within one

¹Source: P. Schmüser et al. Ultraviolet and Soft X-Ray Free-Electron Lasers, Springer-Verlag, 2010, Copyright (2010) by Springer-Verlag GmbH

wavepacket, the radiation is transversely and longitudinally coherent, but the overall temporal coherence is smaller than anticipated from the electron bunch length [174] (see section A.1.3). To make the SASE-FEL pulses fully coherent and free from coherence and intensity spikes, several seeding schemes have been proposed, where SASE is not seeded by stochastically spontaneous emission, but an external temporally well defined and coherent light pulse. Optical lasers are best accessible, however, limited in the available wavelength. With high harmonic generation, FEL have been seeded at deep UV [175], and recently pushed to the XUV-region [176]. With HHG a technical issue comes up: the high-harmonic seed light has to surpass the initial power level of the spontaneous radiation in the SASE-FEL. A second approach is to build a multi-segment FEL, where the fundamental or the higher harmonics (high-gain high harmonics HGHG) of the first undulator segment is used to seed the SASE-process in the undulators downstream [177]. Both HGHG and HHG schemes are planned for the XUV-FEL update FLASH 2 currently under construction.

In contrast to high-gain, single-pass FEL-amplifier a good pulse-to-pulse stability and temporal coherence is achieved in FEL-oscillator, where the FEL-light oscillates in a resonator. In fact the first free-electron laser [178] and succeeding FELs at long wavelength were equipped with an optical resonator, where infrared or microwave light was amplified with low-gain in an undulator embraced by a pair of mirrors and with a circulating electron beam passing numerous times [78]. A summary of various FEL concepts of free-electron lasers can be found in reference [179], "*Free-electron lasers: Present status and future challenges*".

A.1.3 Determination of the X-Ray Pulse Length

Among one of the first user runs at LCLS, L. Young and coworkers investigated the photoionization of neon at various photon energies [19]. The K-shell ionization potential of neon is 870 eV. Above that energy, at 1050 eV and 2000 eV photon energy, and with a fluence of about $200 \mu\text{J}/\mu\text{m}^2$, double core hole formation was observed in electron spectra. Double core holes are created when the Auger lifetime exceeds the inverse photoionization rate, in other words, the average time until the next photoionization event at given beam parameters. For singly charged neon the Auger decay into a 1s vacancy takes place at 2.4 fs time scale [180], but the Auger lifetime is rapidly increased during the ionization process; at Ne^{7+} , for instance, it already

amounts to 23 fs. The Auger lifetime for double core holes is significantly shorter. Due to the impact of Auger lifetimes on observable photoionization processes, the "Auger clock" is a reasonable approach to estimate the X-ray pulse duration.

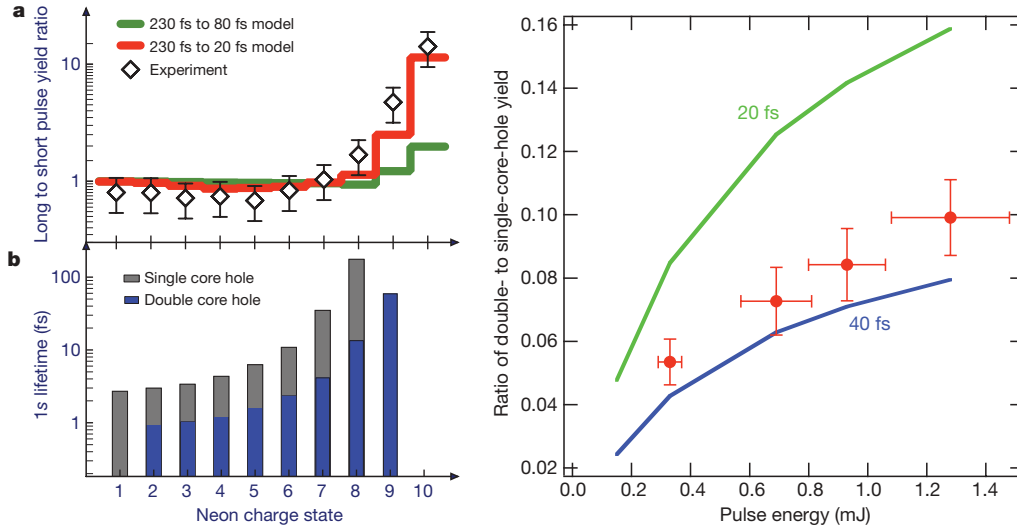


Figure A.2 – LCLS X-ray pulse length determination via double core hole creation¹. On the left the ratio of charge-state yield for 230-fs to 80-fs electron bunch durations is depicted in (a) (data points and simulation in solid lines at 2 keV, 2.0 mJ X-ray pulses) and the lifetimes of single and double core hole states as function of neon charge state in (b) (derived from [181]). On the right the ratio of Auger electron yield into single as a function to the yield into double core-hole is shown for four pulse energies together with simulated ratios at 20 fs and 40 fs pulse duration.

The pulse length could independently be retrieved from the ion as well as from the electron spectra. The ion yield decreases when long-lived single or even double core holes occur, which effectively lower the probability for an additional photoabsorption. For 230 fs pulse length, such core holes can be refilled within the pulse duration, but at nominally 80 fs the pulse length is in the order of the Auger lifetimes and yields for the highest neon charge states are diminished. A comparison of the experimental and theoretical ratio of ion yields for 230 fs and 80 fs indicates that the nominally 80 fs pulse length has actually to be four times lower to explain the decreased yield for Ne^{8+} , Ne^{9+} and Ne^{10+} (see on the left in figure A.2).

This finding is confirmed by pulse length determination from electron spectra: single and double core hole vacancies can easily be differentiated, as Auger electrons

¹Source: L. Young et al., Nature 466, 56-61 (2010). Copyright by the Nature Publishing Group.

from transitions into double core holes are significantly shifted towards higher kinetic energies compared to those from decay into a single core hole. The ratio of double to single core holes is specific for a certain pulse energy and pulse length. In the calculation of this ratio, the radiative decay into core holes [182–184] has also be considered. Then, the calculated ratios are compared to ratios derived from the experimental Auger line intensities. Accordingly, the nominally 80 fs pulse duration is found to be 40 fs or even less (see on the right in figure A.2).

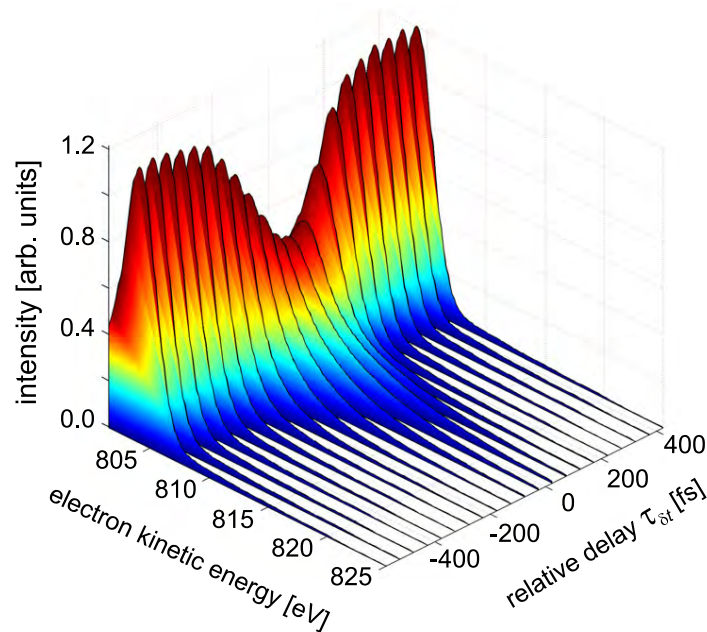


Figure A.3 – LCLS X-ray pulse length determination via sidebands in a two color set up¹. The neon Auger electron energy spectra are drawn as a function of the relative delay time (integrated in 50 fs steps) between the NIR (pulse length 100 fs) and the X-ray pulses (electron pulse length 75 fs). Around the relative zero point, the highest order of sidebands is observed.

Due to the high requirements on peak fluence for double core hole creation, and the small angular acceptance of electron time-of-flight spectrometer (0.007 sr), the above approach is impractical for shot-to-shot on-line diagnostics. By means of a magnetic bottle electron spectrometer with an angular acceptance of approximately 0.8 sr and a relatively large focus spot of 60 μm diameter, Düsterer et al. demonstrated a non-invasive technique to obtain the LCLS single shot pulse duration [89].

¹Source: S. Düsterer et al., New Journal of Physics 13, 093024 (2011). Copyright by the Institute of Physics

To retrieve the pulse duration from the electron spectrum, Auger electrons following X-ray inner shell ionization of neon were dressed with 100 fs long near-infrared laser pulses, where their momentum vector was either increased or decreased in interaction with the time-dependent laser field (due to the bandwidth of the incident X-ray beam, which is transferred on the photo-electron energy, the small additional momentum contribution cannot be resolved for photo electrons) . The number of *sidebands* in the electron kinetic energy spectrum, spaced by the photon energy of the NIR laser (1.55 eV, 800 nm), represent the number of absorbed optical photons; the better the temporal overlap of the X-ray pulse and peak intensity of the laser pulse is, the more sidebands are generated. Thus, in a scan of the delay between X-ray and optical laser, the number of sidebands reveals the X-ray pulse length [185]. At LCLS this two-color approach determined a pulse length (FWHM) of 120 fs for an electron bunch duration of 175 fs and 40 fs for nominally 75 fs long pulse, respectively (figure A.3).

The determination of pulse length via sideband measurements in a two-color setup is closely related to light field streaking cameras, which have become an established diagnosis tool for attosecond HHG sources [186] and XUV FELs [187].

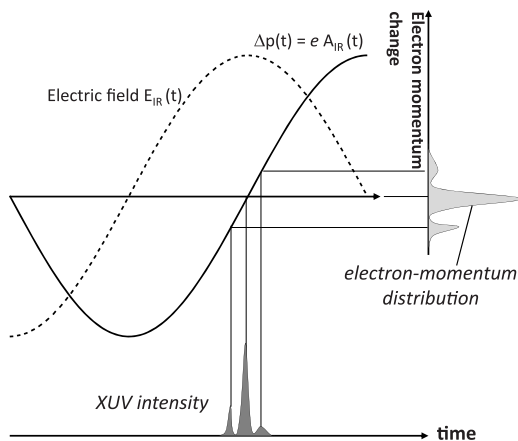


Figure A.4 – Pulse length determination by light-field streaking¹.

Here, the XUV or X-ray pulse photoionizes the target atom, where the temporal profile of the generated electron wavepacket resembles the photon pulse shape. Then, the electrons are accelerated by the electric field of the optical streak pulse. Their momentum change is given by the vector potential of the dressing field at the ionization time (figure A.4).

By a simultaneous measurement of the kinetic energy and angular distribution, the momenta can be recovered and the temporal profile of the ionizing pulse reconstructed. The main difference of the sideband and the streaking technique is

¹Source: U. Fröhling et al. Nature Photonics 3, 523-528 (2009). Copyright by the Institute of Physics

the frequency of the optical dressing laser: for sidebands a high frequency, i.e. high photon energy, is desirable to distinguish the number of absorbed photons. Owing to the optical *pulse duration* of several tenth of femtoseconds, the above sideband approach is limited to pulse lengths of >40 fs. In contrast the maximum detectable pulse length for light-field streaking cameras is governed by the *sub-cycle oscillation* of the laser electric field: the X-ray pulse length has to fit into a half single cycle of the dressing field to avoid ambiguity. So at 800 nm the longest pulse length measurable by streaking would be 1.4 fs, which is too small for the estimated pulse length. For short electron pulses at the LCLS, low bunch charge mode, light-field streaking has been applied with $2.4 \mu\text{m}$ wavelength, and the X-ray pulse length was found to be less than five femtoseconds long [90]. To determine longer pulse lengths with the streaking approach, the wavelength of the dressing laser has to be longer. At FLASH terahertz radiation, which is available from a dedicated THz undulator downstream of the XUV undulators (thus 9 ns delay to the XUV beam), was employed to determine the XUV pulse length to be 28 fs (FWHM) [188] and, recently, THz radiation (strong IR-laser light frequency converted by a Lithium Niobate (LiNbO₃) crystal), was used for light field streaking at LCLS as well [91].

Instead of an additional optical laser, the FEL-light can be split to investigate the pulse and coherence length in a two-beam *single-color* experiment. To date, such autocorrelation measurements have been limited to FELs operating up to the XUV region, where beam splitting and guiding optics are better available, but beam splitters for the X-ray region based on moveable grazing incidence split-mirrors are currently developed. Two classes of autocorrelation experiments, based on interferometer or pump-probe multiple-photon ionization, have been carried out at XUV-FELs: At FLASH, a beam splitter and delay stage were employed to determine the temporal (longitudinal) coherence length via interference patterns produced by overlapping both partial beams under a small angle and recorded on a XUV sensitive CCD-camera [92, 93]. Also at FLASH the temporal coherence and pulse length was investigated by means of intensity autocorrelation, where the ion yield from nonlinear processes occurring in atoms (two-photon double ionization of He [94, 95], and four-photon four-fold-ionization of N₂ [96]) indicate to which degree the two single-color beams are overlapping; the same technique was employed at SCSS observing the two-photon single ionization of He [97].

For synchrotron radiation, which is generated by spontaneous emission, the pulse

length information is delivered in spectral intensity correlations. Its spectrum, shaped by shot noise fluctuations, consists of spikes with widths inversely proportional to the bunch length [189]. An intensity interferometry has successfully been applied for pulse length determination of synchrotron radiation from a bending magnet [190] and from a wiggler [189]; the statistical temporal properties of a FEL operating in the self amplified spontaneous emission mode are similar to those of spontaneous emission, which can be described by a Gaussian process [79]. Consequently Hau-Riege et al. derived the pulse length from single shot spectra measured in the Soft X-ray (SXR) experimental station, which is equipped with a monochromator that can be used as spectrograph [116], and from an assumed pulse shape function. They found the photon pulse length to be 70 fs for 300 fs, 60 fs for 150 fs, and 40 fs for 70 fs electron bunch length, respectively [88?]. It should be mentioned, that, vice versa, the averaged spectral shape and the coherence time can be derived from the averaged pulse duration by the partial-coherence method [191]; with both, pulse duration and spectral data at hand, PCM helped to underpin the pulse length measurements at XUV-FELs [96, 97].

A.2 The CAMP endstation

A.2.1 A Multi-Purpose Endstation

Before the experimental setup of the CAMP endstation is discussed, a list of experiments performed so far should illustrate the "multi-purpose" as intended in the initial design:

- simultaneous ion and fluorescence spectra of rare gas atoms [192]
- coulomb explosion imaging of molecular fragmentation
- (time resolved) imaging and ion spectra of X-ray excited clusters
- coherent diffractive imaging of bio-samples [13–16]
- aerosol morphology [85]
- diffractive imaging of oriented molecules in the gas phase
- time-resolved photoelectron diffraction in laser-aligned molecules

- X-ray induced lattice and electron dynamics in graphite [88]

A.2.2 Vacuum System

Ultra high vacuum (UHV) is required for three reasons:

1. some technical devices require vacuum, e.g. the electron multipliers (MCP see below) require a vacuum of below 10^{-5} mbar to avoid sparking
2. photon and ion absorption and scattering should be minimized
3. the target to background signal should be maximized

Vacuum can be reached by a variety of pumping techniques, which classify into three classes: a positive displacement pump traps a fixed amount of air and displaces that trapped volume into the exhaust. They are used to pump from atmospheric pressure down to pre-vacuum (10^{-3} mbar). Pressurizing pumps work similarly by generating a pressure gradient but do not spatially enclose a volume. That is why they hardly work at atmospheric pressure. Turbo-molecular pumps, for instance, have open rotors, but due to the high rotation speed, a ultra high vacuum down to 10^{-9} mbar can be reached. Since gas can be absorbed on a surface, especially water, nitrogen and oxygen are easily trapped on the cold surface of a cryo-pump, which further improves an UHV. All three types of pumps were used in the discussed set-up.

A vacuum in the low 10^{-8} mbar region is required for any chamber connecting to the AMO beamline. Because this pressure could not be reached in the main experimental chamber of CAMP, differential pumping sections were placed between the main chamber and the beamline. In total, three differential pumping sections, separated by apertures of 5 mm diameter, were used to lower the pressure from at maximum 10^{-6} mbar in the main chamber to the low 10^{-8} mbar region. The pumping section was enclosed by two valves and a bellow between two of the sections allowed to move the main experimental chamber for alignment on the actual beam axis.

The vacuum was created by turbo-molecular pumps connected to the pre-vacuum of several roughing pumps. The main chamber was pumped by four turbo-molecular pumps each with a pumping speed of 700 l/s. The pnCCD detector require cryogenic cooling and expose a large cold area, thus they resemble a cryo-pump; a dedicated cryo-pump connected to a large copper surface was used as well. Because condensed

air might rapidly evaporated during warm up and the resulting over-pressure might pose a hazard to workers and equipment, burst discs which would relieve the pressure were mandatory.

The vacuum was monitored by several vacuum gauges and could be analyzed by a residual gas analyzer.

A.2.3 Estimating the Density and Temperature of the Gas Jet

The gas pressure, skimmer opening-diameter and $X_{1st\ skimmer}$ are the dominating parameters for the target density in the interaction zone. If all apertures and skimmers are aligned the pressure in the beam dump, which is a separated chamber to pump the gas jet after passing the main experimental chamber, should increase linearly with the gas pressure. From the pressure in the beam dump, p_{dump} , the target density, ρ , in the interaction zone can be estimated

$$\rho = \frac{N_A}{22.4} \cdot \frac{p_{dump} L_{dump}}{v \pi (d_{target})^2 / 4} \quad (\text{A.5})$$

Here N_A is the Avogadro constant and L_{dump} the pumping speed in the jet dump [193]. In contrast to the velocity of an ideal gas derived from the expansion-equation 3.9, the velocity v has to be corrected for the temperature T_{end} which was not transformed into kinetic energy

$$\frac{5}{2} N k_B T = \frac{1}{2} m \bar{v}^2 + \frac{5}{2} N k_B T_{end} \Rightarrow v = \sqrt{\frac{5 k_B}{m} (T - T_{end})} \quad (\text{A.6})$$

The temperature T_{end} can be derived from the *speed-ratio* S , the ratio between the averaged velocity v and the width of the velocity distribution, which is given by the thermic velocity [194]

$$S = \frac{v}{v_{therm}} = \frac{v}{\sqrt{2 k_B T_{end} / m}} = \sqrt{\frac{5}{2} \left(\frac{T_{end}}{T} \right)} \quad (\text{A.7})$$

The temperature then becomes $T_{end} = 2.5 T / S^2$. The speed-ratio is empirically determined for given gas pressure and aperture diameter, which can be found in tables (e.g. [195]). This relation not only helps to derive the target density, but also shows that the temperature T_{end} after expansion is proportional to the initial gas temperature. Hence, to decrease the internal target motion for a better momentum resolution in the interaction zone, the initial gas temperature should be lowered.

A.2.4 Multi Channel Plate (MCP)

The ion yield is undetectable small and thus has to be amplified to a measurable current. The amplifier has to resolve nanosecond-short timescales but also deliver the spatial information to the attached position resolving detector. So even though a simple electron multiplier provides sufficient time resolution, its spatial resolution capability is limited by its relative bulky size. A multi channel plate (MCP) can be considered as a dense array of thousands of micro-sized electron multiplier, resulting in a spatial resolution determined by their diameter and center-to-center spacing.

In a MCP these micro-sized electron multiplier are semiconductor channels biased with a voltage of about 1000 V between thin metal electrodes on both ends. The channels are tilted around 8 degree to normal to assure that ions will hit the channel walls and start a cascade of secondary electrons. The secondary emission process is fed by the bias current flowing through the channel resistance (approx. 30 M Ω) due to the voltage difference of front and back. As the secondary electrons are stripped from this current, a so called strip-current fills up the electron-holes. It can be measured as a positive pulse on the MCP.

A single plate yields 10^3 to 10^4 electrons, the common array of two plates in a chevron (v-like) shape has a gain of 10^7 .

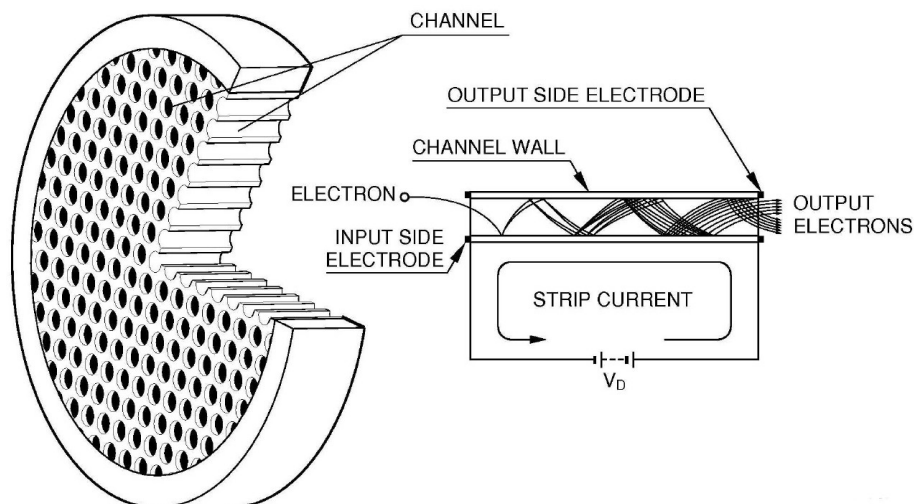


Figure A.5 – Sketch of a MCP and its working principle.¹

¹Source: http://sales.hamamatsu.com/assets/pdf/catsandguides/MCPassy_TMCP0001E08.pdf, Copyright by Hamamatsu Corporation.

The absolute detection efficiency, of a MCP is dependent on the impacting ion-mass and its kinetic energy [109]. To enhance the MCP detection efficiency the charged particles, which were accelerated in the electric field of the spectrometer, are additionally accelerated in the electric field between a highly transparent thin copper mesh and the MCP front-surface.

A.2.5 pn-Junction Charge Coupled Device (pnCCD)

There are many types of fluorescence detectors available, as a good reference, several of them can be found in an electron-beam ion trap (EBIT), which is dedicated to fluorescence spectroscopy of highly charged ions and has been employed at VUV and X-ray FELs, FLASH [196] and LCLS: MCPs, semiconductor (Germanium) detector, grazing incident spectrometer and calorimeter. All these devices have specific wavelength-dependent detection efficiencies and energy resolution. For instance, semiconductor detectors have broadband detection efficiency but a low resolution (the EBIT Germanium detector at LCLS¹ \approx FWHM 50 eV resolution), while grazing incident spectrometer have high resolution but are limited to a small energy region and tiny solid angle (for the EBIT spectrometer at LCLS 0.7 eV resolution, 60 eV working range). For CAMP, a large format semiconductor detector was used, a pn-junction charge coupled device (pnCCD) [127, 145]. The key idea of CAMP is to measure ion and electron spectra simultaneously with the fluorescence spectrum in each shot, so that a broadband large-solid-angle detection device was chosen instead of a high resolving one.

The pnCCDs were designed for satellite missions where a wide range of elements had to be identified by their $K\alpha$ lines between few hundreds of electronvolts to tenths of kilo-electronvolt [197]. Thus a broadband (100eV-25keV) optical to hard X-ray detector was required. This energy range and a high quantum efficiency of above 90% (>400 eV) could be achieved by a large sensitive depth making use of the full volume of the chip to the conversion of the incident X-rays into electron hole pairs.

The underlying technique is the sideways depletion of a pnp-structure [127, 145, 198]: in a 450 μm thick high resistivity (up to 6 $\text{k}\Omega/\text{cm}$) n-silicon-wafer with p+ contacts on both surfaces the pn junctions are reversely biased. The photo-effect

¹Combined with the monochromator at the SXR beamline, the Germanium detector could be used as counting detector. Then, the detector count rate during an energy scan by the monochromator gives high resolving and fast fluorescence spectrum.

transforms every 3.7 eV of the impinging X-ray energy into an electron-hole pair. With an extraction field of $0.5 \text{ V}/\mu\text{m}$, the holes drift to the p^+ -implanted back side, while the electrons drift within few nanoseconds to the potential minimum inside the n -type silicon (see potential-curve on the right in figure 3.14). The depth of this minimum is set by the voltage difference of pnCCD back (X-ray entrance) and front (electrical readout) side. With a negatively biased back side with respect to the front side, the voltage is here chosen to set the potential minimum $7 \mu\text{m}$ under the front side within an epitaxial layer¹ with lower resistivity ($40 \Omega/\text{cm}$). This distance is close enough for the electrons to experience a potential well formed by three transfer registers of two different voltage levels. Each potential well constitutes one pixel. After millisecond-long integration time, the pixel-wise collected electrons are transferred to the readout n^+ anode by a simultaneous change of neighboring register voltages. The benefit of the pnp-structure is that full depletion of the silicon bulk is achieved at a voltage four times lower than the voltage needed to deplete a simple diode of the same thickness. Hence the capacitance of the n^+ anode can be kept very small, which yields a superior signal to noise ratio. Each

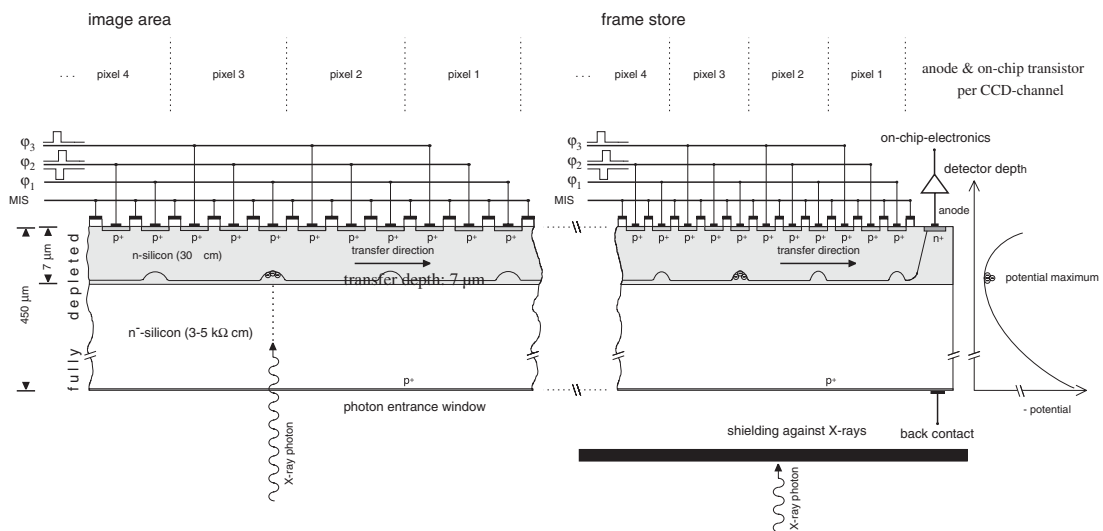


Figure A.6 – Schematic cross-section through a frame-store pnCCD channel. On the right: electric potential in the device vs. depth.² [199]

¹A crystalline overlayer grown on a crystalline substrate with a preferred orientation of the overlayer.

²Source: N. Meidinger et al. Nuclear Instruments and Methods in Physics Research Section A: Accelerators, Spectrometers, Detectors and Associated Equipment 565, 251-257 (2006). Copyright (2012) by Elsevier Ltd.

transfer channel depicted in figure 3.14 is coupled to its own on-chip integrated JFET readout amplifier, where the anode of the pnCCD line is connected to the p+ gate of the n-channel *junction gate field-effect transistor* (JFET) for signal amplification. The preamplified signal is then fed into a multichannel analog signal amplifier and processor (CAMEX) [200], which performs an eightfold sampling of the pixel-signal and the baseline to further improve the signal-to-noise ratio. It also offers to set one of 16 gain settings. Gain 1 is the maximum gain setting optimal for high resolution spectroscopy, in gain mode $1/2^n$ additional capacitors are used in the CAMEX chips so that the gain decreases but the dynamic range increases, which enables counting of scattered X-ray photons at high flux for best imaging. Up to this point, all channels are processed in parallel which ensures a high readout speed of up to 200 Hz. Eventually, each of the 16 CAMEX chips performs a multiplexing of all amplified and processed 128 channels to one data stream, which is rapidly (10 MHz) transferred to a 14-bit analog-digital converter and processed by the computer based data acquisition system. For X-ray FEL experiments with additional optical pump or alignment lasers, the pnCCD entrance window was coated with aluminum layer for suppression of optical light contamination; to avoid deposition of target-fragments, a thin foil (e.g. 3 μm polyimide) was used in front of the pnCCD surface [157]. Details on the actual running, read-out and analysis of the pnCCDs will be presented in section 3.3.3.

Bibliography

- [1] Röntgen, W. C. Über eine neue Art von Strahlen. *Annalen der Physik* **300**, 12–17 (1898). URL <http://doi.wiley.com/10.1002/andp.18983000103>.
- [2] Planck, M. Zur Theorie des Gesetzes der Energieverteilung im Normalspektrum. *Verhandlungen der Deutschen physikalischen Gesellschaft* **2**, 237 (1900). URL http://www.pro-physik.de/Phy/pdfs/Max_Planck_DPG-Verhandlungen1900.pdf.
- [3] Einstein, A. Über einen die Erzeugung und Verwandlung des Lichtes betreffenden heuristischen Gesichtspunkt. *Annalen der Physik* **322**, 132–148 (1905). URL <http://doi.wiley.com/10.1002/andp.19053220607>.
- [4] Göppert-Mayer, M. Über Elementarakte mit zwei Quantensprüngen. *Annalen der Physik* **401**, 273–294 (1931). URL <http://doi.wiley.com/10.1002/andp.19314010303>.
- [5] Voronov, G. S. & Delone, N. B. Ionization of the xenon atom by the electric field of ruby laser emission. *Journal of Experimental and Theoretical Physics (JETP) Letters* **1**, 66 (1965). URL http://www.jetpletters.ac.ru/ps/1590/article_24398.pdf.
- [6] Mould, R. F. The early history of x-ray diagnosis with emphasis on the contributions of physics 1895-1915. *Physics in medicine and biology* **40**, 1741–87 (1995). URL <http://www.ncbi.nlm.nih.gov/pubmed/8587931>.
- [7] Friedrich, W., Knipping, P. & Laue, M. Interferenzerscheinungen bei Röntgenstrahlen. *Annalen der Physik* **346**, 971–988 (1913). URL <http://doi.wiley.com/10.1002/andp.19133461004>.

- [8] Debye, P. & Scherrer, P. Interferenzen an regellos orientierten Teilchen im Röntgenlicht. I. *Physikalische Zeitschrift* **17**, 277 (1916). URL http://www.digizeitschriften.de/dms/img/?PPN=PPN266833020_0043&DMDID=dmdlog111#.
- [9] Bragg, W. L. The Analysis of Crystals by the X-ray Spectrometer. *Proceedings of the Royal Society A: Mathematical, Physical and Engineering Sciences* **89**, 468–489 (1914). URL <http://rspa.royalsocietypublishing.org/cgi/doi/10.1098/rspa.1914.0015>.
- [10] Watson, J. D. & Crick, F. H. C. Molecular Structure of Nucleic Acids: A Structure for Deoxyribose Nucleic Acid. *Nature* **171**, 737–738 (1953). URL <http://www.nature.com/doifinder/10.1038/171737a0>.
- [11] Wille, K. Synchrotron radiation sources. *Reports on Progress in Physics* **54**, 1005–1067 (1991). URL <http://stacks.iop.org/0034-4885/54/i=8/a=001?key=crossref.dc03c82e1b56b9fdb2795980da480ecb>.
- [12] Neutze, R., Wouts, R., van der Spoel, D., Weckert, E. & Hajdu, J. Potential for biomolecular imaging with femtosecond X-ray pulses. *Nature* **406**, 752–757 (2000). URL <http://www.ncbi.nlm.nih.gov/pubmed/10963603>.
- [13] Chapman, H. N. *et al.* Femtosecond X-ray protein nanocrystallography. *Nature* **470**, 73–77 (2011). URL <http://www.nature.com/doifinder/10.1038/nature09750>.
- [14] Seibert, M. M. *et al.* Single mimivirus particles intercepted and imaged with an X-ray laser. *Nature* **470**, 78–81 (2011). URL <http://www.nature.com/doifinder/10.1038/nature09748>.
- [15] Barty, A. *et al.* Self-terminating diffraction gates femtosecond X-ray nanocrystallography measurements. *Nature Photonics* **6**, 35–40 (2011). URL <http://www.nature.com/doifinder/10.1038/nphoton.2011.297>.
- [16] Lomb, L. *et al.* Radiation damage in protein serial femtosecond crystallography using an x-ray free-electron laser. *Physical Review B* **84**, 214111 (2011). URL <http://link.aps.org/doi/10.1103/PhysRevB.84.214111>.

- [17] Yoon, C. H. *et al.* Unsupervised classification of single-particle X-ray diffraction snapshots by spectral clustering. *Optics Express* **19**, 16542 (2011). URL <http://www.opticsinfobase.org/abstract.cfm?URI=oe-19-17-16542>.
- [18] Spence, J. C. H. *et al.* Phasing of coherent femtosecond X-ray diffraction from size-varying nanocrystals. *Optics Express* **19**, 2866 (2011). URL <http://www.ncbi.nlm.nih.gov/pubmed/22254364><http://www.opticsinfobase.org/abstract.cfm?URI=oe-19-4-2866>.
- [19] Young, L. *et al.* Femtosecond electronic response of atoms to ultra-intense X-rays. *Nature* **466**, 56–61 (2010). URL <http://www.nature.com/doifinder/10.1038/nature09177>.
- [20] Doumy, G. *et al.* Nonlinear Atomic Response to Intense Ultrashort X Rays. *Physical Review Letters* **106**, 083002 (2011). URL <http://link.aps.org/doi/10.1103/PhysRevLett.106.083002>.
- [21] Hoener, M. *et al.* Ultraintense X-Ray Induced Ionization, Dissociation, and Frustrated Absorption in Molecular Nitrogen. *Physical Review Letters* **104**, 253002 (2010). URL <http://link.aps.org/doi/10.1103/PhysRevLett.104.253002>.
- [22] Fang, L. *et al.* Double Core-Hole Production in N₂: Beating the Auger Clock. *Physical Review Letters* **105**, 083005 (2010). URL <http://link.aps.org/doi/10.1103/PhysRevLett.105.083005>.
- [23] Cryan, J. *et al.* Auger Electron Angular Distribution of Double Core-Hole States in the Molecular Reference Frame. *Physical Review Letters* **105**, 083004 (2010). URL <http://link.aps.org/doi/10.1103/PhysRevLett.105.083004>.
- [24] Rohringer, N. & Santra, R. X-ray nonlinear optical processes using a self-amplified spontaneous emission free-electron laser. *Physical Review A* **76**, 33416 (2007). URL <http://link.aps.org/doi/10.1103/PhysRevA.76.033416>.
- [25] Sytcheva, A., Pabst, S., Son, S.-K. & Santra, R. Enhanced nonlinear response of Ne⁸⁺ to intense ultrafast x rays. *Phys. Rev. A* **85**, 023414 (2012). URL <http://link.aps.org/doi/10.1103/PhysRevA.85.023414>.

- [26] Popov, V. S. Tunnel and multiphoton ionization of atoms and ions in a strong laser field (Keldysh theory). *Physics-Uspekhi* **47**, 855–885 (2004). URL <http://stacks.iop.org/1063-7869/47/i=9/a=R01?key=crossref.fada7a3507c3603112cd8e21ec3d4bfa>.
- [27] Protopapas, M., Keitel, C. H. & Knight, P. L. Atomic physics with super-high intensity lasers. *Reports on Progress in Physics* **60**, 389–486 (1997). URL <http://stacks.iop.org/0034-4885/60/i=4/a=001?key=crossref.c9efe8743561c1b53a515c06c2e13ca2>.
- [28] Pukhov, A. Strong field interaction of laser radiation. *Reports on Progress in Physics* **66**, 47–101 (2003). URL <http://stacks.iop.org/0034-4885/66/i=1/a=202?key=crossref.1b193efe576fde5e6213c8a057c9d7cc>.
- [29] Wabnitz, H. *et al.* Multiple ionization of atom clusters by intense soft X-rays from a free-electron laser. *Nature* **420**, 482–485 (2002). URL <http://www.ncbi.nlm.nih.gov/pubmed/12466837>.
- [30] Wabnitz, H. *et al.* Multiple Ionization of Rare Gas Atoms Irradiated with Intense VUV Radiation. *Physical Review Letters* **94**, 023001 (2005). URL <http://link.aps.org/doi/10.1103/PhysRevLett.94.023001>.
- [31] Sorokin, A. *et al.* Photoelectric Effect at Ultrahigh Intensities. *Physical Review Letters* **99**, 213002 (2007). URL <http://link.aps.org/doi/10.1103/PhysRevLett.99.213002>.
- [32] McQuarrie, D. A. & Simon, J. D. *Physical Chemistry: A Molecular Approach* (University Science Books, 1997).
- [33] Hartree, D. R. The Wave Mechanics of an Atom with a Non-Coulomb Central Field. Part I. Theory and Methods. *Mathematical Proceedings of the Cambridge Philosophical Society* **24**, 89 (1928). URL http://www.journals.cambridge.org/abstract_S0305004100011919.
- [34] Slater, J. Atomic Shielding Constants. *Physical Review* **36**, 57–64 (1930). URL <http://link.aps.org/doi/10.1103/PhysRev.36.57>.
- [35] Ionization in the field of a strong electromagnetic wave **20**.

- [36] Mainfray, G. & Manus, G. Multiphoton ionization of atoms. *Reports on Progress in Physics* **54**, 1333–1372 (1991). URL <http://stacks.iop.org/0034-4885/54/i=10/a=002?key=crossref.507d1cbda7374fd8b812a25fada68d50>.
- [37] Wachter, A. & Hoerber, H. *Repetitorium Theoretische Physik (Springer-Lehrbuch) (German Edition)* (Springer, 2004).
- [38] Santra, R. Concepts in x-ray physics. *Journal of Physics B: Atomic, Molecular and Optical Physics* **42**, 169801–169801 (2009). URL <http://stacks.iop.org/0953-4075/42/i=16/a=169801?key=crossref.a7edd4b39b6d4d45e87dbb9828e62974>.
- [39] Fitzpatrick, R. Quantum Mechanics: A graduate level course. lecture notes (2006). URL <http://farside.ph.utexas.edu/teaching/qm/lectures/node64.html>.
- [40] Demtröder, W. *Experimentalphysik 3: Atome, Moleküle und Festkörper*. Springer-Lehrbuch (Springer, 2010).
- [41] Atkins, P. & De Paula, J. *Physical Chemistry* (Oxford University Press, 2006).
- [42] Attwood, D. *Soft X-Rays and Extreme Ultraviolet Radiation: Principles and Applications* (Cambridge University Press, 2007).
- [43] Bransden, B. & Joachain, C. *Physics of Atoms and Molecules* (Longman Pub Group, 1982).
- [44] Ueda, K. High-resolution inner-shell spectroscopies of free atoms and molecules using soft-x-ray beamlines at the third-generation synchrotron radiation sources. *Journal of Physics B: Atomic, Molecular and Optical Physics* **36**, R1–R47 (2003). URL <http://stacks.iop.org/0953-4075/36/i=4/a=201?key=crossref.b5a4184768088be9d12aa743766aa6ff>.
- [45] Southworth, S. *et al.* Double K-shell photoionization of neon. *Physical Review A* **67**, 062712 (2003). URL <http://link.aps.org/doi/10.1103/PhysRevA.67.062712>.
- [46] Falta, J. & Möller, T. *Forschung mit Synchrotronstrahlung* (Vieweg-Teubner Verlag, 2010).

-
- [47] Saito, N. & Suzuki, I. H. Shake-off processes in photoionization and Auger transition for rare gases irradiated by soft X-rays. *Physica Scripta* **49**, 80–85 (1994). URL <http://stacks.iop.org/1402-4896/49/i=1/a=011?key=crossref.acb488c749234dd3471c71aa9c2dde74>.
- [48] Kochur, a. & Popov, V. Shake up and shake off probabilities for L-, M-, and N-electrons in atoms with $Z=3$ to 60. *Radiation Physics and Chemistry* **75**, 1525–1528 (2006). URL <http://linkinghub.elsevier.com/retrieve/pii/S0969806X06002118>.
- [49] Armen, G. B., Aksela, H., Å berg, T. & Aksela, S. The resonant Auger effect. *Journal of Physics B: Atomic, Molecular and Optical Physics* **33**, R49–R92 (2000). URL <http://stacks.iop.org/0953-4075/33/i=2/a=201?key=crossref.561d62f0e75c83051582880d63fd3c97>.
- [50] Bambynek, W. *et al.* X-Ray Fluorescence Yields, Auger, and Coster-Kronig Transition Probabilities. *Reviews of Modern Physics* **44**, 716–813 (1972). URL <http://link.aps.org/doi/10.1103/RevModPhys.44.716>.
- [51] Kurka, M. *Zwei-Photonen-Doppelionisation von Helium und D₂-Molekülen am Freie-Elektronen-Laser in Hamburg*. Ph.D. thesis, Ruprecht-Karls Universität, Heidelberg (2011). URL http://archiv.ub.uni-heidelberg.de/volltextserver/volltexte/2011/12345/pdf/PhD_Kurka.pdf.
- [52] Freeman, R. *et al.* Above-threshold ionization with subpicosecond laser pulses. *Physical Review Letters* **59**, 1092–1095 (1987). URL <http://link.aps.org/doi/10.1103/PhysRevLett.59.1092>.
- [53] Milošević, D. B., Paulus, G. G., Bauer, D. & Becker, W. Above-threshold ionization by few-cycle pulses. *Journal of Physics B: Atomic, Molecular and Optical Physics* **39**, R203–R262 (2006). URL <http://stacks.iop.org/0953-4075/39/i=14/a=R01?key=crossref.212b8163f018982d1c4d95988bf902ce>.
- [54] Dai, B.-N. & Lambropoulos, P. Selective ionization: Effects of power broadening, laser bandwidth, and interaction time on selectivity. *Physical Review A* **34**, 3954–3961 (1986). URL <http://link.aps.org/doi/10.1103/PhysRevA.34.3954>.
-

- [55] Johnson, P. M. Molecular multiphoton ionization spectroscopy. *Accounts of Chemical Research* **13**, 20–26 (1980). URL <http://www.ncbi.nlm.nih.gov/pubmed/20234716><http://pubs.acs.org/doi/abs/10.1021/ar50145a004>.
- [56] Johnson, P. M. & Otis, C. E. Molecular Multiphoton Spectroscopy with Ionization Detection. *Annual Review of Physical Chemistry* **32**, 139–157 (1981). URL <http://www.annualreviews.org/doi/abs/10.1146/annurev.pc.32.100181.001035>.
- [57] Faisal, F. H. M. Multiple absorption of laser photons by atoms. *Journal of Physics B: Atomic and Molecular Physics* **6**, L89–L92 (1973). URL <http://stacks.iop.org/0022-3700/6/i=4/a=011?key=crossref.e8106b936b6411a7642e20c2bf95dbe7>.
- [58] Reiss, H. Effect of an intense electromagnetic field on a weakly bound system. *Physical Review A* **22**, 1786–1813 (1980). URL <http://link.aps.org/doi/10.1103/PhysRevA.22.1786>.
- [59] Corkum, P. Plasma perspective on strong field multiphoton ionization. *Physical Review Letters* **71**, 1994–1997 (1993). URL <http://link.aps.org/doi/10.1103/PhysRevLett.71.1994>.
- [60] Lewenstein, M., Balcou, P., Ivanov, M., L Huillier, A. & Corkum, P. Theory of high-harmonic generation by low-frequency laser fields. *Physical Review A* **49**, 2117–2132 (1994). URL <http://link.aps.org/doi/10.1103/PhysRevA.49.2117>.
- [61] Smith, R. & Key, M. H. A review of laser and synchrotron based x-ray sources. *J. Phys. IV France* **11**, Pr2–383–Pr2–388 (2001). URL <http://dx.doi.org/10.1051/jp4:2001274>.
- [62] Bauer, D. Theory of intense laser-matter interaction. lecture notes (2006).
- [63] Tang, X., Lyras, A. & Lambropoulos, P. Dynamics of resonances rapidly shifting under short laser pulses. *Physical Review Letters* **63**, 972–975 (1989). URL <http://link.aps.org/doi/10.1103/PhysRevLett.63.972>.

- [64] Agarwal, G. Field-Correlation Effects in Multiphoton Absorption Processes. *Physical Review A* **1**, 1445–1459 (1970). URL <http://link.aps.org/doi/10.1103/PhysRevA.1.1445>.
- [65] Glauber, R. Coherent and Incoherent States of the Radiation Field. *Physical Review* **131**, 2766–2788 (1963). URL <http://link.aps.org/doi/10.1103/PhysRev.131.2766>.
- [66] Slater, J. A Simplification of the Hartree-Fock Method. *Physical Review* **81**, 385–390 (1951). URL <http://link.aps.org/doi/10.1103/PhysRev.81.385>.
- [67] Cederbaum, L. S. & Domcke, W. *Theoretical Aspects of Ionization Potentials and Photoelectron Spectroscopy: A Green's Function Approach* (John Wiley & Sons, Inc.).
- [68] Son, S.-K. Shake-off ratios for xenon ground state 3d and 3p photoionization from $q=0+$ to $q=35+$. Private Communications (2012).
- [69] Son, S.-K., Young, L. & Santra, R. Impact of hollow-atom formation on coherent x-ray scattering at high intensity. *Physical Review A* **83**, 033402 (2011). URL <http://link.aps.org/doi/10.1103/PhysRevA.83.033402>.
- [70] Emma, P. *et al.* First lasing and operation of an ångstrom-wavelength free-electron laser. *Nature Photonics* **4**, 641–647 (2010). URL <http://www.nature.com/doi/10.1038/nphoton.2010.176>.
- [71] Madey, J. M. J. Stimulated Emission of Bremsstrahlung in a Periodic Magnetic Field. *Journal of Applied Physics* **42**, 1906 (1971). URL <http://link.aip.org/link/?JAP/42/1906/1&Agg=doi>.
- [72] Milton, S. V. *et al.* Exponential gain and saturation of a self-amplified spontaneous emission free-electron laser. *Science* **292**, 2037–41 (2001). URL <http://www.ncbi.nlm.nih.gov/pubmed/11358995>.
- [73] Emma, P., Frisch, J. & Krejcik, P. A Transverse RF Deflecting Structure for Bunch Length and Phase Space Diagnostics. *Proceedings 2001 Particle Accelerator Conference* 18–22 (2001). URL <http://www-ssrl.slac.stanford.edu/lcls/technotes/lcls-tn-00-12.pdf>.

- [74] Bane, K. *et al.* Measurements and modeling of coherent synchrotron radiation and its impact on the Linac Coherent Light Source electron beam. *Physical Review Special Topics - Accelerators and Beams* **12**, 030704 (2009). URL <http://link.aps.org/doi/10.1103/PhysRevSTAB.12.030704>.
- [75] Moeller, S. *et al.* Photon beamlines and diagnostics at LCLS. *Nuclear Instruments and Methods in Physics Research Section A: Accelerators, Spectrometers, Detectors and Associated Equipment* **635**, S6–S11 (2011). URL <http://linkinghub.elsevier.com/retrieve/pii/S0168900210024101>.
- [76] Cavaliere, A. Pulse profile measurements at LCLS. Private Communications (2012).
- [77] Ding, Y. *et al.* Measurements and Simulations of Ultralow Emittance and Ultrashort Electron Beams in the Linac Coherent Light Source. *Physical Review Letters* **102**, 254801 (2009). URL <http://link.aps.org/doi/10.1103/PhysRevLett.102.254801>.
- [78] Schmüser, P., Dohlus, M. & Rossbach, J. *Ultraviolet and Soft X-Ray Free-Electron Lasers*, vol. 229 of *Springer Tracts in Modern Physics* (Springer-Verlag, 2009), 1 edn.
- [79] Saldin, E., Schneidmiller, E. & Yurkov, M. Statistical properties of radiation from VUV and X-ray free electron laser. *Optics Communications* **148**, 383–403 (1998). URL <http://linkinghub.elsevier.com/retrieve/pii/S0030401897006706>.
- [80] Bonifacio, R., De Salvo, L., Pierini, P., Piovella, N. & Pellegrini, C. Spectrum, temporal structure, and fluctuations in a high-gain free-electron laser starting from noise. *Physical Review Letters* **73**, 70–73 (1994). URL <http://link.aps.org/doi/10.1103/PhysRevLett.73.70>.
- [81] Huang, Z. & Kim, K.-J. Review of x-ray free-electron laser theory. *Physical Review Special Topics - Accelerators and Beams* **10**, 034801 (2007). URL <http://link.aps.org/doi/10.1103/PhysRevSTAB.10.034801>.
- [82] Ackermann, W. *et al.* Operation of a free-electron laser from the extreme ultraviolet to the water window. *Nature Photonics* **1**, 336–342 (2007). URL <http://www.nature.com/doi/10.1038/nphoton.2007.76>.

- [83] Shintake, T. *et al.* A compact free-electron laser for generating coherent radiation in the extreme ultraviolet region. *Nature Photonics* **2**, 555–559 (2008). URL <http://www.nature.com/doi/finder/10.1038/nphoton.2008.134>.
- [84] Tanaka, T. & Shintake, T. SCSS X-FEL conceptual design report. Tech. Rep., RIKEN Harima Institute, Hyogo, Japan (2005).
- [85] Loh, N., Bogan, M. *et al.* Morphometry with X-ray Lasers. submitted (2012).
- [86] Reiche, S., Musumeci, P., Pellegrini, C. & Rosenzweig, J. Development of ultra-short pulse, single coherent spike for SASE X-ray FELs. *Nuclear Instruments and Methods in Physics Research Section A: Accelerators, Spectrometers, Detectors and Associated Equipment* **593**, 45–48 (2008). URL <http://linkinghub.elsevier.com/retrieve/pii/S0168900208006207>.
- [87] Emma, P. *et al.* Femtosecond and Subfemtosecond X-Ray Pulses from a Self-Amplified Spontaneous-Emission-Based Free-Electron Laser. *Physical Review Letters* **92**, 074801 (2004). URL <http://link.aps.org/doi/10.1103/PhysRevLett.92.074801>.
- [88] Hau-Riege, S. *et al.* Ultrafast disintegration of x-ray-heated solids (2012). Submitted.
- [89] Düsterer, S. *et al.* Femtosecond x-ray pulse length characterization at the Linac Coherent Light Source free-electron laser. *New Journal of Physics* **13**, 093024 (2011). URL <http://stacks.iop.org/1367-2630/13/i=9/a=093024?key=crossref.a101f2916caa04161dd7df1533dba70f>.
- [90] Helm, W., Kienberger, R. *et al.* Pulse profile measurements with infrared streaking at LCLS. in preparation (2012).
- [91] Grguras, I., Cavalieri, A. *et al.* Pulse profile measurements with THz streaking at LCLS. in preparation (2012).
- [92] Mitzner, R. *et al.* Spatio-temporal coherence of free electron laser pulses in the soft x-ray regime. *Optics Express* **16**, 19909 (2008). URL <http://www.opticsinfobase.org/abstract.cfm?URI=oe-16-24-19909>.

- [93] Schlotter, W. F. *et al.* Longitudinal coherence measurements of an extreme-ultraviolet free-electron laser. *Optics Letters* **35**, 372 (2010). URL <http://www.opticsinfobase.org/abstract.cfm?URI=ol-35-3-372>.
- [94] Mitzner, R. *et al.* Direct autocorrelation of soft-x-ray free-electron-laser pulses by time-resolved two-photon double ionization of He. *Physical Review A* **80**, 025402 (2009). URL <http://link.aps.org/doi/10.1103/PhysRevA.80.025402>.
- [95] Sorgenfrei, F. *et al.* The extreme ultraviolet split and femtosecond delay unit at the plane grating monochromator beamline PG2 at FLASH. *Review of Scientific Instruments* **81**, 043107 (2010). URL <http://www.ncbi.nlm.nih.gov/pubmed/20441325>.
- [96] Jiang, Y. *et al.* Temporal coherence effects in multiple ionization of N₂ via XUV pump-probe autocorrelation. *Physical Review A* **82**, 3–6 (2010). URL <http://link.aps.org/doi/10.1103/PhysRevA.82.041403>.
- [97] Moshhammer, R. *et al.* Second-order autocorrelation of XUV FEL pulses via time resolved two-photon single ionization of He. *Optics Express* **19**, 21698 (2011). URL <http://www.opticsinfobase.org/abstract.cfm?URI=oe-19-22-21698>.
- [98] Chalupský, J. *et al.* Spot size characterization of focused non-gaussian x-ray laser beams. *Optics Express* **18**, 27836 (2010). URL <http://www.opticsinfobase.org/abstract.cfm?URI=oe-18-26-27836>.
- [99] Krzywinski, J. Imprint Studies in the HFP Chamber at the AMO Beamline. Private Communications (2009).
- [100] Lofthus, A. & Krupenie, P. H. The spectrum of molecular nitrogen. *Journal of Physical and Chemical Reference Data* **6**, 113 (1977). URL <http://link.aip.org/link/JPCRBU/v6/i1/p113/s1&Agg=doi>.
- [101] Hau-Riege, S. P., Bionta, R. M., Ryutov, D. D. & Krzywinski, J. Measurement of x-ray free-electron-laser pulse energies by photoluminescence in nitrogen gas. *Journal of Applied Physics* **103**, 053306 (2008). URL <http://link.aip.org/link/JAPIAU/v103/i5/p053306/s1&Agg=doi>.

- [102] Hau-Riege, S. *et al.* Near-Ultraviolet Luminescence of N₂ Irradiated by Short X-Ray Pulses. *Physical Review Letters* **105**, 3–6 (2010). URL <http://link.aps.org/doi/10.1103/PhysRevLett.105.043003>.
- [103] Tiedtke, K. *et al.* Gas detectors for x-ray lasers. *Journal of Applied Physics* **103**, 094511 (2008). URL <http://link.aip.org/link/JAPIAU/v103/i9/p094511/s1&Agg=doi>.
- [104] Saito, N. *et al.* Radiometric comparison for measuring the absolute radiant power of a free-electron laser in the extreme ultraviolet. *Metrologia* **47**, 21–23 (2010). URL <http://stacks.iop.org/0026-1394/47/i=1/a=003?key=crossref.42645939dbe205325e4702e8dcd7b103>.
- [105] Wiley, W. C. & McLaren, I. H. Time-of-Flight Mass Spectrometer with Improved Resolution. *Review of Scientific Instruments* **26**, 1150 (1955). URL <http://link.aip.org/link/RSINAK/v26/i12/p1150/s1&Agg=doi>.
- [106] Sincrotrone Trieste SCpA. Atomic Calculation of Photoionization Cross-Sections and Asymmetry Parameters (2011). URL <http://ulisse.elettra.trieste.it/services/elements/WebElements.html>.
- [107] Yeh, J. & Lindau, I. Atomic subshell photoionization cross sections and asymmetry parameters: $1 < z < 103$. *Atomic Data and Nuclear Data Tables* **32**, 1 – 155 (1985). URL <http://www.sciencedirect.com/science/article/pii/0092640X85900166>.
- [108] Yeh, J. J. *Atomic Calculation of Photoionization Cross-Sections and Asymmetry Parameters* (Routledge, 1993).
- [109] Fraser, G. The ion detection efficiency of microchannel plates (MCPs). *International Journal of Mass Spectrometry* **215**, 13–30 (2002). URL <http://linkinghub.elsevier.com/retrieve/pii/S138738060100553X>.
- [110] Saito, N. & Suzuki, I. H. Multiple photoionization in Ne, Ar, Kr and Xe from 44 to 1300 eV. *International Journal of Mass Spectrometry and Ion Processes* **115**, 157–172 (1992). URL <http://linkinghub.elsevier.com/retrieve/pii/0168117692850382>.

- [111] Sorokin, A. *et al.* Pulse energy monitoring of X-ray FEL beam by gas-monitor detector. DESY Report (2010).
- [112] Carlson, T., Hunt, W. & Krause, M. Relative Abundances of Ions Formed as the Result of Inner-Shell Vacancies in Atoms. *Physical Review* **151**, 41–47 (1966). URL <http://link.aps.org/doi/10.1103/PhysRev.151.41>.
- [113] Mukoyama, T. *et al.* Charge distribution of Xe ions as a result of multiple photoionisation of Xe atoms between 4.1 and 8.0 keV. *Journal of Physics B: Atomic and Molecular Physics* **20**, 4453–4460 (1987). URL <http://stacks.iop.org/0022-3700/20/i=17/a=023?key=crossref.d4d193dce2aebaacb451608d8189511f>.
- [114] Yong, G. J. *et al.* Colossal Magnetoresistive Manganite Based Fast Bolometric X-ray Sensors for Total Energy Measurements of Free Electron Lasers. *Sensor Letters* **6**, 741–745 (2008). URL <http://openurl.ingenta.com/content/xref?genre=article&iissn=1546-198X&volume=6&issue=5&spage=741>.
- [115] Bozek, J. D. AMO instrumentation for the LCLS X-ray FEL. *The European Physical Journal Special Topics* **169**, 129–132 (2009). URL <http://www.springerlink.com/index/10.1140/epjst/e2009-00982-y>.
- [116] Heimann, P. *et al.* Linac Coherent Light Source soft x-ray materials science instrument optical design and monochromator commissioning. *Review of Scientific Instruments* **82**, 093104 (2011). URL <http://www.ncbi.nlm.nih.gov/pubmed/21974570>.
- [117] Fritz, D. The X-Ray Pump-Probe Instrument at LCLS - OSA Technical Digest (CD). In *Laser Science XXV*, LSMD2 (Optical Society of America, 2009). URL <http://www.opticsinfobase.org/abstract.cfm?URI=LS-2009-LSMD2>.
- [118] Boutet, S. & J Williams, G. The Coherent X-ray Imaging (CXI) instrument at the Linac Coherent Light Source (LCLS). *New Journal of Physics* **12**, 035024 (2010). URL <http://stacks.iop.org/1367-2630/12/i=3/a=035024?key=crossref.ee7b62eb5549902891c671e9eccc3bf3>.
- [119] Robert, A. The X-Ray Photon Correlation Spectroscopy Instrument at LCLS - OSA Technical Digest (CD). In *Laser Science XXV*, LSThC1 (Optical Society

- of America, 2009). URL <http://www.opticsinfobase.org/abstract.cfm?URI=LS-2009-LSThC1>.
- [120] Stanford National Accelerator Laboratory, Lawrence Livermore National Laboratory and PSRI/Science and Technology Facilities Council. Matter in Extreme Conditions Instrument, Conceptual Design Report (2009). URL <http://www.slac.stanford.edu/cgi-wrap/getdoc/slac-r-934.pdf>.
- [121] SLAC National Accelerator Laboratory. LCLS User Resources Site (2011). URL <http://www-ssrl.slac.stanford.edu/lcls/users/>.
- [122] Sorokin, A. *et al.* Method based on atomic photoionization for spot-size measurement on focused soft x-ray free-electron laser beams. *Applied Physics Letters* **89**, 221114 (2006). URL <http://link.aip.org/link/APPLAB/v89/i22/p221114/s1&Agg=doi>.
- [123] Chalupsky, J. *et al.* Comparing different approaches to characterization of focused X-ray laser beams. *Nuclear Instruments and Methods in Physics Research Section A: Accelerators, Spectrometers, Detectors and Associated Equipment* **631**, 130–133 (2011). URL <http://linkinghub.elsevier.com/retrieve/pii/S0168900210027816>.
- [124] Flöter, B. *et al.* EUV Hartmann sensor for wavefront measurements at the Free-electron LASer in Hamburg. *New Journal of Physics* **12**, 083015 (2010). URL <http://stacks.iop.org/1367-2630/12/i=8/a=083015?key=crossref.65f1d137cb191e60ac8977a379fb4782>.
- [125] Chalupský, J. *et al.* Characteristics of focused soft X-ray free-electron laser beam determined by ablation of organic molecular solids. *Optics Express* **15**, 6036–43 (2007). URL <http://www.ncbi.nlm.nih.gov/pubmed/19546907>.
- [126] Barty, A. *et al.* Predicting the coherent X-ray wavefront focal properties at the Linac Coherent Light Source (LCLS) X-ray free electron laser. *Optics Express* **17**, 15508–19 (2009). URL <http://www.ncbi.nlm.nih.gov/pubmed/19724548>.
- [127] Strüder, L. *et al.* Large-format, high-speed, X-ray pnCCDs combined with electron and ion imaging spectrometers in a multipurpose chamber for experiments at 4th generation light sources. *Nuclear Instruments and Methods in*

- Physics Research Section A: Accelerators, Spectrometers, Detectors and Associated Equipment* **614**, 483–496 (2010). URL <http://linkinghub.elsevier.com/retrieve/pii/S0168900209023900>.
- [128] Spielberger, L. *Erforschung von Korrelationseffekten in atomaren Mehrteilchen-Systemen: Doppel- und Einfachionisation von Helium induziert durch hochenergetische Photonen*. Ph.D. thesis, Goethe-Universität, Frankfurt am Main (1996). URL <http://www.atom.uni-frankfurt.de/publications/files/LutzSpielberger1996.pdf>.
- [129] Bergmann, L., Schaefer, C. & Kleinermanns, K. *Gase, Nanosysteme, Flüssigkeiten*. Bergmann-Schaefer Lehrbuch Der Experimentalphysik: Band 5 (Gruyter Verlag, 2005), 2 edn.
- [130] Beijerinck, H. Absolute intensities and perpendicular temperatures of supersonic beams of polyatomic gases. *Physica B+C* **111**, 327–352 (1981). URL <http://www.ncbi.nlm.nih.gov/pubmed/22302754><http://linkinghub.elsevier.com/retrieve/pii/0378436381901121>.
- [131] Ullrich, J. *et al.* Recoil-ion momentum spectroscopy. *Nuclear Instruments and Methods in Physics Research Section B: Beam Interactions with Materials and Atoms* **61**, 415–422 (1991). URL <http://linkinghub.elsevier.com/retrieve/pii/0168583X91953155>.
- [132] Ullrich, J. *et al.* Recoil-ion momentum spectroscopy. *Journal of Physics B: Atomic, Molecular and Optical Physics* **30**, 2917–2974 (1997). URL <http://stacks.iop.org/0953-4075/30/i=13/a=006?key=crossref.277731322fcf81426f97a1bedb9f3807>.
- [133] Dörner, R. *et al.* Cold Target Recoil Ion Momentum Spectroscopy: a momentum microscope to view atomic collision dynamics. *Physics Reports* **330**, 95–192 (2000). URL <http://linkinghub.elsevier.com/retrieve/pii/S037015739900109X>.
- [134] Ullrich, J. *et al.* Recoil-ion and electron momentum spectroscopy: reaction-microscopes. *Reports on Progress in Physics* **66**, 1463–1545 (2003). URL <http://linkinghub.elsevier.com/retrieve/pii/>

0168583X91953155<http://stacks.iop.org/0034-4885/66/i=9/a=203?key=crossref.4f0ed0c11253bbad6096727290d95871>.

- [135] Scientific Instrument Services, Inc. (SIS). SIMION Industry standard charged particle optics simulation software. . URL <http://simion.com/>.
- [136] Rolles, D. *et al.* A velocity map imaging spectrometer for electron-ion and ion-ion coincidence experiments with synchrotron radiation. *Nuclear Instruments and Methods in Physics Research Section B: Beam Interactions with Materials and Atoms* **261**, 170–174 (2007). URL <http://linkinghub.elsevier.com/retrieve/pii/S0168583X07009949>.
- [137] Vrakking, M. J. J. An iterative procedure for the inversion of two-dimensional ion/photoelectron imaging experiments. *Review of Scientific Instruments* **72**, 4084 (2001). URL <http://link.aip.org/link/RSINAK/v72/i11/p4084/s1&Agg=doi>.
- [138] Whitaker, B. J. *Imaging in Molecular Dynamics: Technology and Applications* (Cambridge University Press, 2003), 1 edn.
- [139] Johnsson, P. *et al.* Velocity map imaging of atomic and molecular processes at the free electron laser in Hamburg (FLASH). *Journal of Modern Optics* **55**, 2693–2709 (2008). URL <http://www.tandfonline.com/doi/abs/10.1080/09500340802393062>.
- [140] Eppink, A. T. J. B. & Parker, D. H. Velocity map imaging of ions and electrons using electrostatic lenses: Application in photoelectron and photofragment ion imaging of molecular oxygen. *Review of Scientific Instruments* **68**, 3477 (1997). URL <http://link.aip.org/link/RSINAK/v68/i9/p3477/s1&Agg=doi>.
- [141] O’Keeffe, P. *et al.* A photoelectron velocity map imaging spectrometer for experiments combining synchrotron and laser radiations. *Review of Scientific Instruments* **82**, 033109 (2011). URL <http://www.ncbi.nlm.nih.gov/pubmed/21456720>.
- [142] Jagutzki, O. Fast position and time-resolved read-out of micro-channelplates with the delay-line technique for single-particle and photon-detection. In *Pro-*

- ceedings of SPIE*, vol. 3438, 322–333 (SPIE, 1998). URL <http://link.aip.org/link/?PSI/3438/322/1&Agg=doi>.
- [143] Motomura, K. *et al.* Multi-coincidence ion detection system for EUV-FEL fragmentation experiments at SPring-8. *Nuclear Instruments and Methods in Physics Research Section A: Accelerators, Spectrometers, Detectors and Associated Equipment* **606**, 770–773 (2009). URL <http://linkinghub.elsevier.com/retrieve/pii/S0168900209008882>.
- [144] Hamamatsu Corporation. MCP and MCP assembly selection guide. URL http://sales.hamamatsu.com/assets/pdf/catsandguides/MCPassy_TMCP0001E08.pdf.
- [145] Hartmann, R. *et al.* Large format imaging detectors for x-ray free-electron-lasers. In *Proceedings of the SPIE*, vol. 8078, 80780W–80780W–9 (SPIE, 2011). URL <http://link.aip.org/link/PSISDG/v8078/i1/p80780W/s1&Agg=doi>.
- [146] Agilent Technologies. Agilent U1065A – Acqiris High-Speed cPCI Digitizers – DC282. URL <http://cp.literature.agilent.com/litweb/pdf/5989-7443EN.pdf>.
- [147] Adimec. Adimec Opal-1000. URL http://www.adimec.com/en/Service_Menu/Industrial_camera_products/High_performance_cameras_for_the_machine_vision_applications/OPAL_series_High_speed_CCD_cameras/OPAL-1000.
- [148] 1stVision Inc. Pulnix TMC-6740CL. URL http://www.1stvision.com/cameras/JAI/dataman/TM-TMC-6740CL_revAw.pdf.
- [149] Foucar, L. *et al.* CASS - CFEL ASG Software Suite. Submitted to Computer Physics Communications, Elsevier.
- [150] Agilent Technologies. Agilent U1051A – Acqiris TC890 Time-to-Digital Converter. URL <http://cp.literature.agilent.com/litweb/pdf/5989-7109EN.pdf>.
- [151] Argonne National Laboratory. Experimental Physics and Industrial Control System. URL <http://www.aps.anl.gov/epics/>.

- [152] The HDF Group. Hierarchical Data Format - HDF5. URL <http://www.hdfgroup.org/HDF5/>.
- [153] Antcheva, I. *et al.* Root – a c++ framework for petabyte data storage, statistical analysis and visualization. *Computer Physics Communications* **180**, 2499 – 2512 (2009). URL <http://www.sciencedirect.com/science/article/pii/S0010465509002550>. A celebratory issue focused on quality software for high performance, grid and novel computing architectures.
- [154] OriginLab Corporation. Data Analysis and Graphing Software. URL <http://www.originlab.com/index.aspx?go=Products/OriginPro>.
- [155] Andritschke, R., Hartner, G., Hartmann, R., Meidinger, N. & Struder, L. Data analysis for characterizing PNCCDS. In *2008 IEEE Nuclear Science Symposium Conference Record*, 2166–2172 (IEEE, 2008). URL <http://ieeexplore.ieee.org/lpdocs/epic03/wrapper.htm?arnumber=4774781>.
- [156] Kimmel, N. *et al.* Calibration methods and performance evaluation for pnCCDs in experiments with FEL radiation. In *Proceedings of the SPIE*, vol. 8078, 80780V–80780V–11 (SPIE, 2011). URL <http://link.aip.org/link/PSISDG/v8078/i1/p80780V/s1&Agg=doi>.
- [157] Weidenspointner, G., Epp, S., Hartmann, A. & Hartmann, R. Practical experience from operating the imaging pnCCD detectors of the CAMP instrument at LCLS. In *Proceedings of the SPIE*, vol. 8078, 80780U (SPIE, 2011). URL http://spiedigitallibrary.org/proceedings/resource/2/psisdg/8078/1/80780U_1?isAuthorized=no.
- [158] Bostedt, C. Focus size in the CAMP endstation. Private Communications (2011).
- [159] Makris, M., Lambropoulos, P. & Mihelič, a. Theory of Multiphoton Multielectron Ionization of Xenon under Strong 93-eV Radiation. *Physical Review Letters* **102**, 033002 (2009). URL <http://link.aps.org/doi/10.1103/PhysRevLett.102.033002>.
- [160] Santra, R. & Greene, C. Multiphoton ionization of xenon in the vuv regime. *Physical Review A* **70**, 3–10 (2004). URL <http://link.aps.org/doi/10.1103/PhysRevA.70.053401>.

- [161] Martin, S., Brédy, R., Bernard, J., Désesquelles, J. & Chen, L. Very Fast Hollow-Atom Decay Processes in Xe^{30+} - C_{60} Collisions. *Physical Review Letters* **89** (2002). URL <http://link.aps.org/doi/10.1103/PhysRevLett.89.183401>.
- [162] Karim, K. R., Grabbe, S. R. & Bhalla, C. P. Radiative and Auger de-excitation of hollow argon atoms. *Journal of Physics B: Atomic, Molecular and Optical Physics* **29**, 4007–4016 (1996). URL <http://stacks.iop.org/0953-4075/29/i=17/a=021?key=crossref.bba67ae5c1bb8d92a34c711e23d1933e>.
- [163] Briand, J.-P. *et al.* Observation of Hollow Atoms or Ions above Insulator and Metal Surfaces. *Physical Review Letters* **77**, 1452–1455 (1996). URL <http://link.aps.org/doi/10.1103/PhysRevLett.77.1452>.
- [164] Briand, J.-P. *et al.* The interaction of slow highly charged ions on surfaces. *Review of Scientific Instruments* **71**, 627 (2000). URL <http://link.aip.org/link/RSINAK/v71/i2/p627/s1&Agg=doi>.
- [165] Son, S.-K. Calculated Photoionization Cross Sections of Rydberg States in Highly Charged Xenon. Private Communications (2012).
- [166] Son, S.-K. Calculated Photoionization Cross Sections and Charge State Distribution of Kr. Private Communications (2011).
- [167] Abdullah, A. H., El-shemi, A. M. & Ghoneim, A. A. Yields of multiply charged ions produced from inner-shell ionization in neutral Ne, Ar and Kr atoms. *Radiation Physics and Chemistry* **68**, 697–705 (2003).
- [168] Cowan, R. *The Theory of Atomic Structure and Spectra*. Los Alamos Series in Basic and Applied Sciences (University of California Press, 1981), 1 edn.
- [169] Viefhaus, J. *et al.* Auger cascades versus direct double Auger: relaxation processes following photoionization of the Kr 3d and Xe 4d, 3d inner shells. *Journal of Physics B: Atomic, Molecular and Optical Physics* **38**, 3885–3903 (2005). URL <http://stacks.iop.org/0953-4075/38/i=21/a=011?key=crossref.ea0dd0550c766bd887ac46f6effb50ad>.
- [170] Rudenko, a. *et al.* Recoil-Ion Momentum Distributions for Two-Photon Double Ionization of He and Ne by 44 eV Free-Electron Laser Radiation. *Physical*

- Review Letters* **101**, 073003 (2008). URL <http://link.aps.org/doi/10.1103/PhysRevLett.101.073003>.
- [171] Moshhammer, R. *et al.* Few-Photon Multiple Ionization of Ne and Ar by Strong Free-Electron-Laser Pulses. *Physical Review Letters* **98**, 203001 (2007). URL <http://link.aps.org/doi/10.1103/PhysRevLett.98.203001>.
- [172] Yamakawa, K. *et al.* Many-Electron Dynamics of a Xe Atom in Strong and Superstrong Laser Fields. *Physical Review Letters* **92**, 123001 (2004). URL <http://link.aps.org/doi/10.1103/PhysRevLett.92.123001>.
- [173] Richard, P. *et al.* The production of highly charged Ar and Xe recoil ions by fast uranium impact. *Nuclear Instruments and Methods in Physics Research Section A: Accelerators, Spectrometers, Detectors and Associated Equipment* **240**, 532–537 (1985). URL <http://linkinghub.elsevier.com/retrieve/pii/0168900285906771>.
- [174] DESY. FLASH Brochure (2007). URL http://hasylab.desy.de/facilities/sr_and_fel_basics/fel_basics/index_eng.html.
- [175] Dimauro, L. *et al.* First SASE and seeded FEL lasing of the NSLS DUV FEL at 266 and 400nm. *Nuclear Instruments and Methods in Physics Research Section A: Accelerators, Spectrometers, Detectors and Associated Equipment* **507**, 15–18 (2003). URL <http://linkinghub.elsevier.com/retrieve/pii/S0168900203008258>.
- [176] Togashi, T. *et al.* Extreme ultraviolet free electron laser seeded with high-order harmonic of Ti:sapphire laser. *Optics Express* **19**, 317 (2010). URL <http://www.opticsinfobase.org/abstract.cfm?URI=oe-19-1-317>.
- [177] Saldin, E., Schneidmiller, E., Shvydko, Y. & Yurkov, M. X-ray FEL with a meV bandwidth. *Nuclear Instruments and Methods in Physics Research Section A: Accelerators, Spectrometers, Detectors and Associated Equipment* **475**, 357–362 (2001). URL <http://linkinghub.elsevier.com/retrieve/pii/S016890020101539X>.
- [178] Deacon, D. *et al.* First Operation of a Free-Electron Laser. *Physical Review Letters* **38**, 892–894 (1977). URL <http://link.aps.org/doi/10.1103/PhysRevLett.38.892>.

- [179] Barletta, W. *et al.* Free electron lasers: Present status and future challenges. *Nuclear Instruments and Methods in Physics Research Section A: Accelerators, Spectrometers, Detectors and Associated Equipment* **618**, 69–96 (2010). URL <http://linkinghub.elsevier.com/retrieve/pii/S0168900210005656>.
- [180] Krause, M. O. Atomic radiative and radiationless yields for K and L shells. *Journal of Physical and Chemical Reference Data* **8**, 307 (1979). URL <http://link.aip.org/link/JPCRBV/v8/i2/p307/s1&Agg=doi>.
- [181] Bhalla, C. P., Folland, N. O. & Hein, M. A. Theoretical *K*-Shell Auger Rates, Transition Energies, and Fluorescence Yields for Multiply Ionized Neon. *Physical Review A* **8**, 649–657 (1973). URL <http://link.aps.org/doi/10.1103/PhysRevA.8.649>.
- [182] Albiez, A., Thoma, M., Weber, W. & Mehlhorn, W. KL 2,3 ionization in neon by electron impact in the range 1.5–50 keV: cross sections and alignment. *Zeitschrift für Physik D: Atoms, Molecules and Clusters* **16**, 97–106 (1990). URL <http://www.springerlink.com/index/10.1007/BF01679570>.
- [183] Kanngießer, B. *et al.* Simultaneous determination of radiative and nonradiative decay channels in the neon K shell. *Physical Review A* **62**, 014702 (2000). URL <http://link.aps.org/doi/10.1103/PhysRevA.62.014702>.
- [184] Chen, M. Auger transition rates and fluorescence yields for the double-K-hole state. *Physical Review A* **44**, 239–242 (1991). URL <http://link.aps.org/doi/10.1103/PhysRevA.44.239>.
- [185] Schins, J. *et al.* Observation of Laser-Assisted Auger Decay in Argon. *Physical Review Letters* **73**, 2180–2183 (1994). URL <http://link.aps.org/doi/10.1103/PhysRevLett.73.2180>. [/link.aps.org/doi/10.1103/PhysRevLett.73.2180](http://link.aps.org/doi/10.1103/PhysRevLett.73.2180).
- [186] Itatani, J. *et al.* Attosecond Streak Camera. *Physical Review Letters* **88**, 173903 (2002). URL <http://link.aps.org/doi/10.1103/PhysRevLett.88.173903>.
- [187] Frühling, U. Light-field streaking for FELs. *Journal of Physics B: Atomic, Molecular and Optical Physics* **44**, 243001 (2011). URL

<http://stacks.iop.org/0953-4075/44/i=24/a=243001?key=crossref.5ae504c47a6f4074370ee8334a24046e>.

- [188] Frühling, U. *et al.* Single-shot terahertz-field-driven X-ray streak camera. *Nature Photonics* **3**, 523–528 (2009). URL <http://www.nature.com/doifinder/10.1038/nphoton.2009.160>.
- [189] Catravas, P. *et al.* Measurement of Electron-Beam Bunch Length and Emittance Using Shot-Noise-Driven Fluctuations in Incoherent Radiation. *Physical Review Letters* **82**, 5261–5264 (1999). URL <http://link.aps.org/doi/10.1103/PhysRevLett.82.5261>.
- [190] Krzywinski, J. A new method for ultrashort electron pulse-shape measurement using synchrotron radiation from a bending magnet. *Nuclear Instruments and Methods in Physics Research Section A: Accelerators, Spectrometers, Detectors and Associated Equipment* **401**, 429–441 (1997). URL <http://linkinghub.elsevier.com/retrieve/pii/S016890029700987X>.
- [191] Pfeifer, T., Jiang, Y., Düsterer, S., Moshhammer, R. & Ullrich, J. Partial-coherence method to model experimental free-electron laser pulse statistics. *Optics Letters* **35**, 3441 (2010). URL <http://www.opticsinfobase.org/abstract.cfm?URI=ol-35-20-3441>.
- [192] Rudek, B. *et al.* Ultra-Efficient Ionization of Heavy Atoms by Intense X-Ray Free-Electron Laser Pulses. submitted (2012).
- [193] Jahnke, T. *Interatomic Coulombic Decay - Experimentelle Untersuchung eines neuartigen, interatomaren Abregungsmechanismus*. Ph.D. thesis, Goethe-Universität, Frankfurt am Main (2005). URL <http://www.atom.uni-frankfurt.de/publications/files/TillJahnke2005.pdf>.
- [194] Toennies, J. P. & Winkelmann, K. Theoretical studies of highly expanded free jets: Influence of quantum effects and a realistic intermolecular potential. *The Journal of Chemical Physics* **66**, 3965 (1977). URL <http://link.aip.org/link/JCPA6/v66/i9/p3965/s1&Agg=doi>.
- [195] Brusdeylins, G., Toennies, J. P. & Vollmer, R. XII. Symposium on Molecular Beams. In *Book of Abstracts* (1989).

- [196] Epp, S. *Röntgen-Laserspektroskopie hochgeladener Ionen in einer EBIT am Freie-Elektronen-Laser FLASH*. Ph.D. thesis, Ruprecht-Karls-Universität, Heidelberg (2007). URL http://archiv.ub.uni-heidelberg.de/volltextserver/frontdoor.php?source_opus=7493.
- [197] Strüder, L. *et al.* A 36 cm² large monolithic pn-charge coupled device x-ray detector for the European XMM satellite mission. *Review of Scientific Instruments* **68**, 4271 (1997). URL <http://link.aip.org/link/RSINAK/v68/i11/p4271/s1&Agg=doi>.
- [198] Strüder, L. *et al.* The MPI/AIT X-ray imager (MAXI) - High speed pn CCDs for X-ray detection. *Nuclear Instruments and Methods in Physics Research Section A: Accelerators, Spectrometers, Detectors and Associated Equipment* **288**, 227–235 (1990). URL <http://linkinghub.elsevier.com/retrieve/pii/016890029090490W>.
- [199] Meidinger, N. *et al.* pnCCD for photon detection from near-infrared to X-rays. *Nuclear Instruments and Methods in Physics Research Section A: Accelerators, Spectrometers, Detectors and Associated Equipment* **565**, 251–257 (2006). URL <http://linkinghub.elsevier.com/retrieve/pii/S0168900206007662>.
- [200] Herrmann, S. *et al.* Mixed signal pnCCD readout ASIC for the future X-Ray astronomy mission eROSITA. *2007 IEEE Nuclear Science Symposium Conference Record* 2398–2403 (2007). URL <http://ieeexplore.ieee.org/lpdocs/epic03/wrapper.htm?arnumber=4436626>.

Selbständigkeitserklärung

Erklärung gemäß §8(3b) der Promotionsordnung darüber, dass die Doktorarbeit auf selbständiger Arbeit beruht.

”Ich versichere hiermit, dass ich die vorliegende Arbeit selbstständig verfasst, keine anderen als die angegebenen Hilfsmittel verwendet und sämtliche Stellen, die benutzten Werken im Wortlaut oder dem Sinne nach entnommen sind, mit Quellen- bzw. Herkunftsangaben kenntlich gemacht habe.”

Hamburg, 22. März 2012

Benedikt Rudek